Microwave photonics

Jianping YAO[1*] & Jose CAPMANY[2,3*]

[1]*Microwave Photonics Research Laboratory, School of Electrical Engineering and Computer Science,
University of Ottawa, Ottawa ON K1W 1K3, Canada;*
[2]*ITEAM Research Institute, Universitat Politècnica de València, València 46022, Spain;*
[3]*iPronics, Programmable Photonics, 7 C. Pedro Duque, València 46022, Spain*

Abstract Microwave photonics, an interdisciplinary field that combines microwave engineering and photonic technology for the generation, transmission, processing, and control of microwave signals, to take advantage of the broad bandwidth, high frequency, and low loss offered by modern photonics, has been intensively researched for the last few decades, and numerous solutions have been proposed and demonstrated. In this article, an overview about microwave photonics is provided which covers the basic concepts of microwave photonics, photonic-assisted microwave signal generation, photonic-assisted microwave signal processing, and true time delay beamforming. The implementation of microwave photonic systems based on photonic integrated circuits is also reviewed, including the design, fabrication, and material platforms, application-specific photonic integrated circuits for microwave photonics, and programmable integrated microwave photonics. The challenges and future applications of microwave photonics are also discussed.

Keywords microwave photonics, photonic integrated circuits, microwave photonic link, microwave photonic signal processor, optoelectronic oscillator, radio over fiber

1 Introduction

Microwave photonics is an area that deals with the use of photonic techniques to generate, process, control, and transmit microwave signals to take advantage of the high frequency, large bandwidth and low loss offered by modern photonics for applications such as broadband wireless communications, radar, sensing, imaging and instrumentation. Digital electronics is the most widely used approach nowadays for these applications. However, its speed is less than a few GHz, limited mainly by the electronic sampling rate. The unique capabilities offered by modern photonics for the generation and processing of ultra-wideband, high-frequency microwave signals make it a promising alternative for wideband microwave applications. For the past four decades, numerous new techniques have been proposed and demonstrated. A few articles reviewing the microwave photonics techniques have been published [1–4], but the emphasis of these studies was placed on the implementation of the microwave photonics techniques based on discrete components. In this article, a comprehensive review of microwave photonics techniques with their implementation based on both discrete components and photonic integrated circuits (PICs) is performed. Specifically, we first review the basic concepts of microwave photonics including the general architecture of a microwave photonics link and its performance measures including the link gain, noise figure, and spurious free dynamic range. Then, techniques to generate high frequency and low phase noise microwave signals, including optical injection locking, optical phase lock loop, external modulation, and optoelectronic oscillation, are presented. Techniques to process microwave signals, especially the implementation of microwave photonic filters, are also reviewed. Microwave arbitrary waveform generation based on direct space-to-time mapping, spectral shaping and wavelength-to-time mapping, and temporal pulse shaping is also reviewed. Broadband phased array beamforming is an important application of microwave photonics and is reviewed.

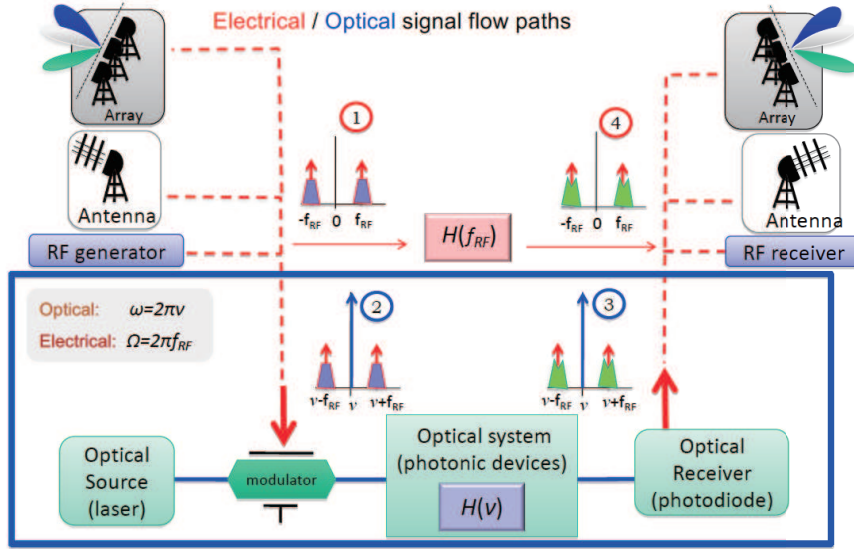* Corresponding author (email: jpyao@uottawa.ca, jcapmany@iteam.upv.es)

Figure 1   (Color online) General layout of a microwave photonic link.

Thanks to the fast advancement in PIC technology, all the microwave photonic techniques previously demonstrated based on discrete components can be implemented using PICs. In this article, integrated microwave photonics (IMWP) is also reviewed. First, the materials systems that can be employed for the implementation of microwave photonic subsystems and systems including indium phosphide (InP), silicon on insulator (SOI), silicon nitride (Si_3N_4) and lithium niobate on insulator (LOI), are reviewed. Then, recent progress in application-specific photonic integrated circuits, where a particular circuit configuration to optimally perform a particular microwave photonics functionality, is discussed. General purpose programmable microwave photonic signal processors that are capable of performing all the main microwave signal generation and processing functionalities by suitable software programming are also reviewed. The challenges in implementing fully integrated microwave photonics systems based on heterogeneous integration are discussed.

2   Basic concepts for microwave photonics

2.1   Microwave photonics links

A microwave photonic link (MWPL) is a basic building block of any system or network in charge of the distribution of radiofrequency (RF) signals by optical means [5–12]. A general layout of an MWPL is shown in Figure 1 and it will serve us to introduce some basic definitions and concepts.

The starting point is an input RF signal with its spectrum having two sidebands centered at frequency $\pm f_{RF}$, as shown in point 1. This signal, which can have its origin either from an RF generator or from the reception by means of a single or an arrayed antenna, modulates the light from an optical source to up-convert its spectrum to the optical region of the spectrum (point 2), such that the sidebands are now centered at $\nu \pm f_{RF}$, where ν represents the central frequency of the optical source. The combined optical signal is then processed by an optical system composed of several photonic devices (including the possibility of an optical fiber link) and characterized by an overall lumped optical field transfer function $H(\nu)$. The MWPL modifies the spectral characteristics of the sidebands as illustrated in point 3. Finally, a photodetector (PD) is employed to down-convert the sidebands again to the RF part of the spectrum by suitable beating with the optical carrier, so the recovered RF signal, processed by the MWPL (as shown in point 4), is ready to be sent to an RF receiver or to be re-radiated. The overall electrical transfer function $H(f_{RF})$ is also shown and must not be confused with the optical field transfer function of the auxiliary optical system.

MWPLs can range from very simple to very complex configurations depending, fundamentally, on the nature of the auxiliary optical system transfer function $H(\nu)$. The simplest configuration, which historically was the first to be considered, corresponds to the case where the optical system is a dispersionless
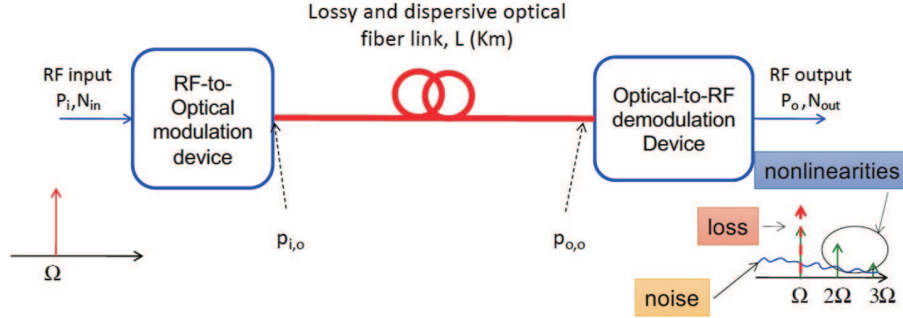
Figure 2   (Color online) Diagram of a simple MWPL showing the relevant signal nomenclature at different points of the link and the input (lower left hand-side)/output (lower right hand-side) signal spectra for an input RF tone.

optical fiber link. Though limited in its applications this configuration is quite adequate for introducing the concepts related to the operation and figures of merit.

2.2   Figures of merit

Figure 2 shows the diagram of a simple MWPL [5], where the optical transmitter and the optical receiver are connected by means of a lossy and dispersionless optical fiber link of a length of L. Fiber losses are given by an attenuation coefficient α in dB/km.

If an input RF tone at frequency Ω_{RF} is injected into the link as shown in the lower left hand-side inset, the output RF signal, shown in the lower right hand-side inset, is generally composed of three contributions: the desired input tone itself with a decreased amplitude due to the system losses, noise spread over a given spectral region, and nonlinear harmonic distortion contributions appearing at $n\Omega_{\mathrm{RF}}$ $n = 2, 3, \ldots$. These three effects characterize the quality of the MWPL in terms of three figures of merit (FOMs): the RF link gain G_{RF}, the noise figure NF, and the spurious free dynamic range SFDR. In very simple terms, G_{RF} accounts for the overall end-to-end system losses, NF accounts for the overall noise level introduced by the system components, and the SFDR qualifies the impact of nonlinearities.

RF gain. Referring to the configuration of the MWPL in Figure 2, let p_i represent the RF power of the input tone at the frequency Ω_{RF} injected to the MWPL. In the same way, p_o represents the RF power of the output tone at frequency Ω_{RF} extracted from the MWPL. The RF link gain in natural units is defined as [5–7, 9]

$$G_{\mathrm{RF}} = \frac{p_o}{p_i}. \tag{1}$$

It is convenient to re-express (1) in terms of some intermediate auxiliary values of the optical power at the input and the output of the optical fiber link. If we define $p_{i,o}$ as the root mean square (RMS) power magnitude of the time varying optical power at the link input and $p_{o,o}$ as the RMS power magnitude of the time varying optical power at the link output, then

$$p_{o,o} = 10^{-\frac{\alpha L}{10}} p_{i,o} = T_{M\text{-}D} p_{i,o}, \tag{2}$$

where $T_{M\text{-}D}$ represents the optical transmittance function from the optical transmitter to the optical detector. Using the relationship given by (2) in (1), we get [6]

$$G_{\mathrm{RF}} = \left(\frac{p_o}{p_{o,o}^2}\right) \times T_{M\text{-}D}^2 \times \left(\frac{p_{i,o}^2}{p_i}\right). \tag{3}$$

Eq. (3) seems in principle an unnecessary complication of the simple version given in (1). However, it is useful in practice, as it is the product of three factors that separately characterize the performance of the optical receiver, the optical link, and the optical transmitter, respectively.

The $p_{i,o}^2/p_i$ factor represents the equivalent input-output RF power transmission at the optical transmitter. For an external Mach-Zehnder modulator (MZM) employed as shown in Figure 3, then the optical power transmission versus input modulation voltage of the MZM is given by

$$T_{\mathrm{MZM}} = \frac{p_{i,o}}{P_o} = \frac{\alpha_{\mathrm{MZM}}}{2}\left[1 + \cos\left(\frac{\pi v_M}{V_\pi}\right)\right], \tag{4}$$
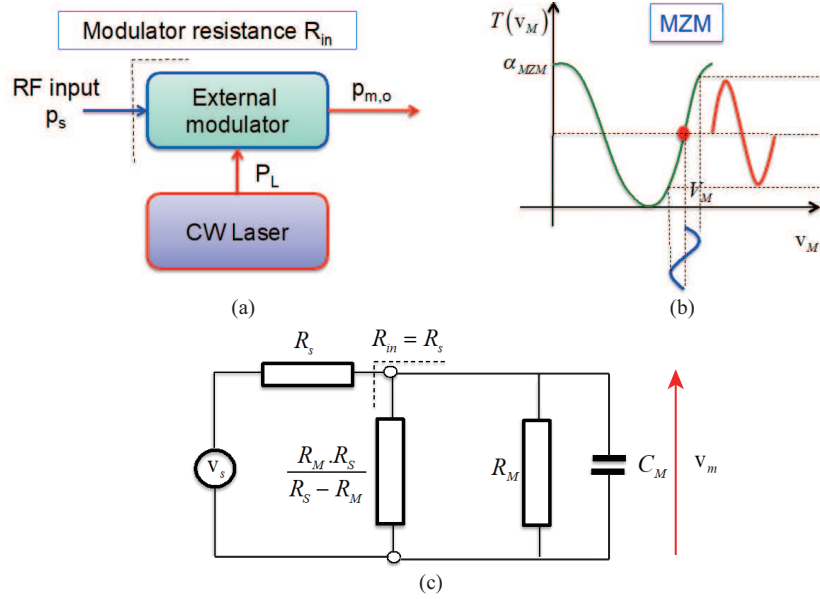
Figure 3 (Color online) (a) Optical transmitter employing a continuous-wave (CW) optical source and a Mach–Zehnder modulator (MZM) external modulator; (b) optical power vs. input voltage transfer characteristic for an MZM; (c) resistive impedance matching circuit for an external modulator.

where P_o represents the output power from the continuous-wave (CW) laser (input power to the modulator), α_{MZM} is the MZM optical loss, and the modulation voltage is expressed as $V_T = V_M + v_M(t)$, where V_M is the bias voltage and $v_M(t)$ is the time varying RF signal. The modulation efficiency in terms of output optical power vs. input electrical current for an MZM biased at the quadrature point $(V_M = V_\pi/2)$ is given by

$$s_m \triangleq \left(\frac{\mathrm{d}p_{i,o}}{\mathrm{d}i_M}\right)_{I_M} = R_{\mathrm{in}}\left(\frac{\mathrm{d}p_{i,o}}{\mathrm{d}v_M}\right)_{V_M} = R_{\mathrm{in}}P_o\left(\frac{\mathrm{d}T\,(v_M)}{\mathrm{d}v_M}\right)_{V_M} = \frac{\pi\alpha_{\mathrm{MZM}}P_oR_{\mathrm{in}}}{2V_\pi}. \tag{5}$$

When using a resistively matched network between the voltage source and the modulator, as shown in Figure 3(c), then it is straightforward to show by means of circuit analysis that

$$\frac{p_{i,o}^2}{p_i} \approx \frac{s_m^2}{R_{\mathrm{in}}} = \left(\frac{\pi\alpha_{\mathrm{MZM}}P_o}{2V_\pi}\right)^2 R_{\mathrm{in}}. \tag{6}$$

The $p_o/p_{o,o}^2$ factor represents the equivalent input-output RF power transmission at the optical receiver. Again, it is advisable to employ electrical circuits to match the output or load resistance to that of the optical receiver. In that case it is possible to make the following approximation [5,6]:

$$\frac{p_o}{p_{o,o}^2} \approx \Re^2 R_{\mathrm{out}}, \tag{7}$$

where $\Re$ is the detector responsivity. Introducing (2), (6), (7) into (3), one gets

$$G_{\mathrm{RF}} = \left(\frac{\pi I_{dc}}{V_\pi}\right)^2 R_{\mathrm{in}}R_{\mathrm{out}}, \tag{8}$$

where the average received photocurrent is given by

$$I_{dc} = \frac{\alpha_{\mathrm{MZM}}\Re P_o 10^{-\frac{\alpha L}{10}}}{2}. \tag{9}$$

Noise figure. Figure 2 also shows the noise power at the input N_{in} and output N_{out} of the MWPL. The link noise figure NF is defined as the quotient between the signal to noise ratio (SNR) at the input and the SNR at the output, given by

$$\mathrm{NF} = 10\log\left(\frac{p_i/N_{\mathrm{in}}}{p_o/N_{\mathrm{out}}}\right) = 10\log\left(\frac{N_{\mathrm{out}}}{G_{\mathrm{RF}}N_{\mathrm{in}}}\right), \tag{10}$$

where we have made use of (1).

There are two important consequences derived from (10). First, if no noise is added by the link NF = 0 dB, then we have $N_{\text{out}} = G_{\text{RF}} N_{\text{in}}$. Second, NF does not depend on the RF signal power at the link input. In practice, however, noise is added by several electronic and photonic components in the link (laser, photodetector, electronic components). This implies that, in general, $N_{\text{out}} = G_{\text{RF}} N_{\text{in}} + N_{\text{add}}$, with N_{add} representing the power of additional noise sources at the system output. Hence, we have

$$\text{NF} = 10 \log \left(\frac{G_{\text{RF}} N_{\text{in}} + N_{\text{add}}}{G_{\text{RF}} N_{\text{in}}} \right) = 10 \log \left(1 + \frac{N_{\text{add}}}{G_{\text{RF}} N_{\text{in}}} \right). \tag{11}$$

Note that the effect of the additional noise can be referred to as the system input as an additional noise source with the power given by $N_{\text{add}}/G_{\text{RF}}$. Furthermore, Eq. (11) can be generalized to include noise sources appearing at intermediate points in the system. In this case, if $N_{\text{add},i}$ represents the noise power generated at the system output at point i and $G_{\text{RF},i}$ represents the RF gain between the system input and point i, then the overall contribution to the noise figure is $N_{\text{add},i}/G_{\text{RF},i}$, given by [6,8]

$$\text{NF} = 10 \log \left(1 + \frac{\sum_i \left(N_{\text{add},i}/G_{\text{RF},i} \right)}{N_{\text{in}}} \right). \tag{12}$$

Depending on the system complexity, more or less noise sources will have to be considered. However, the most important ones, i.e., those that have to be considered in any system, are the thermal noise and shot noise at the receiver and the laser relative intensity (RIN) noise. For a system with an RF bandwidth given by B, the thermal noise power is given by

$$N_{o,\text{th}} = 4kTF_n B = \text{RIN}_{o,\text{th}} I_{dc}^2 R_{\text{out}} B, \tag{13}$$

where k is the Boltzman constant and F_n is a noise factor that takes into account the contribution of all electronic components at the receiver. In (13), the noise power is defined as well in terms of an equivalent relative intensity noise given by

$$\text{RIN}_{o,\text{th}} = \frac{4kTF_n}{R_{\text{out}} I_{dc}^2}. \tag{14}$$

The shot noise power is given by

$$N_{\text{shot}} = 2eI_{dc} R_{\text{out}} B = \text{RIN}_{\text{shot}} I_{dc}^2 B R_{\text{out}}, \tag{15}$$

where e represents the charge of an electron. As with the thermal noise, the shot noise power is defined as well in terms of an equivalent relative intensity noise given by

$$\text{RIN}_{\text{shot}} = \frac{2e}{I_{dc}}. \tag{16}$$

Finally, the laser noise is directly defined through its relative intensity noise parameter

$$N_{\text{laser}} = \text{RIN}_{\text{laser}} I_{dc}^2 R_{\text{out}} B. \tag{17}$$

The overall noise contribution can be represented by

$$N_{\text{out}} = N_{o,\text{th}} + N_{\text{shot}} + N_{\text{laser}} = \text{RIN}_{\text{tot}} I_{dc}^2 R_{\text{out}} B, \tag{18}$$

where $\text{RIN}_{\text{tot}} = \text{RIN}_{o,\text{th}} + \text{RIN}_{\text{shot}} + \text{RIN}_{\text{laser}}$. In general, more contributions to the noise will have to be considered for a more complex system including the noise terms from filters and amplifiers. A detailed treatment of this is presented in [12].

Dynamic range. For a given RF gain, Eq. (1) implies that a higher output RF power will be achieved by increasing the input RF power. Unfortunately, the input RF power cannot be increased at will since nonlinear terms start to appear in the output RF spectrum that can distort the signal. The dynamic range gives a measure of how much RF power can be injected into an MWPL before the effects of nonlinear terms become comparable to the link noise. Figure 4 reproduces again the configuration of a simple MWPL but this time the input and output RF signals are outlined, and an external modulation configuration is considered.
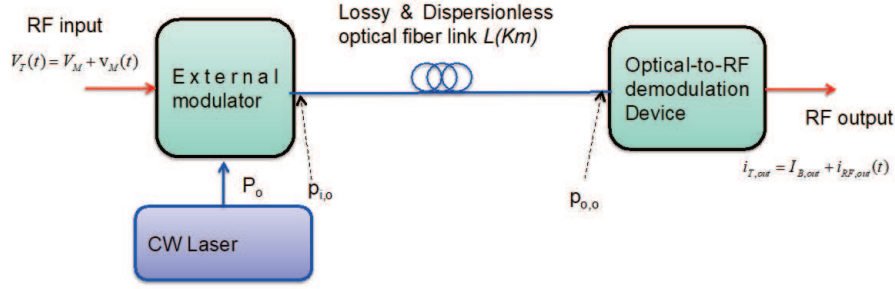
Figure 4   (Color online) Simple MWPL configuration showing explicitly the input and output electronic signals.

Let us assume that it is possible to establish a relationship between the output current and the input voltage by means of a function f [6],

$$
\begin{aligned}
i_{T,\text{out}} = f[V] &= f\left[V_M + v_M(t)\right] \\
&= f(V_M) + \left(\frac{\mathrm{d}f}{\mathrm{d}V}\right)_{V_M} v_M(t) + \frac{1}{2!}\left(\frac{\mathrm{d}^2 f}{\mathrm{d}V^2}\right)_{V_M} v_M^2(t) + \frac{1}{3!}\left(\frac{\mathrm{d}^3 f}{\mathrm{d}V^3}\right)_{V_M} v_M^3(t) + \cdots \\
&= I_{B,\text{out}} + f_1 v_M(t) + f_2 v_M^2(t) + f_3 v_M^3(t) + \cdots .
\end{aligned} \tag{19}
$$

In general, the f_i coefficients can be both time and frequency dependent but for the sake of simplicity we will, however, assume no such dependence in the following discussion. An analysis of the harmonic distortion due to nonlinearities can be performed if we assume a sinusoidal modulation for the input RF voltage where the amplitude v_s represents the RMS value delivered by the source,

$$
v_M(t) = \sqrt{2} v_s \cos \Omega_{\text{RF}} t. \tag{20}
$$

Substitution of (20) in (19) yields the following nonlinear harmonic distortion terms:

$$
\begin{aligned}
v_{\text{RF}}^2 &= \left(\sqrt{2} v_s \cos \Omega_{\text{RF}} t\right)^2 = \frac{1}{2}\left(\sqrt{2} v_s\right)^2 \left[1 + \cos\left(2\Omega_{\text{RF}} t\right)\right], \\
v_{\text{RF}}^3 &= \left(\sqrt{2} v_s \cos \Omega_{\text{RF}} t\right)^3 = \frac{1}{4}\left(\sqrt{2} v_s\right)^3 \left[3 \cos\left(\Omega_{\text{RF}} t\right) + \cos\left(3\Omega_{\text{RF}} t\right)\right], \\
v_{\text{RF}}^4 &= \left(\sqrt{2} v_s \cos \Omega_{\text{RF}} t\right)^4 = \frac{1}{8}\left(\sqrt{2} v_s\right)^4 \left[3 + 4\cos\left(2\Omega_{\text{RF}} t\right) + \cos\left(4\Omega_{\text{RF}} t\right)\right], \\
&\cdots
\end{aligned} \tag{21}
$$

Note from (21) and (19) that the f_k term contributes to the kth harmonic distortion term at $k\Omega_{\text{RF}} t$, but also contributes to terms with frequencies ranging from $(k-2)\Omega_{\text{RF}} t$ to $(k-2m)\Omega_{\text{RF}} t$ terms with an integer m and $k-2m > 0$. Substituting (21) into (19), we get

$$
\begin{aligned}
i_{T,\text{out}} = {}& I_{B,\text{out}} + \frac{f_2}{2}\left(\sqrt{2} v_s\right)^2 + \frac{6 f_4}{16}\left(\sqrt{2} v_s\right)^4 + \cdots \\
& + \left[f_1\left(\sqrt{2} v_s\right) + \frac{3 f_3}{4}\left(\sqrt{2} v_s\right)^3 + \frac{10 f_5}{16}\left(\sqrt{2} v_s\right)^5 + \cdots\right] \cos\left(\Omega_{\text{RF}} t\right) \\
& + \left[\frac{f_2}{2}\left(\sqrt{2} v_s\right)^2 + \frac{4 f_4}{8}\left(\sqrt{2} v_s\right)^4 + \cdots\right] \cos\left(2\Omega_{\text{RF}} t\right) \\
& + \left[\frac{f_3}{4}\left(\sqrt{2} v_s\right)^3 + \frac{5 f_5}{16}\left(\sqrt{2} v_s\right)^5 + \cdots\right] \cos\left(3\Omega_{\text{RF}} t\right) + \cdots .
\end{aligned} \tag{22}
$$

The inspection of (22) reveals several interesting features. In the first place, the dependence between the output RF current $i_{T,\text{out}}$ and the input RF voltage v_s is only linear if the contributions from f_i, $i > 1$ can be neglected, otherwise harmonic distortion terms must be considered. However, in practice usually, $f_1 > f_2 > f_3 > \cdots$, so within a reasonable range of v_s the fundamental tone is much larger than the second harmonic which in turn is larger than the third harmonic, etc. Thus, in practice, for the majority of systems we need only to consider f_1, f_2, and f_3 in the series expansion given in (21). Note that the

largest coefficient for the n-th harmonic contains a v_s^n term. Hence, the RF power of the n-th harmonic increases at least n times faster than that of the fundamental. It is also interesting to point out that the output current DC component is shifted from the $I_{B,\mathrm{out}}$ value by a term proportional to f_2.

The total output RF power can be computed from (22) [5,6],

$$
\begin{aligned}
&p_o = \tfrac{\Omega_{\mathrm{RF}}}{2\pi} \int_0^{2\pi/\Omega_{\mathrm{RF}}} i_{T,\mathrm{out}}^2 R_{\mathrm{out}} \mathrm{d}t = \sum_k p_k, \\
&p_1 = 4f_1^2 R_{\mathrm{out}} R_{\mathrm{in}} p_i, \\
&p_2 = 8f_2^2 R_{\mathrm{out}} R_{\mathrm{in}}^2 p_i^2, \\
&p_3 = 16f_3^2 R_{\mathrm{out}} R_{\mathrm{in}}^3 p_i^3, \\
&\cdots \\
&p_k = 2^{k+1} f_k^2 R_{\mathrm{out}} R_{\mathrm{in}}^k p_i^k.
\end{aligned}
\tag{23}
$$

That is, the total RF output power is the sum of the RF powers of the individual terms in (22) since the cross-terms yield zero average:

$$
\frac{\Omega_{\mathrm{RF}}}{2\pi} \int_0^{2\pi/\Omega_{\mathrm{RF}}} \cos\left(m\Omega_{\mathrm{RF}}t\right) \cos\left(n\Omega_{\mathrm{RF}}t\right)\mathrm{d}t = \delta_{m,n}. \tag{24}
$$

For the following discussion, it is useful to express the relationships given in (23) in logarithmic form. Thus, we have

$$
\begin{aligned}
&P_1\,(\mathrm{dBm}) = P_i\,(\mathrm{dBm}) + 10\log_{10}\left(4f_1^2 R_{\mathrm{out}} R_{\mathrm{in}}\right), \\
&P_2\,(\mathrm{dBm}) = 2P_i\,(\mathrm{dBm}) + 10\log_{10}\left(8f_2^2 R_{\mathrm{out}} R_{\mathrm{in}}^2\right), \\
&P_3\,(\mathrm{dBm}) = 3P_i\,(\mathrm{dBm}) + 10\log_{10}\left(16f_3^2 R_{\mathrm{out}} R_{\mathrm{in}}^3\right), \\
&\cdots \\
&P_k\,(\mathrm{dBm}) = kP_i\,(\mathrm{dBm}) + 10\log_{10}\left(2^{k+1} f_k^2 R_{\mathrm{out}} R_i^k\right).
\end{aligned}
\tag{25}
$$

A similar procedure can be followed for the analysis of the intermodulation distortion. In this case, one has to assume at least a two-tone RF input to the system,

$$
v_M(t) = \sqrt{2}v_s\left[\cos\Omega_{\mathrm{RF},1}t + \cos\Omega_{\mathrm{RF},2}t\right]. \tag{26}
$$

If substituted in (10) taking up to the third order term shows the appearance of the second order terms in $2\Omega_1, 2\Omega_2, \Omega_1+\Omega_2, \Omega_1-\Omega_2$, and the third order terms in $3\Omega_1, 3\Omega_2, 2\Omega_1+\Omega_2, 2\Omega_1-\Omega_2, 2\Omega_2+\Omega_1, 2\Omega_2-\Omega_1$. In the so-called sub-octave applications where the bandwidth is less than one octave, the 2nd order distortion terms fell out of the band and can be filtered out. Of the remaining terms, the sum terms can be usually neglected so the limitation in the dynamic range comes from the terms in $2\Omega_1 - \Omega_2$ and $2\Omega_2 - \Omega_1$ which are usually known as the third order intermodulation distortion (IMD3) terms. A straightforward but lengthy calculation renders for the amplitude of the $\cos(2\Omega_2 - \Omega_1)t$ term the value $3f_3\left(\sqrt{2}v_s\right)^3/4$ which is three times bigger than the corresponding third order harmonic distortion (HD3) term given by (22). Thus, the power of the IMD3 terms is 9 times higher than that of the HD3 terms.

In general, the calculation of an analytic expression of $f(V)$ for an end-to-end link is not possible, but a simplified analysis can be carried out by identifying the component that causes most of the nonlinear distortion and treating the rest of the link as linear. In many cases, this component is the external modulator. Alternatively, a numerical calculation for the end-to-end function $f(V)$ can be employed.

In any case, it is possible to represent the values of the output RF power values for the signal, harmonic, and intermodulation distortion terms as a function of the RF power of the input signal to the system. This is usually done in logarithmic form, as given by (25). Figure 5 shows a typical representation that we will take as a reference in order to explain several important parameters related to the dynamic range. In particular, we have represented the straight lines corresponding to the RF signal or fundamental, the second order harmonic distortion (HD2), IMD3 and HD3. The lines show a different slope as expected from (24) with a value of one for the fundamental term, two for HD2, and three for IMD3 and HD3. We have also plotted the noise floor $\eta = \mathrm{RIN}_{\mathrm{out}} I_{dc}^2 R_{\mathrm{out}}$ (W/Hz) due to the contributions of all the relevant noise sources.
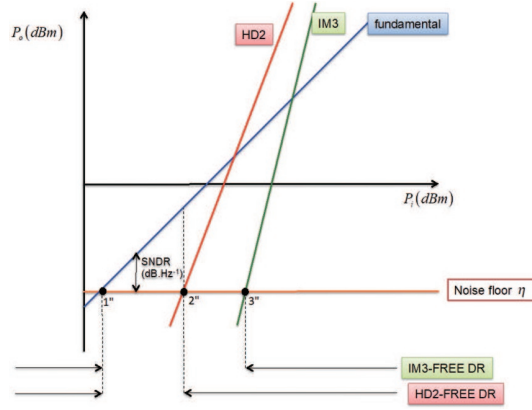
Figure 5 (Color online) Logarithmic representation of the output RF power vs. input RF power for the signal (fundamental), second and third order distortion terms in an MWPL.

For the region of input powers within points 1 and 2, the relevant distortion source is noise and the system performance is given in terms of the signal to noise dynamic range or SNDR. As it can be immediately observed this value is obtained at any point in this region as the difference between the output RF power level corresponding to the fundamental and the noise floor level. SNDR is given in dB·Hz as the noise floor is given per Hz of bandwidth. From this value and the knowledge of the system RF bandwidth B it is straightforward to obtain the real SNR limited by noise:

$$\text{SNR (dB)} = \text{SNDR (dB)} - 10\log_{10}\left([B \text{ (Hz)}]\right). \tag{27}$$

When the input RF power reaches the value given by point 2, then the second order nonlinear distortion becomes the dominant factor over the noise. The input power margin between points 1 and 2 generates an output signal free from the second order nonlinearities. This input power range is known as the second order spurious free dynamic range (SFDR$_2$). In a similar way, the input power margin between points 1 and 3 generates an output signal free from the third order nonlinearities; hence this power range is known as the third order spurious free dynamic range (SFDR$_3$).

The dependence of SFDR$_2$ on the system bandwidth can be computed as follows referring to Figure 5. From (25) we know that

$$\begin{aligned} P_1 \text{ (dBm)} &= P_i \text{ (dBm)} + 10\log_{10}\left(4f_1^2 R_{\text{out}} R_{\text{in}}\right) \rightarrow p_1 = c_1 p_i, \\ P_2 \text{ (dBm)} &= 2P_i \text{ (dBm)} + 10\log_{10}\left(8f_2^2 R_{\text{out}} R_{\text{in}}^2\right) \rightarrow p_2 = c_2 p_i^2. \end{aligned} \tag{28}$$

But at point 2, the RF power for HD2 equals that of the noise per unit bandwidth, we have

$$p_2 = c_2 p_i^2 = \eta \rightarrow p_i = \sqrt{\frac{\eta}{c_2}}. \tag{29}$$

When substituted into the first expression in (28), we have

$$p_1 = c_1 p_i = \sqrt{\frac{c_1^2 \eta}{c_2}} \rightarrow \text{SFDR}_2 = \frac{p_1}{\eta} = \sqrt{\frac{c_1^2}{c_2 \eta}}. \tag{30}$$

Since p_1 is in W, then the units of SFDR$_2$ are Hz$^{1/2}$ or dB·Hz$^{1/2}$ if we express it in logarithmic form. To distinguish the fact that this quantity is for a 1 Hz bandwidth we will name it SFDR$_2^{1\text{Hz}}$. If the second order nonlinearities are the limiting factor, then SFDR$_2$ for the system bandwidth of B Hz can be computed by

$$\text{SFDR}_2 \text{ (dB)} = \text{SFDR}_2^{1\text{Hz}} \text{ (dB)} - 5\log_{10}\left([B \text{ (Hz)}]\right). \tag{31}$$

A similar procedure can be employed to obtain the system dependence of SFDR$_3^{1\text{Hz}}$ on the system bandwidth. Again, from (25) we know
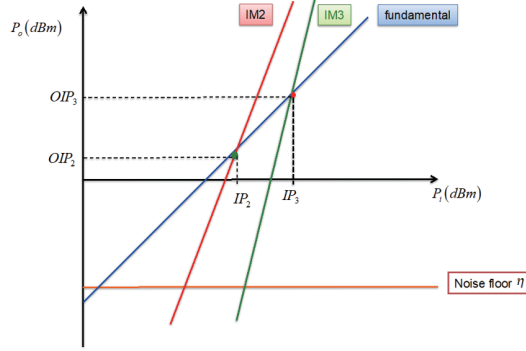
$$p_1 = c_1 p_i,$$

Figure 6 (Color online) The second and third order optical interception points for the distortion terms in an MWPL.

$$p_3 = c_3 p_i^3. \tag{32}$$

According to (1) $c_1 = G_{\mathrm{RF}}$. But at point 3 the RF power for IMD3 equals that of the noise per unit bandwidth, we have

$$p_3 = c_3 p_i^3 = \eta \to p_i = \sqrt[3]{\frac{\eta}{c_3}}. \tag{33}$$

When substituted into the first expression in (32), we have

$$p_1 = c_1 p_i = \sqrt[3]{\frac{c_1^3 \eta}{c_3}} \to \mathrm{SFDR}_3^{1\mathrm{Hz}} = \frac{p_1}{\eta} = \sqrt[3]{\frac{c_1^3}{c_3 \eta^2}}. \tag{34}$$

Since p_1 is in W, then the units of $\mathrm{SFDR}_3^{1\mathrm{Hz}}$ are $\mathrm{Hz}^{2/3}$ or $\mathrm{dB \cdot Hz}^{2/3}$ if we express it in logarithmic form. If the third order nonlinearities are the limiting factor (for example in a sub-octave system), then the SFDR_3 for a system bandwidth B can be computed by

$$\mathrm{SFDR}_3(\mathrm{dB}) = \mathrm{SFDR}_3^{1\mathrm{Hz}}(\mathrm{dB}) - \frac{20}{3} \log_{10}([B \ (\mathrm{Hz})]). \tag{35}$$

In practice, the values of SFDR_2 and SFDR_3 are usually computed through the so-called interception points, which are shown in Figure 6.

The interception points $(\mathrm{IIP}_2, \mathrm{OIP}_2)$ and $(\mathrm{IIP}_3, \mathrm{OIP}_3)$ are the intersection between the lines representing the fundamental and those representing the second and third order distortions, respectively. These points can be easily obtained after experimental measurements. Referring to Figure 6 and (25),

$$\left. \begin{array}{l} \mathrm{OIP}_2 = c_1 \mathrm{IP}_2 \\ \mathrm{OIP}_2 = c_2 \mathrm{IP}_2^2 \end{array} \right\} \Rightarrow \mathrm{IP}_2 = \frac{c_1}{c_2}, \\ \left. \begin{array}{l} \mathrm{OIP}_3 = c_1 \mathrm{IP}_3 \\ \mathrm{OIP}_3 = c_3 \mathrm{IP}_3^3 \end{array} \right\} \Rightarrow \mathrm{IP}_3 = \sqrt{\frac{c_1}{c_3}}. \tag{36}$$

When substituted in (30) and (34), we have

$$\mathrm{SFDR}_2^{1\mathrm{Hz}} = \sqrt{\frac{c_1^2}{\eta c_2}} = \sqrt{\mathrm{IP}_2 \left(\frac{c_1}{\eta}\right)} = \sqrt{\frac{G_{\mathrm{RF}} \mathrm{IP}_2}{\eta}} = \sqrt{\frac{\mathrm{OIP}_2}{\eta}}, \\ \mathrm{SFDR}_2 = \sqrt{\frac{G_{\mathrm{RF}} \mathrm{IP}_2}{\eta B}} = \sqrt{\frac{\mathrm{OIP}_2}{\eta B}} = \sqrt{\frac{\mathrm{OIP}_2}{N_{\mathrm{out}}}}, \tag{37}$$

$$\mathrm{SFDR}_3^{1\mathrm{Hz}} = \sqrt[3]{\frac{c_1^3}{\eta^2 c_3}} = \sqrt[3]{\frac{c_1^2}{\eta^2} \mathrm{IP}_3^2} = \sqrt[3]{\frac{G_{\mathrm{RF}}^2 \mathrm{IP}_3^2}{\eta^2}} = \left(\frac{\mathrm{OIP}_3}{\eta}\right)^{2/3}, \\ \mathrm{SFDR}_3 = \sqrt[3]{\frac{G_{\mathrm{RF}}^2 \mathrm{IP}_3^2}{\eta^2 B^2}} = \left(\frac{\mathrm{OIP}_3}{\eta B}\right)^{2/3} = \left(\frac{\mathrm{OIP}_3}{N_{\mathrm{out}}}\right)^{2/3}. \tag{38}$$

Or, in logarithmic form,

$$
\begin{aligned}
\mathrm{SDFR}_2 \ (\mathrm{dB}) &= \frac{\mathrm{IP}_2 \ (\mathrm{dBm}) + G_{\mathrm{RF}} \ (\mathrm{dB}) - N_{\mathrm{out}} \ (\mathrm{dBm})}{2} \\
&= \frac{\mathrm{OIP}_2 \ (\mathrm{dBm}) - N_{\mathrm{out}} \ (\mathrm{dBm})}{2},
\end{aligned}
\tag{39}
$$

$$
\begin{aligned}
\mathrm{SDFR}_3 \ (\mathrm{dB}) &= \frac{2}{3} \left[\mathrm{IP}_3 \ (\mathrm{dBm}) + G_{\mathrm{RF}} \ (\mathrm{dB}) - N_{\mathrm{out}} \ (\mathrm{dBm}) \right] \\
&= \frac{2}{3} \left[\mathrm{OIP}_3 \ (\mathrm{dBm}) - N_{\mathrm{out}} \ (\mathrm{dBm}) \right].
\end{aligned}
\tag{40}
$$

In summary, in this section, we have reviewed the basic concepts of MWPLs including the general architecture and the performance measures including the link gain, noise figure, and the spurious free dynamic ranges for both the second order harmonic distortions and the third order intermodulation distortions. The same analysis can also be applied to microwave photonic filters since, ideally, a microwave photonic filter is a linear system which is expected to have a large dynamic range. The implementation of a microwave photonic filter, however, involves an optical modulator, which is inherently a nonlinear device, which would make the dynamic range decrease. The techniques developed for MWPLs can be applied to increase the dynamic range of microwave photonic filters.

3 Photonic-assisted microwave signal generation

The primary motivation of generating microwave signals in the optical domain based on photonics is to generate high frequency, frequency tunable, and low phase noise microwave signals which cannot be easily generated based on pure electronics. Numerous approaches have been proposed for the last few decades. In general, all these approaches can be classified into two categories, microwave generation based on heterodyne beating of two optical waves, and microwave generation based on optoelectronic oscillation.

3.1 Microwave generation based on heterodyne beating

The fundamental concept behind the generation of microwave signals based on photonics is to beat two optical waves at a photodetector. If the two wavelengths are phase correlated, a low-phase noise heterodyne beat signal with its frequency corresponding to the wavelength spacing is generated. The key is to generate two wavelengths that are phase correlated, to ensure low-phase noise microwave signal generation. In general, there are three main approaches that are employed to generate two phase-correlated wavelengths, to beat to generate a high frequency and low phase noise microwave signal. These techniques include optical injection locking [13–18], optical phase locked loop [19–27], optical external modulation [28–37], and optoelectronic oscillation [38–52].

Figure 7 shows an injection-locking-based microwave signal generation system [13–18]. As can be seen, a laser diode is directly modulated by a low-frequency microwave modulation signal. Due to frequency modulation at the laser diode, a frequency-modulated optical signal with multiple sidebands is generated. By injecting the frequency-modulated optical signal into two slave laser diodes, with one sideband to injection lock one laser diode, two wavelengths corresponding to the two sidebands are selected. Since the two wavelengths are generated due to direct modulation at the master laser diode with the same microwave source, the two wavelengths are phase correlated. The beating of the two wavelengths at a photodetector will generate a low phase noise microwave signal. Figure 7 shows an example of an injection locking system for microwave signal generation. As can be seen, a low-frequency microwave modulation signal is applied to the master laser diode to generate a frequency-modulated optical signal. If the two slave laser diodes have free running wavelengths close to those of the ±2nd sidebands, when the frequency-modulated optical signal is injected into the two slave laser diodes, the wavelengths from the slave laser diodes are injection locked by the ±2nd sidebands. By beating the two wavelengths at the photodetector, a microwave signal with its frequency being 4 times the frequency of the microwave modulation signal is generated. Note that the system in Figure 7 can not only generate a high frequency and low phase noise microwave signal, but also distribute the microwave signal by transmitting the two wavelengths over a single-mode fiber (SMF). By beating the two wavelengths remotely, a microwave signal at a remote location can be generated.
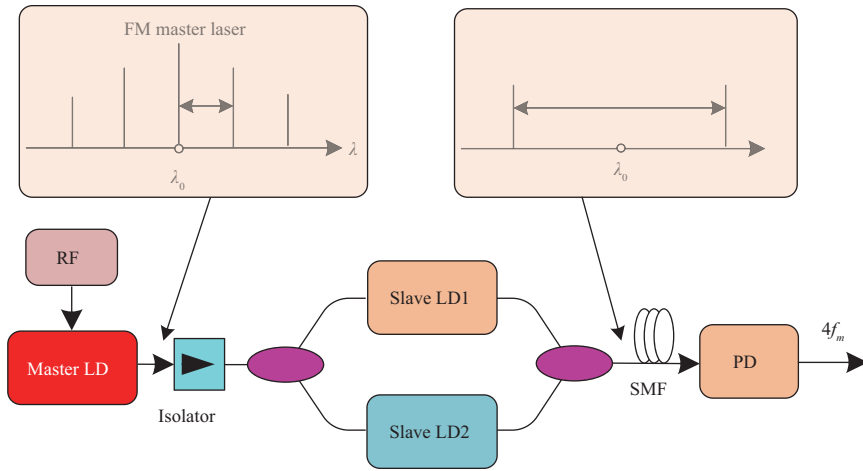
Figure 7 (Color online) Optical injection locking of two wavelengths for microwave signal generation and transmission. The master laser diode is directly modulated by a microwave modulation signal with its output injected into the two slave laser diodes. The slave laser diodes are injection-locked by the ±2nd sidebands from the output of the master laser diode. The beat at the photodetector will generate a microwave signal with a frequency that is 4 times that of the microwave modulation signal.
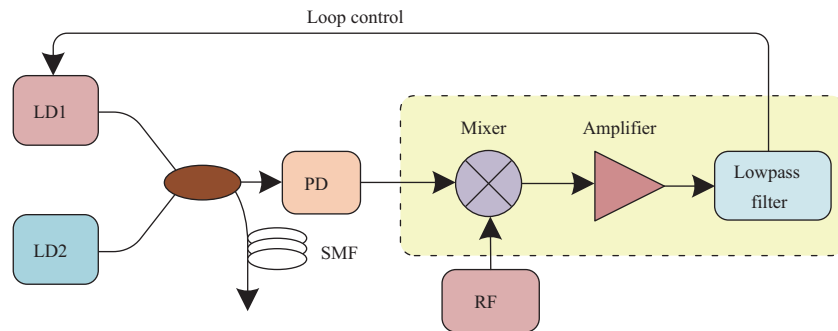
Figure 8 (Color online) Optical phase lock loop to phase lock two optical wavelengths for microwave generation and transmission. LD: laser diode. PD: photodetector.

A limitation of the approach is that once the salve laser diodes are selected, the free running wavelengths are fixed; thus the frequency of the generated microwave signal is not tunable or has a very limited frequency tunable range.

A second approach to generate two phase-correlated wavelengths and by beating the two wavelengths to generate a low phase noise microwave signal is to use an optical phase lock loop [19–27]. Assume two free running laser diodes have a wavelength spacing corresponding to a frequency f_m. Since the wavelengths are not phase locked, the phase noise terms from the two laser diodes after beating at a photodetector will be translated to the generated microwave signal. To make the two wavelengths phase correlated, an optical phase lock loop can be employed. As can be seen from Figure 8, the two wavelengths from the two laser diodes are applied to a photodetector to generate a beat note. The beat signal is mixed with a microwave reference signal. After low-pass filtering, a current or voltage signal that is proportional to the phase difference between the two microwave signals is generated, which is fed back to one laser diode to control its phase to be identical to that of another laser diode. If the loop length is sufficiently short, the two wavelengths can be effectively phase locked. Again, the microwave signal can be generated remotely. If the two phase-locked wavelengths are transmitted over a fiber and beat at a photodetector, then a microwave signal at a remote location can be generated.

Again, the limitation of the approach is that the frequency has limited tunability since the wavelengths of the laser diodes are fixed or have limited tunability. A solution is to use the external modulation approach in which the frequency of the generated microwave signal can be widely tunable.

A third approach to generate two phase-correlated wavelengths and by beating the two wavelengths to generate a low phase noise microwave signal is to use external modulation [28–37]. Figure 9 shows the approach to generating a microwave signal based on optical external modulation [31, 34, 37]. The key advantage of this approach is that the frequency of the generated microwave signal can be continuously
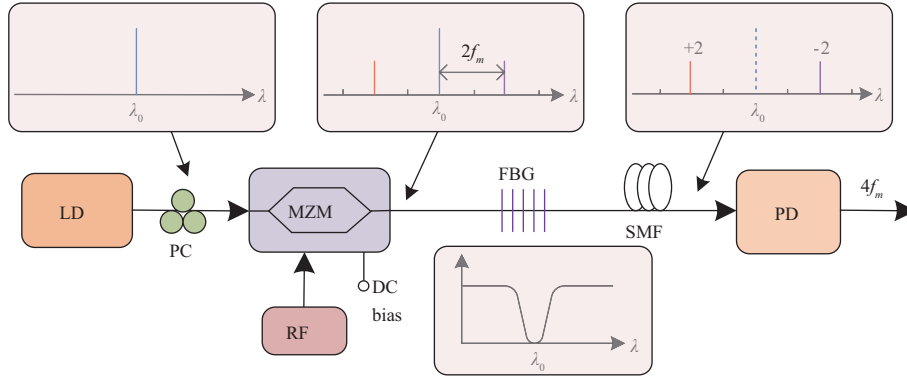
Figure 9 (Color online) Microwave signal generation based on external modulation using an MZM and a wavelength-fixed optical filter, such as an FBG. MZM: Mach-Zehnder modulator; FBG: fiber Bragg grating; PD: photodetector.

tunable. As shown in Figure 9, a linearly polarized light wave from a laser diode is applied to an MZM through a polarization controller. The polarization controller is employed to control the polarization direction of the light wave from the laser diode to be aligned with the principal axis of the MZM to minimize the polarization-dependent loss. A low frequency microwave modulation signal is applied to the MZM via its RF port to modulate the light wave. By biasing the MZM at the minimum transmission point (MITP), the odd order sidebands are fully suppressed. By using an optical notch filter with its center wavelength located at the wavelength of the optical carrier, such as a fiber Bragg grating (FBG), the optical carrier is filtered out, and only the two $\pm$2nd sidebands are obtained (the $\pm$4th and higher even order sidebands are very weak and are ignored). By beating the two sidebands at a photodetector, a microwave signal with a frequency that is four times the frequency of the microwave modulation signal is generated. Again, by transmitting the two $\pm$2nd sidebands over a fiber and beating the two sidebands remotely at a photodetector, a microwave signal at a remote location is generated.

Note that the MZM can be replaced by a phase modulator (PM). The advantage of using a PM is that a PM is not biased; thus the bias drifting problem does not exist [32]. In addition, one may use two cascaded MZMs, to generate a microwave signal with a higher frequency [33]. For example, a microwave signal with a frequency multiplication factor up to 12 can be generated [34]. The use of this approach to generate a sub-THz signal was also reported [35, 36]. Phase-noise analysis of a microwave signal with external modulation was also studied theoretically and experimentally [37].

All the three approaches based on heterodyne beating of two wavelengths to generate a high frequency and low-phase noise microwave signal need a microwave reference source. The phase noise of the generated microwave signal is directly related to the phase noise of the reference microwave source. If the frequency multiplication factor is N, the phase noise performance of the generated microwave signal will be deteriorated by $20\log_{10}N$ (dB) [38]. For example, if N is 4, then the phase noise performance is reduced by 12 dB. To generate a microwave signal with a very low phase noise, a microwave reference source with an ultra-low phase noise is needed, which makes the implementation highly costly. On the other hand, we may improve the phase noise performance through frequency division. For example, if the frequency of a microwave signal is divided by 4, then the phase noise performance is increased by 12 dB. The approach was employed to generate an ultrastable microwave signal with its stability comparable to the best microwave oscillators, but without the need for cryogenic temperature control [39].

3.2 Microwave generation based on an optoelectronic oscillator

A solution to generate a low phase noise microwave signal without the need for a low-phase noise microwave reference source is to use an optoelectronic oscillator (OEO) [40–52]. An OEO is an optical and electronic hybrid system with an amplified feedback loop consisting of an optical path and an electrical path. For the optical path, the length can be made long thanks to the ultra-low loss of the state-of-the-art optical fibers; thus the Q factor of the feedback loop can be high, making the generated microwave signal have ultra-low phase noise. This is the key and unique feature of OEOs for low-phase noise microwave generation. Figure 10 shows the configuration of an OEO, which consists of a laser diode, a polarization controller, a Mach-Zehnder modulator, a length of single mode fiber, a microwave bandpass filter, an electronic amplifier (EA) to provide the loop gain, and a photodetector. A light wave from the laser
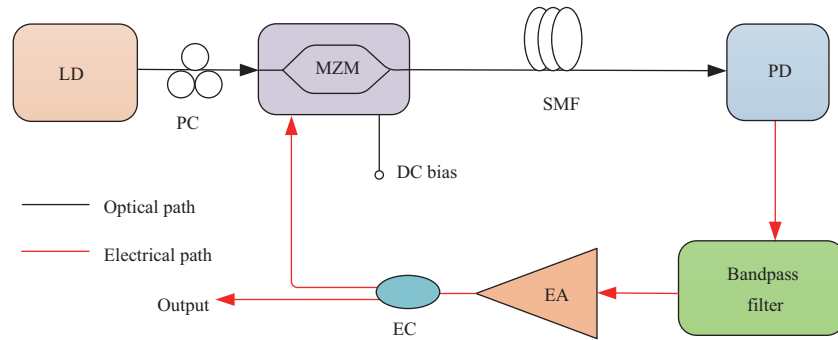
Figure 10 (Color online) An optoelectronic oscillator. LD: laser diode; MZM: Mach-Zehnder modulator; SMF: single mode fiber; PD: photodetector; EA: electronic amplifier.

diode is sent to the Mach-Zehnder modulator through the polarization controller. Again, the polarization controller is used to control the polarization state of the incident light wave to the Mach-Zehnder modulator, to minimize the polarization-dependent loss. The modulated light wave is then sent to the photodetector after passing through the single mode fiber. At the output of the photodetector, the optical signal is converted to a microwave signal, which is then filtered by the microwave bandpass filter, amplified by the electronic amplifier and sent back to the Mach-Zehnder modulator, to close the feedback loop. If the gain provided by the electronic amplifier is sufficiently large to make the loop gain greater than the loop loss, oscillation will start. The frequency of the generated microwave signal is equal to the center frequency of the passband of the microwave bandpass filter.

Since the frequency tunability of an electronic microwave filter is very limited, one may use a microwave photonic filter to perform frequency tuning and mode selection. A microwave photonic filter can have a large frequency tunable range as compared to an electronic microwave filter. Figure 11 shows a frequency-tunable optoelectronic oscillator in which a phase-shifted fiber Bragg grating (PS-FBG) is employed to implement, jointly with a phase modulator and a photodetector, a frequency-tunable microwave photonic filter [46]. As can be seen, the light wave from a tunable laser source (TLS) is directed to a phase modulator, where a double-sideband plus carrier (DSB+C) optical signal is generated. Note the DSB+C signal generated using a phase modulator is different from a DSB+C generated using a Mach-Zehnder modulator. A DSB+C signal generated by a phase modulator has two first sidebands that are out of phase. Thus, by applying a phase-modulated DSB+C signal to a photodetector, no microwave signal will be generated except a DC, since the beating between one sideband with the optical carrier will generate a microwave signal that will be fully canceled by another microwave signal resulting from the beating between the other sideband with the optical carrier. To convert a phase-modulated DSB+C signal to an intensity-modulated signal, a simple way is to remove one sideband. As can be seen, the DSB+C signal is sent to a phase-shifted fiber Bragg grating where one sideband is removed due to the notch of the phase-shifted fiber Bragg grating, thus the phase-modulated DSB+C signal is converted to a single-sideband plus carrier (SSB+C) signal. The detection of the SSB+C at a photodetector will generate a microwave signal. The central frequency of the microwave photonic filter is equal to the wavelength spacing between the notch wavelength and the wavelength of the optical carrier. Thus, by tuning either the wavelength of the optical carrier from the tunable laser source or the notch wavelength, the frequency of the microwave filter can be tuned.

The key challenge in implementing an optoelectronic oscillator using a long fiber is the mode selection difficulty. An optoelectronic oscillator with a long feedback loop has a large number of closely spaced longitudinal modes separated by its free spectral range (FSR) within the passband of the microwave or microwave photonic bandpass filter. To enable single mode oscillation, a microwave or microwave photonic filter with an ultra-narrow passband must be used to select a single mode, which is very challenging considering the small free spectral range of a long optoelectronic oscillator loop. The use of dual or multiple feedback loops may make an optoelectronic oscillator have a large FSR due to the Vernier effect [42], but the implementation is more complicated and the frequency tunability is limited.

Instead of using a long feedback loop to increase the Q factor, one may use a high Q factor optical resonator to serve as a mode selection component. For example, OEwaves has demonstrated a miniaturized optoelectronic oscillator in which the long fiber was replaced by a high Q factor whispering gallery mode (WGM) resonator [47]. OEwaves has developed mm-scale whispering gallery mode resonators with
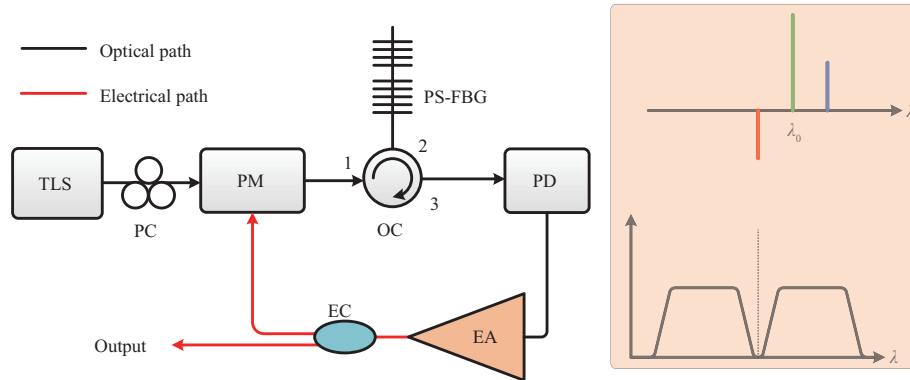
Figure 11 (Color online) A frequency tunable OEO. The oscillation frequency of the OEO is determined by the central frequency of the microwave photonic filter. TLS: tunable laser source; PC: polarization controller; PM: phase modulator; PD: photodetector; EA: electronic amplifier; PS-FBG: phase-shifted fiber Bragg grating.
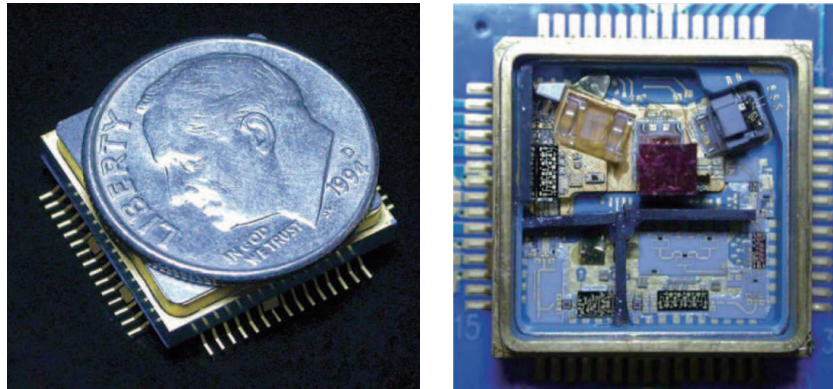

Figure 12 (Color online) Miniature optoelectronic oscillator incorporating a lithium niobate whispering gallery mode (WGM) resonator (from OEwaves [47]).

the Q factor and finesse in excess of 10^{11} and 10^7, which are beyond what is possible with bulk or integrated optical resonators. By using a whispering gallery mode resonator, a microwave signal with a phase noise as low as -110 dBc/Hz at 10 kHz offset was generated. Figure 12 shows an OEwaves miniature optoelectronic oscillator incorporating a lithium niobate WGM resonator in the optoelectronic oscillator loop. In addition to the ease of mode selection, the use of a whispering gallery mode resonator can also significantly reduce the size of the optoelectronic oscillator, making an optoelectronic oscillator to have a small form factor, a feature that is highly needed for airborne applications.

The use of a WGM resonator can solve the mode selection problem, but the implementation is still challenging especially the coupling between a fiber and a whispering gallery mode resonator, making the optoelectronic oscillator highly costly. In addition, the spectral response of a whispering gallery mode resonator is fixed or with very limited tunability, thus the frequency of the generated microwave signal by a whispering gallery mode resonator based optoelectronic oscillator has no or very limited frequency tunability.

Recently, a new concept, called parity time symmetry, has been introduced to the microwave photonics field [48, 49]. A parity-time (PT) symmetric system is a special non-Hermitian system in which its Hamiltonian possesses real eigenvalues [50–59]. The inherent mode selection feature has made the concept extremely useful for mode selection in a laser or an optoelectronic oscillator. The key advantage of using parity time symmetry in an optoelectronic oscillator is that high performance mode selection can be implemented, making stable single-mode oscillation possible while maintaining a high Q factor to ensure an ultra-low phase noise.

Figure 13 shows a parity-time symmetric optoelectronic oscillator in which two optoelectronic loops have identical geometry but with one having a gain coefficient and the other a loss coefficient, identical in magnitude, are implemented [48]. Once the gain/loss coefficient is greater than the coupling coefficient, the PT symmetry condition is broken, and the mode that has the highest gain is selected.
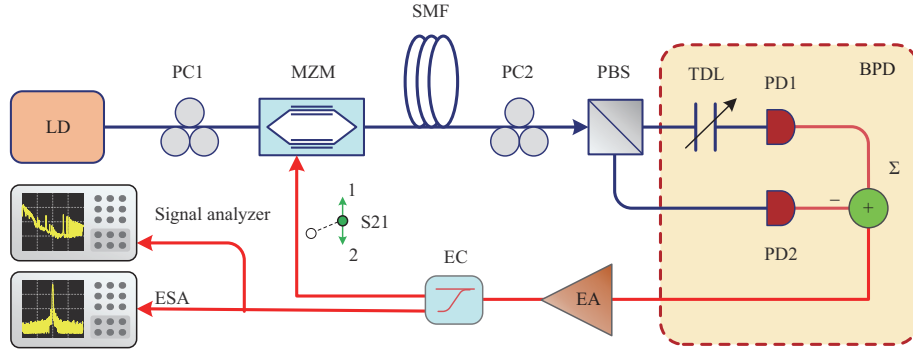
Figure 13 (Color online) Diagram of a PT-symmetric optoelectronic oscillator. LD: laser diode; PC: polarization controller; MZM: Mach-Zehnder modulator; SMF: single-mode fiber; PBS: polarization beam splitter; TDL: tunable delay line; PD: photodetector; BPD: balanced photodetector; Σ: microwave combiner; EA: electrical amplifier; ESA: electrical spectrum analyzer [48].

Mathematically, the coupled mode equations relating to the modes in the two loops are given by

$$\frac{\mathrm{d}a_n}{\mathrm{d}t} = -i\omega_n a_n + i\kappa b_n + \gamma_{a_n} a_n, \tag{41}$$

$$\frac{\mathrm{d}b_n}{\mathrm{d}t} = -i\omega_n b_n + i\kappa a_n + \gamma_{b_n} b_n, \tag{42}$$

where a_n and b_n are the amplitudes of the n-th modes in the gain and loss loops, respectively, ω_n is the eigenfrequency of the longitudinal modes of the two loops without PT symmetry coupling, κ is the coupling coefficient between the two loops, and γ_{a_n} and γ_{b_n} are the gain coefficients of the gain and loss loops for the n-th mode. By solving (41) and (42), we can get the eigenfrequencies of the PT symmetric system, given by

$$\omega_n^{(1,2)} = \omega_n + i\frac{\gamma_{a_n} + \gamma_{b_n}}{2} \pm \sqrt{\kappa_n^2 - \left(\frac{\gamma_{a_n} - \gamma_{b_n}}{2}\right)^2}. \tag{43}$$

Assuming that the exact PT symmetry condition is satisfied for one longitudinal mode, say $n = 0$, i.e., $\gamma_{a_0} = -\gamma_{b_0} = \gamma_0$, Eq. (43) can be written as

$$\omega_0^{(1,2)} = \omega_0 \pm \sqrt{\kappa_0^2 - \gamma_0^2}. \tag{44}$$

It can be seen from (44) that, when the gain/loss coefficient is smaller than the coupling coefficient, the two loops exhibit broken degeneracy with eigenfrequency splitting. However, when the gain/loss coefficient is greater than the coupling coefficient, the eigenfrequency becomes a complex number with a non-zero imaginary part. The electrical field can then be written as

$$E_0^{(1,2)} = \exp\left(\mathrm{j}\omega_0 t\right)\exp\left(\pm |g_0|\, t\right), \tag{45}$$

where $g_0 = \sqrt{\kappa_0^2 - \gamma_0^2}$. As can be seen from (45), parity-time symmetry is broken when the gain/loss coefficient is greater than the coupling coefficient. Amplifying and decaying modes with an identical frequency will be generated, and the amplifying mode would be the dominating mode that oscillates in the optoelectronic oscillator.

Stable single-mode oscillation supported by broken parity-time symmetry without the need of an ultra narrowband optical or microwave filter was evaluated experimentally based on the system shown in Figure 13 and the experimental results are shown in Figure 14 [48]. The two loops have an identical loop length of 9.166 km. Clearly, the loops are very long and a large number of closely spaced longitudinal modes exist in the gain spectrum of the optoelectronic loop. Without broken parity-time symmetry, the optoelectronic oscillator will oscillate in multimode. Figure 14(a) shows the spectrum of the microwave signal generated by the optoelectronic oscillator. It is clearly seen multiple mode oscillation is resulted. To achieve single-mode oscillation, enabled by the broken PT symmetry, the gain and loss in the two loops are tuned to be balanced and to be greater than the coupling coefficient, which is done by tuning the polarization controller before the polarization beam splitter (PBS). Figures 14(b)–(d) show the spectra
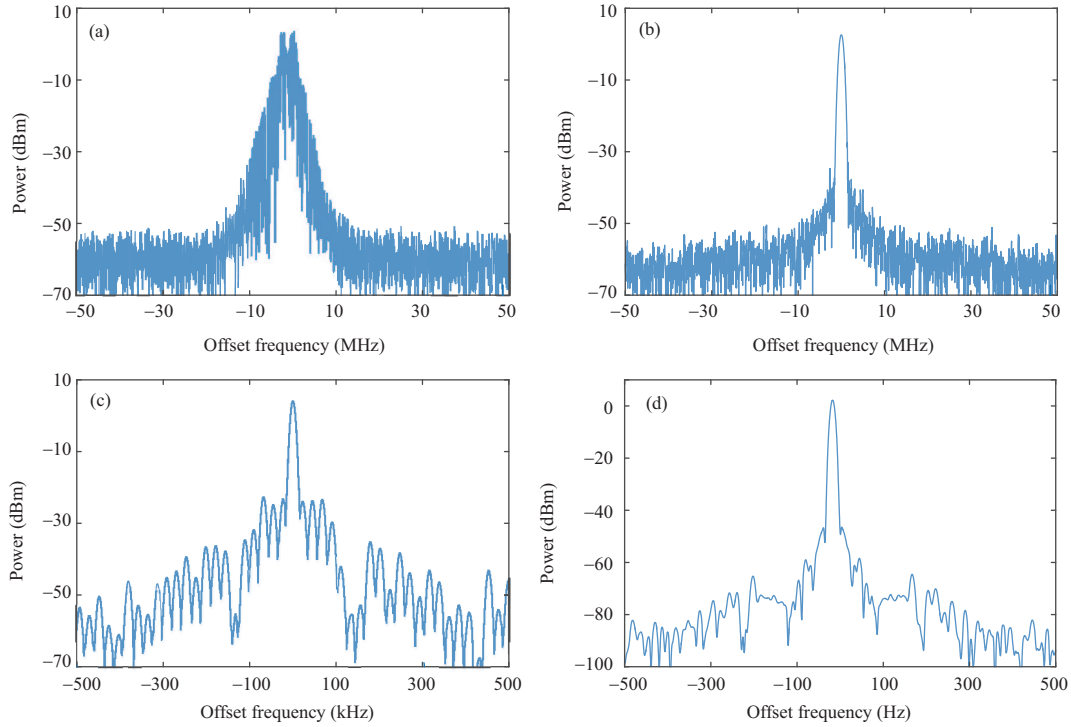
Figure 14 (Color online) The spectra of the microwave signals generated by the PT-symmetric optoelectronic oscillator. The spectra are measured at a central frequency of 9.867 GHz. (a) Multi-mode oscillation measured with an RBW of 3 MHz; (b) single-mode oscillation measured with an RBW of 3 MHz; (c) single-mode oscillation measured with an RBW of 9.1 kHz; (d) single-mode oscillation measured with an RBW of 9 Hz [48].

of the generated microwave signal measured at different resolution bandwidths (RBWs). Clearly, single-mode oscillation is achieved. Figure 14(b) shows the spectrum with a 100 MHz span and Figure 14(c) shows the spectrum with a 1 MHz span. The oscillating mode can be identified, and the mode spacing between the oscillating mode and the adjacent sidemode is measured to be 22.73 kHz and the oscillating mode is 26.4 dB higher than the highest sidemode. No mode hopping is observed in the experiment for a measurement time window of over ten minutes. Further reducing the frequency span to 1 kHz, the spectrum of the microwave signal is shown in Figure 14(d). It can be seen the microwave signal has an extremely narrow bandwidth thanks to the high Q factor of the optoelectronic loop due to the use of a long fiber in the optoelectronic oscillator.

The configuration shown in Figure 13 has two physically separated loops. To achieve broken parity-time symmetry, the lengths of the two loops must be made identical and the gain and loss must be balanced, which makes the implementation difficult. In addition, the stability is affected due to the use of two physically separated loops. The PT symmetry can also be implemented in a single physical resonator or loop [54, 60–62]. By using different multiplexing techniques, two equivalent loops with balanced gain and loss can be implemented. Figure 15 shows a configuration using a polarization-dependent Sagnac loop to implement two equivalent loops [61]. As can be seen, the Sagnac loop, consisting of a PBS and two polarization controllers, is employed to function equivalently to two mutually coupled feedback loops, with the gain, loss, and coupling coefficient being independently controllable by tuning the polarization controllers. Since only a single physical loop is used, the implementation is greatly simplified, and the stability is highly improved. The same concept has been employed to implement a single mode fiber ring laser, in which a single physical loop was employed to operate equivalently as two mutually coupled loops [63].

In addition to single-frequency and low phase-noise microwave signal generation, the generation of frequency-chirped microwave signals is also a topic of interest and can find applications in spread spectrum communications, radar, and microwave imaging. A review on the photonic generation of chirped microwave waveform has recently been published [64]. In general, a chirped microwave waveform can be generated based on spectral shaping and wavelength-to-time (SS-WTT) mapping, based on external modulation, and Fourier-domain mode locking [65]. Here a discussion on Fourier-domain mode locking
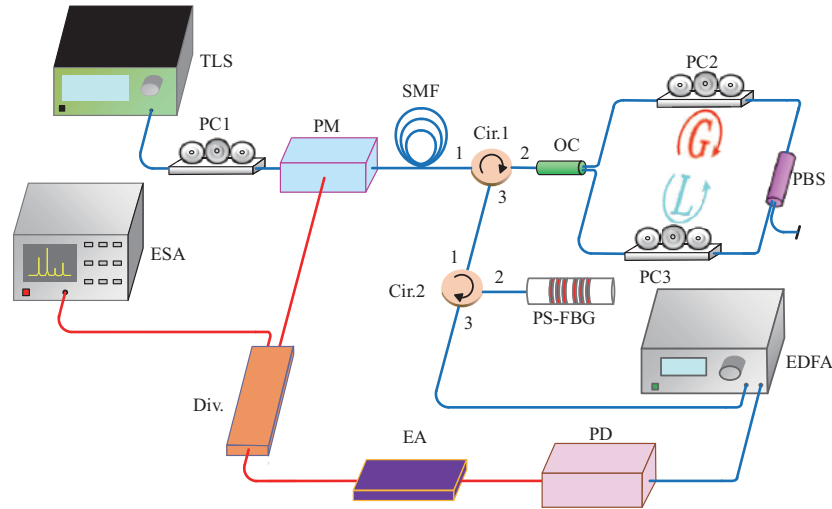
Figure 15   (Color online) A PT-symmetric optoelectronic oscillator with a single physical loop. TLS: tunable laser source; PC: polarization controller; PM: phase modulator; SMF: single-mode fiber; Cir.: circulator; OC: optical coupler; PBS: polarization beam splitter; PS-FBG: phase-shifted fiber Bragg grating; EDFA: erbium-doped fiber amplifier; PD: photodetector; EA: electrical amplifier; Div.: divider; ESA: electrical spectrum analyzer [62].
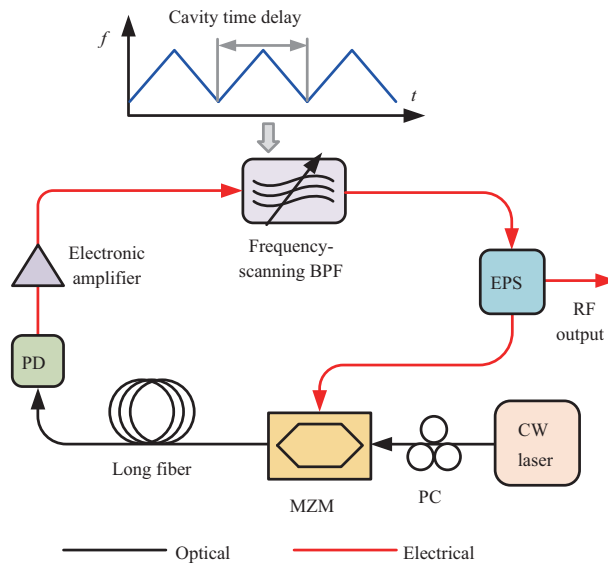

Figure 16   (Color online) A Fourier domain mode locked OEO for generating a chirped microwave waveform. EPS: electronic power splitter; MZM: Mach-Zehnder modulator; PC: polarization controller [64].

of an optoelectronic oscillator for chirped microwave signal generation is discussed.

A frequency chirped microwave waveform can also be generated by a frequency tunable optoelectronic oscillator through fast tuning the central frequency of a microwave bandpass filter in the loop, but the phase noise performance is poor due to the fact that the optoelectronic oscillator, when tuned from one frequency to another, will need a buildup time to stabilize the oscillation at the new frequency. A solution is to use Fourier domain mode locking. In a Fourier domain mode locked (FDML) OEO, all modes co-exist and are phase locked in the OEO loop. The switching from one mode to another mode does not need a buildup time, thus a chirped microwave waveform generated by a Fourier domain mode locked optoelectronic oscillator will not increase the low phase noise [65].

Figure 16 shows the schematic of a Fourier domain mode locked optoelectronic oscillator. It is similar to a regular optoelectronic oscillator except that the microwave bandpass filter is frequency tunable and the tuning is controlled by a sawtooth waveform with its repetition rate to be identical to the free spectral range of the optoelectronic loop or one of its multiples. The use of a Fourier domain mode locked laser to generate a linearly chirped optical waveform, and by beating the linearly chirped optical waveform

with an optical carrier, a linearly chirped microwave waveform with a much broader bandwidth could be generated [66].

In summary, microwave signal generation can be implemented either by heterodyne beating two phase-correlated wavelengths or using an optoelectronic oscillator. Since the use of an optoelectronic oscillator does not need a reference microwave source, it is an approach that is more suitable for applications where no reference microwave source is available. Similar to the heterodyne beating approaches where the microwave signal can be transmitted over a long fiber and generated at a remote location, an optoelectronic oscillator can also generate a microwave signal remotely. By taping part of the optical signal at the input of the photodetector, distributing the optical signal over a fiber, and detecting the signal at a second photodetector, a microwave signal can be generated at a remote location.

4 Photonic-assisted microwave signal processing

Microwave signals can also be processed in the optical domain to take advantage of the high frequency and wide bandwidth offered by modern photonics. Among the numerous signal processing functions, microwave filtering is one of the major functions and has been investigated for the last few years.

Microwave filters can be implemented in the optical domain using photonics to support operations at high frequency with a wide frequency tunable range [1, 67–69]. The implementations of microwave photonic filters can be, in general, classified into two categories: incoherent and coherent implementations. In general, an incoherent microwave photonic filter has a delay-line configuration with a finite impulse response (FIR) or infinite impulse response (IIR). In the configuration, a microwave signal is modulated on an optical carrier or optical carriers. The time delays and tap coefficients are produced in the optical domain and the time-delayed and weighted optical signals are detected at a photodetector. To avoid optical interferences, which are extremely sensitive to environmental changes, an incoherent light source that enables an incoherent combination of the time-delayed optical signals at a photodetector is needed. The limitation of an incoherent microwave photonic filter is that the weights or tap coefficients are all positive, making a microwave photonic filter have a low-pass response only, or special designs have to be employed to produce negative [70–72] or complex [73,74] coefficients. The use of nonuniformly spaced taps can also produce a delay line filter with equivalent negative or complex coefficients. A comprehensive study about the design and implementation of nonuniformly spaced microwave photonic filters was reported in [75]. Microwave photonic filters in the second category are implemented using an ultra-narrow band optical filter, to translate its frequency response in the optical domain to the microwave domain. Thus, the frequency response of the microwave filter is uniquely determined by the spectral response of the optical filter [76–78]. Instead of using an incoherent light source, a single-frequency light source is employed. The microwave photonic filters in the second category are also called coherent microwave photonic filters. Since the microwave photonic filters do not have a delay line configuration, optical interference is not an issue that would affect the stable operation of the filters.

Considering that microwave photonic filters based on a delay-line structure have been heavily studied and a few review or tutorial articles have been published [1,67–69], here, only coherent microwave photonic filters that translate the spectral response of an optical filter from the optical domain to the microwave domain will be discussed.

A general structure of a coherent microwave photonic filter is shown in Figure 17. An optical carrier from a laser source is sent to a phase modulator. Assume small signal modulation, at the output of the phase modulator, a DSB+C signal is generated. Note that it is different from intensity modulation using a Mach-Zehnder modulator to generate a DSB+C signal with the two sidebands being in phase, the two first sidebands of a phase modulated signal are out of phase. Thus, the detection of a phase-modulated DSB+C signal at a photodetector will not generate a microwave signal except a DC since the beating between the optical carrier and the lower sideband will cancel completely the beating between the optical carrier and the upper sideband. However, if one of the sidebands is removed by an optical notch filter in transmission or using a dual passband filter in reflection [76], such as a fiber Bragg grating or two cascaded fiber Bragg gratings, then the phase-modulated signal is converted to an intensity-modulated SSB+C signal and the detection of the signal at a photodetector will generate a microwave signal.

Figure 17 shows the schematic of a coherent microwave photonic filter, in which an optical notch filter, such as a fiber Bragg grating in transmission, is used to filter out one sideband of a phase-modulated signal, thus achieving phase-modulation to intensity-modulation conversion. As can be seen, the entire
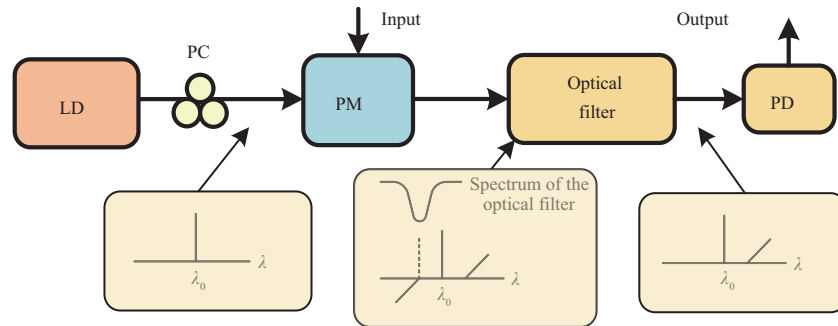
Figure 17 (Color online) Schematic of a coherent microwave photonic filter, in which an optical notch filter is used to filter out one sideband of a phase-modulated signal, thus achieving phase-modulation to intensity-modulation conversion.

operation is equivalent to a microwave filter with the bandwidth determined by the bandwidth of the notch of the optical notch filter and the center frequency is determined by the wavelength difference between the optical carrier and the center wavelength of the notch. Thus, by simply tuning the center frequency of the notch filter or the wavelength of the optical carrier, the center frequency of the microwave bandpass filter can be tuned. When tuning, the spectral shape is maintained unchanged. This is an advantage as compared with an incoherent microwave photonic filter, where the spectral shape is changing when the filter is tuned, or complex coefficients must be used to avoid such a spectral shape change.

Instead of using an optical filter in transmission, one may use two cascaded optical filters such as two fiber Bragg gratings in reflection, by using one fiber Bragg grating to select the optical carrier and the other fiber Bragg grating to select one sideband, and a phase-modulated signal is converted to a single-sideband intensity-modulated signal [76]. A microwave photonic filter with the spectral shape identical to the notch of the second fiber Bragg grating is generated. The major limitation of the technique in [76] is the wide passband since two uniform fiber Bragg gratings were employed. The passband of the microwave photonic filter was determined by the bandwidth of one of the two fiber Bragg gratings to select the sideband. By using a high Q-factor ring resonator [77], the passband can be smaller, but still too large for most applications.

Due to the ultra-narrow bandwidth of the stimulated Brillouin scattering (SBS) gain or loss spectrum, a microwave photonic filter with a narrow passband can be implemented based on phase modulation and phase-modulation to intensity-modulation conversion in an SBS gain or loss spectrum. Figure 18 shows a narrowband microwave photonic filter based on SBS [78]. A light wave from a laser source at ω_0 is split into two paths. At the upper path, the light is modulated by a local oscillator (LO) signal at a dual-parallel MZM (DP-MZM) to generate a single-sideband with suppressed carrier (SSB-SC) signal. Assume that the frequency of the local oscillator signal is ω_{LO}, the generated lower sideband is at $\omega_0 - \omega_{\mathrm{LO}}$. The SSB-SC signal is sent to an erbium-doped fiber amplifier to increase its power and then launched into a long single-mode fiber to stimulate the SBS effect. The SBS gain and loss are located at $\omega_O - \omega_{\mathrm{LO}} - \omega_B$ and $\omega_O - \omega_{\mathrm{LO}} + \omega_B$, respectively. If one sideband of a phase-modulated signal is amplified by the SBS gain, then the phase-modulated signal is converted to an intensity-modulated signal, and the detection of the intensity-modulated signal at a photodetector will generate a microwave signal at $\omega_{\mathrm{LO}} - \omega_B$, as shown in Figure 18. The entire operation of the system is equivalent to a microwave bandpass filter with the passband determined by the SBS gain spectrum. The advantage of this approach is that the filter can be continuously tunable by tuning the LO frequency and the passband is ultra-narrow. However, compared with the use of a fiber Bragg grating or a ring resonator, the system is very complicated, especially a high power erbium-doped fiber amplifier and a long single-mode fiber are needed.

To have an ultra-narrow passband while maintaining a simple system, a solution is to use an optical filter with an ultra-narrow passband. Figure 19 shows the implementation of a coherent microwave photonic filter using a phase-shifted fiber Bragg grating (PS-FBG) [79]. A phase-shifted fiber Bragg grating is a special fiber Bragg grating with a phase shift introduced to the fiber Bragg grating during the inscription process [79]. It is known for a uniform fiber Bragg grating, if a phase shift is introduced to the fiber Bragg grating, an ultra-narrow notch with a phase jump in the notch would be generated in the reflection band [80]. If a phase-modulated optical signal is injected into the phase-shifted fiber Bragg grating that is employed to modify the magnitude and the phase of one sideband, phase-modulation to intensity-modulation conversion would be achieved, which would lead to the implementation of an
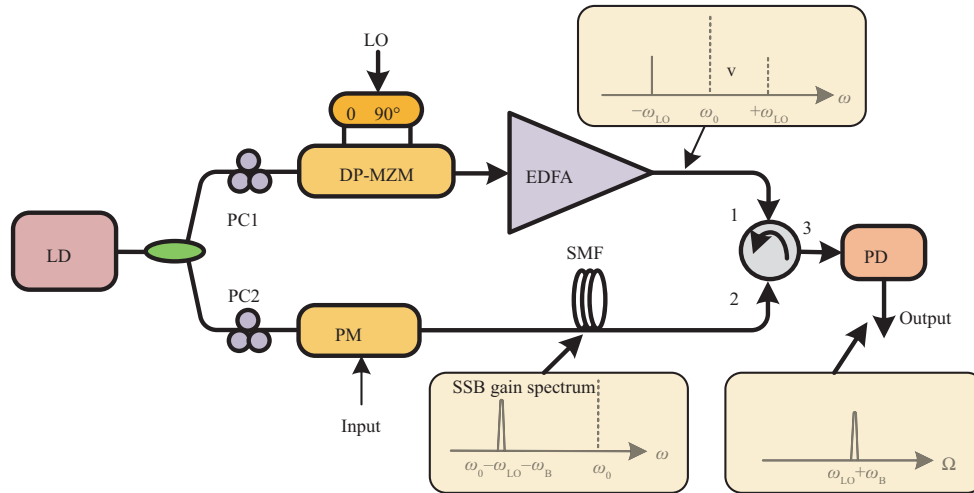
Figure 18 (Color online) A coherent microwave photonic filter implemented based on phase modulation and phase-modulation to intensity-modulation using the SBS gain.
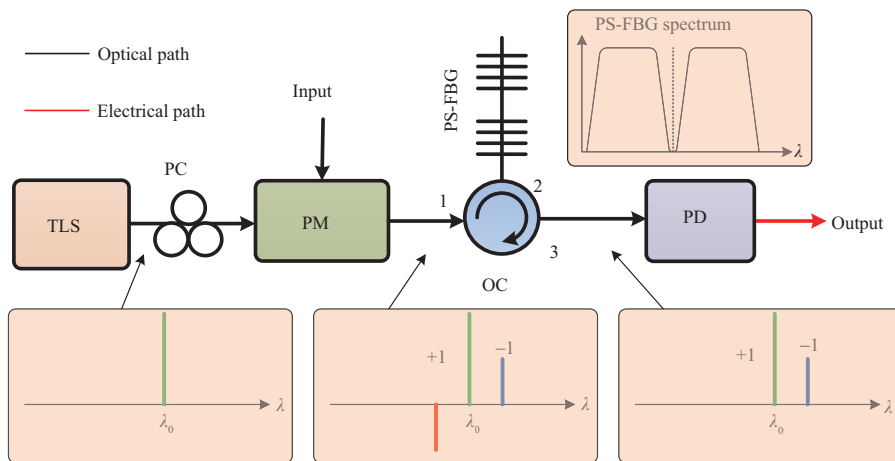

Figure 19 (Color online) A coherent microwave photonic filter implemented based on phase modulation and phase-modulation to intensity-modulation conversion using a PS-FBG.

ultra-narrow passband.

The same concept to implement a coherent microwave photonic filter based on phase-modulation to intensity-modulation conversion to translate the spectral response of an optical filter to that of a microwave photonic filter can be used to implement a microwave photonic filter with a flat top [81]. Instead of using the SBS or a phase-shifted fiber Bragg grating, a specially designed superstructured fiber Bragg grating (SFBG) was used. A superstructured fiber Bragg grating is a special fiber Bragg grating that is spatially modulated by a periodic sampling function along the grating. Due to the spatial sampling, the spectral response has multiple channels. If one period of the sampling function is intentionally increased by a half period, a π phase shift is introduced equivalently to the grating, leading to a narrow notch. The technique is called the equivalent phase shift (EPS) technique [82]. The advantage of introducing a phase shift through the EPS technique is that the sampling period is in the order of tens micrometers, which is 2–3 orders larger than the period of a uniform fiber Bragg grating, making the grating inscription system have better accuracy [82]. To have a flat bottom in the notch, the superstructured fiber Bragg grating was designed to have two closely spaced notches which were achieved by introducing two equivalent phase shifts to the structure. Each phase shift would produce a Lorentz-shaped notch and the combination of the two closely spaced Lorentz-shaped notches would lead to a notch with a flat bottom. When the superstructured fiber Bragg grating with a flat-bottom notch is incorporated to perform phase-modulation to intensity-modulation conversion, a passband with a flat top was achieved. The reflection bandwidth and notch width of the superstructured fiber Bragg grating, which determine the frequency tunable range and bandwidth of the passband, can be controlled
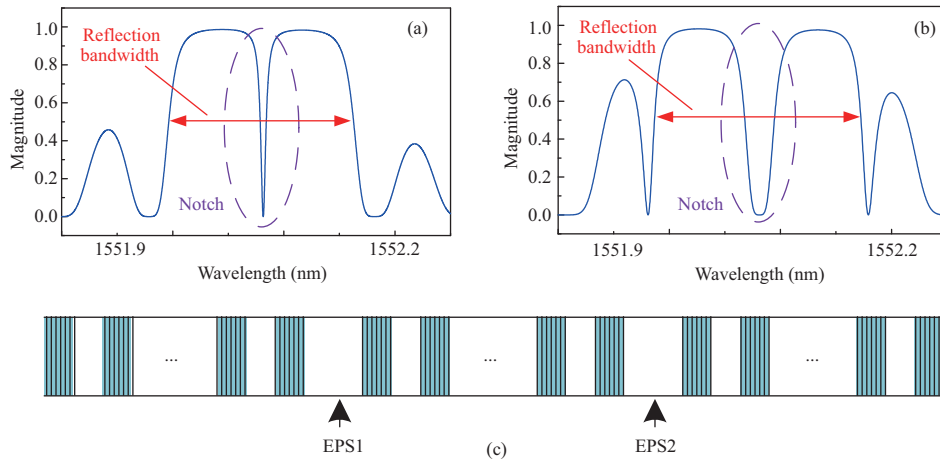
Figure 20 (Color online) (a) Simulated reflection spectrum of a phase-shifted fiber Bragg grating with a single phase shift; (b) simulated reflection spectrum of a superstructured fiber Bragg grating with two phase shifts; (c) structure of a superstructured fiber Bragg grating [81].
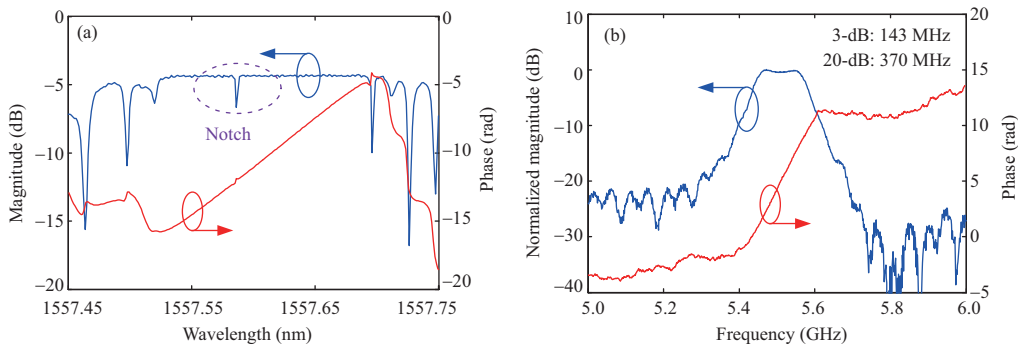

Figure 21 (Color online) (a) Measured reflection spectrum and phase response of a fabricated superstructured fiber Bragg grating; (b) frequency response and phase response of the microwave photonic filter using a superstructured fiber Bragg grating [81].

by controlling the length and maximum index modulation (MIM) of the superstructured fiber Bragg grating. Figure 20(a) shows a simulated reflection spectrum of a PS-FBG with a single-phase shift and Figure 20(b) shows a simulated reflection spectrum of an SFBG with two phase shifts. Figure 20(c) shows the structure of an SFBG in which two EPSs are incorporated.

Figure 21(a) shows the magnitude and phase response in reflection of a superstructured fiber Bragg grating with a length of 32.4 mm. Due to the limited resolution of the optical vector analyzer, the notch depth and shape cannot be precisely shown. Figure 21(b) shows the frequency response of the microwave photonic filter. As can be seen, it has a narrow passband with a flat top. The flatness of the passband is estimated to be within ±0.25 dB. The phase response of the microwave photonic filter is also shown in Figure 21(b). As can be seen, the phase response is linear within the passband. The 3-dB bandwidth was estimated to be 143 MHz. The 20-dB bandwidth was 370 MHz. The shape factor, which is defined as the ratio between the 20-dB and 3-dB bandwidths, was calculated to be 2.6, which is much smaller than those reported in [79]. A smaller shape factor represents a better selectivity. By tuning the wavelength of the optical carrier, the central frequency of the passband can be tuned. The magnitude response and bandwidth of the passband remained unchanged during the tuning, a feature that is important for applications where the shape of the passband and bandwidth are required to be constant.

For certain applications, microwave filters with dual or multiple passbands are needed due to the increasing demand for multiband/multifunctional microwave systems that support various modern services. The same concept can also be used to implement a microwave photonic filter with two or multiple passbands [83]. For a dual- or multi-band microwave photonic filter, the key component is the optical filter which should have dual or multiple passbands. This can be achieved again using an equivalent phase-shifted fiber Bragg grating (EPS-FBG), which could be fabricated by using the equivalent phase shift technique [84]. A phase-shifted fiber Bragg grating has multiple channels due to the spatial sampling of
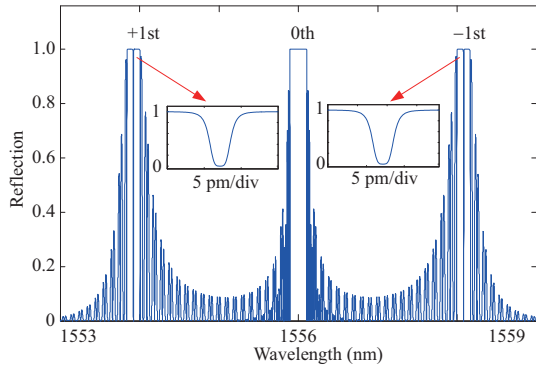
Figure 22 (Color online) Simulated reflection spectrum of an equivalent phase-shifted FBG with two phase shifts [83].
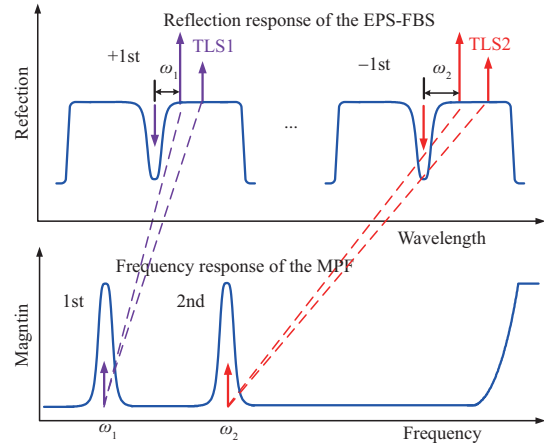

Figure 23 (Color online) Illustration of the generation of the two passbands using an equivalent phase-shifted FBG based on phase-modulation to intensity-modulation conversion [83].
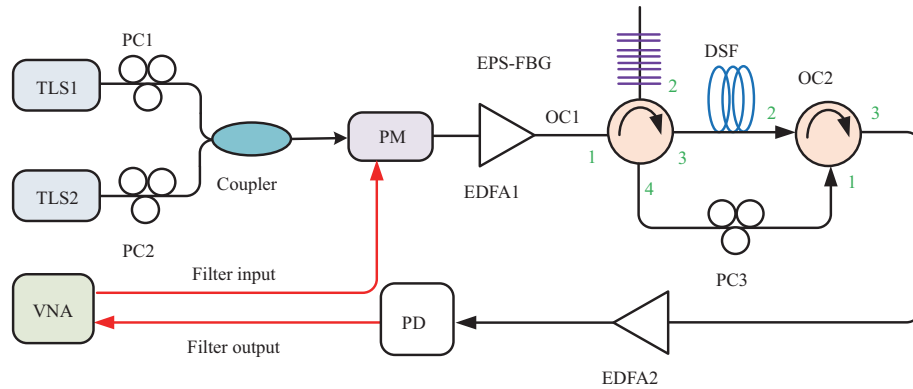

Figure 24 (Color online) Schematic of a dual-passband microwave photonic filter. TLS: tunable laser source; PC: polarization controller; PM: phase modulator; EDFA: erbium-doped fiber amplifier; EPS-FBG: equivalent phase-shifted fiber Bragg grating; OC: optical circulator; DSF: dispersion-shifted fiber; PD: photodetector; VNA: vector network analyzer [83].

the grating structure. Equivalent phase shifts introduced to the ±1st channels are realized by changing the sampling function. Therefore, the fabrication of a phase-shifted fiber Bragg grating is significantly simplified, since the control of the spatial sampling is in a micrometer scale, while the control of the phase shift in the fabrication of a true phase-shifted fiber Bragg grating is in a nanometer scale. In the design, two π phase shifts are introduced to both of the ±1st channels to produce an ultra-narrow and flat-bottom notch in each channel. Figure 22 shows a simulated reflection spectrum of an equivalent phase-shifted fiber Bragg grating with two π phase shifts. As can be seen, the notches are flat due to the use of two phase shifts. A bandpass filter is achieved due to the phase-modulation to intensity-modulation conversion by filtering out one sideband of a phase-modulated signal. In a dual-band microwave photonic filter, the phase-modulation to intensity-modulation conversion is performed at both the ±1st channels; thus two independently tunable passbands are generated, as shown in Figure 23. Because two π phase shifts are introduced to achieve flat-bottom notches, the passbands have small shape factors. Here, the shape factor is again defined as the ratio between the 20-dB and 3-dB bandwidths.

To produce two independent passbands, two optical carriers from two tunable laser sources (TLS1 and TLS2) are tuned to locate at the ±1st channels of the equivalent phase-shifted fiber Bragg grating, as shown in Figure 24. When one sideband of a phase-modulated signal is suppressed by the notch in the +1st channel, a passband with a central frequency that is the frequency difference between the optical carrier and the notch in the +1st channel, will be produced due to the phase-modulation to intensity-modulation conversion. Similarly, when one sideband of a phase-modulated signal is suppressed by the notch in the −1st channel, a passband with a central frequency that is the frequency difference between the optical carrier and the notch in the −1st channel, will also be produced. Therefore, there will be
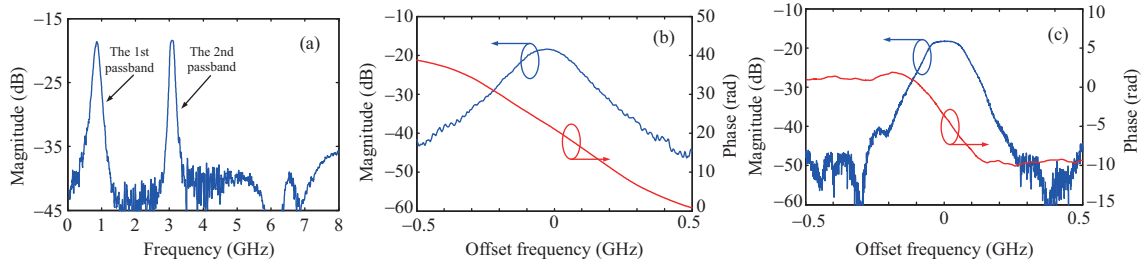
Figure 25 (Color online) (a) Frequency response of the dual-passband microwave photonic filter; magnitude and phase responses of (b) the 1st passband and (c) the 2nd passband [83].

two passbands at two different central frequencies. Again, the central frequencies of the passbands can be tuned by shifting the wavelengths of TLS1 and TLS2 independently. Figure 25 shows the spectral response of the dual passband filter. The bandwidth and shape factor of the 1st passband were estimated to be 167.3 MHz and 3.8, and those of the 2nd passband were 143.4 MHz and 3.3. The 1st and 2nd passband have frequency tunable ranges of 5.4 and 7.4 GHz, respectively. The central frequencies of both passbands can be continuously tuned. Again, the shape of the spectral response of the two passbands was maintained unchanged during the frequency tuning. The variations of the magnitude over the entire frequency tunable ranges were maintained within ±0.5 dB.

The SFDR and NF of a microwave photonic filter are two important parameters that define the linearity and noise performance of the filter and should also be evaluated. A few techniques have been proposed to improve the spurious free dynamic range and the noise figure of a microwave photonic filter [83–87]. One simple solution to increase the spurious free dynamic range and reduce the noise figure is to partially suppress the optical carriers while maintaining the powers at the input of the photodetector unchanged. This operation is equivalent to increasing the filter gain without increasing the noise floor (considering the dominant noise is the shot noise which is generated at the photodetector and is proportional to the optical power at the input of the photodetector). This can be done, for example, using an SBS-assisted filter, such as the one reported in [85] where the SBS-assisted filter was implemented using a dispersion-shifted fiber (DSF). When the light waves pass through the DSF, and the powers of the optical carriers are above the SBS threshold, Stokes waves are generated, which are traveling along the DSF in an opposite direction of the optical carriers. Note that, under small-signal modulation conditions, the powers of the sidebands are below the SBS threshold; thus SBS occurs only at the optical carriers and the sidebands are not affected. As the Stokes waves circulate in the loop, the optical carriers are suppressed. If the optical power at the input of the PD is maintained fixed, the suppression of the optical carriers will increase the gain of the system. The spurious free dynamic range is increased. Since the powers of the optical carriers are reduced, the short noise at the PD is reduced, which makes the noise figures reduced. In [85], the spurious free dynamic ranges were improved by about 7 dB, and the noise figures were decreased by 10 dB.

In summary, a microwave photonic filter can be implemented in the optical domain to take advantage of the high frequency and wide bandwidth offered by photonics. Compared with an electronic microwave filter, a microwave photonic filter can operate at a much higher frequency and can be widely frequency tunable. These are the two key features that make microwave filters implemented in the optical domain attractive. Between incoherent and coherent microwave photonic filters, a coherent microwave photonic filter has a simpler structure, since a single light source is needed, which provides a high potential for photonic integration. The key challenge in implementing an integrated coherent microwave photonic filter is that the optical filter, which is used to translate its spectral response to the microwave domain, should have a high Q factor to ensure an ultra-narrow bandwidth. The low loss of Si_3N_4 may make the implementation possible, but heterogeneous integration may be needed since no active devices can be implemented using Si_3N_4.

4.1 Microwave arbitrary waveform generation

Microwave arbitrary waveforms are widely used in radar, communications, microwave imaging, and modern instrumentation systems. Microwave arbitrary waveforms can be generated electronically based on analog or digital electronics. Due to the limited bandwidth or sampling rate, microwave arbitrary waveforms generated based on analog or digital electronics have low frequency and small bandwidth. For
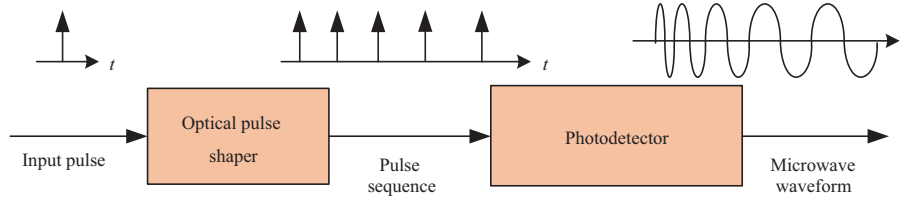
Figure 26 (Color online) Direct space-to-time (DST) mapping for microwave arbitrary waveform generation.

many applications, however, high frequency and large bandwidth microwave waveforms are needed. One solution is to perform microwave arbitrary waveform generation using photonics, to take advantage of the high speed and broad bandwidth offered by modern photonics [88]. A few techniques have been proposed to generate microwave arbitrary waveforms, including (1) direct space-to-time pulse shaping [89–96], (2) spectral-shaping and wavelength-to-time mapping [97–102] and (3) temporal pulse shaping [103–106]. These techniques can be implemented using free space optics or fiber optics. Free-space optics-based microwave arbitrary waveform generators have relatively large sizes and higher losses. Fiber optics can make microwave arbitrary waveform generators smaller and less lossy, and have a high potential for photonic integration.

4.2 Direct space-to-time mapping

Microwave arbitrary waveform generation can be realized based on direct space-to-time (DST) mapping [89–96], in which an optical input pulse is converted to a pulse burst in the optical domain. After photodetection to a high-speed photoreceptor, a microwave waveform is generated. The key to this approach is to control the time delays of the pulses in the pulse burst. Figure 26 shows a direct space-to-time mapping system in which an ultrashort optical pulse from a mode-locked laser source is sent to an optical pulse shaper to generate a pulse burst. The pulse sequence is then applied to a PD. Due to the bandwidth-limited nature of the photodetector, the high-frequency components are eliminated, and a smooth microwave waveform is generated. The theory behind the generation of a microwave arbitrary waveform using a direct space-to-time mapping system is that the microwave waveform to be generated can be obtained by filtering the pulse burst using a band-limited filter. If the temporal spacing is increasing linearly, then a chirped microwave waveform is generated. A chirped microwave waveform has a large time bandwidth product (TBWP), which is widely used in radar systems to increase the detection distance while maintaining a high range resolution through pulse compression (or matched filtering).

The key device in a direct space-to-time mapping system is the optical pulse shaper. It could be implemented in free space, but the size is large. A simpler but more effective approach is to use a PIC, such as an integrated arrayed waveguide grating. An ultra-short pulse is applied to the input of an arrayed waveguide grating, at the output of the arrayed waveguide grating, a pulse burst with the time spacing controlled by switching on and off some of the waveguide channels is generated. The limitation of the approach is that an arrayed waveguide grating developed for optical communications has a small number of channels, making the generated microwave arbitrary waveforms have a small bandwidth.

4.3 Spectral-shaping and wavelength-to-time mapping

Microwave arbitrary waveforms can also be generated based on spectral-shaping and wavelength-to-time mapping [97–102]. Figure 27 shows a microwave arbitrary waveform generation system based on spectral-shaping and wavelength-to-time mapping. As can be seen, the system consists of an ultra-short pulse source, a spectral shaper, a dispersive element, and a photodetector. The spectral shaper is used to modify the spectrum from the pulsed laser source, which can be a mode-locked laser source. The shaped spectrum is then applied to a dispersive element where wavelength-to-time mapping is performed. The dispersive element can be a length of dispersive fiber or a linearly chirped fiber Bragg grating. A microwave waveform is generated in the electrical domain at the output of a high-speed photodetector. If the dispersive element is a length of fiber with a value of the dispersion of $\ddot{\Phi}$, the impulse response is given by $h(t) = \exp(j\frac{t^2}{2\ddot{\Phi}})$. For an input pulse $g(t)$ with a temporal width of Δt_0, the signal at the output
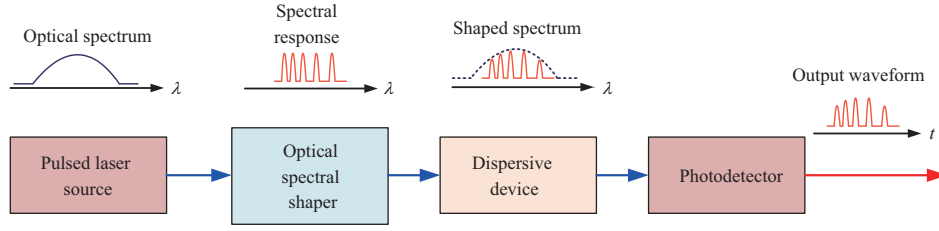
Figure 27 (Color online) Microwave arbitrary waveform generation based on spectral-shaping and wavelength-to-time mapping. By using a spectral shaper with a linearly increasing free spectral range, a linearly chirped microwave waveform can be generated after linear wavelength-to-time mapping.

of the dispersive element is calculated by

$$
\begin{aligned}
y(t) = g(t) \times h(t) &= g(t) \times \exp\left(j\frac{t^2}{2\ddot{\Phi}}\right) = \int_{-\infty}^{\infty} g(\tau) \times \exp\left[j\frac{(t-\tau)^2}{2\ddot{\Phi}}\right] d\tau \\
&= \exp\left(j\frac{t^2}{2\ddot{\Phi}}\right) \times \int_{-\infty}^{\infty} g(\tau) \times \exp\left(j\frac{\tau^2}{2\ddot{\Phi}}\right) \times \exp\left[-j\left(\frac{t}{\ddot{\Phi}}\right)\tau\right] d\tau \\
&\approx \exp\left(j\frac{t^2}{2\ddot{\Phi}}\right) \times \int_{-\infty}^{\infty} g(\tau) \times \exp\left[-j\left(\frac{t}{\ddot{\Phi}}\right)\tau\right] d\tau \\
&= \exp\left(j\frac{t^2}{2\ddot{\Phi}}\right) \times \left. G(\omega)\right|_{\omega=\frac{t}{\ddot{\Phi}}},
\end{aligned}
\tag{46}
$$

where $G(\omega)$ is the Fourier transform of $g(t)$. As can be seen the envelope of the output signal is proportional to the Fourier transform of the envelope of the input signal. Note that Eq. (46) is obtained if the temporal duration of the input ultrashort pulse Δt_0 and the dispersion $\ddot{\Phi}$ of the dispersive element satisfy the condition, given by

$$
\left|\frac{\Delta t_0^2}{2\ddot{\Phi}}\right| \ll 1,
\tag{47}
$$

which means the phase term $\frac{\tau^2}{2\ddot{\Phi}}$ in (46) satisfies $\frac{\tau^2}{2\ddot{\Phi}} \leqslant \frac{\Delta t_0^2}{2\ddot{\Phi}} \ll 1$, thus we have $\exp(j\frac{\tau^2}{2\ddot{\Phi}}) \approx 1$.

If the input to the dispersive device is a rectangular pulse, then the output temporal waveform should be a sinc function. As can be seen, the key device in the microwave arbitrary waveform generator is the spectral shaper, which should be designed to have a magnitude response that can make the shaped spectrum have the same shape as the microwave waveform to be generated. Again, the spectral shaper can be implemented using a spatial light modulator that can be updated in real time. A fiber-optics based spectral shaper can also be implemented. For example, we can use a special fiber Bragg grating with its spectral response designed to have a shape identical to that of the microwave arbitrary waveform. The key limitation of using a fiber Bragg grating is that the spectral response is fixed or has limited updatability. Thus, the generated waveform is fixed or can be slightly tuned with limited tunability.

4.4 Temporal pulse shaping

Microwave arbitrary waveforms can also be generated based on temporal pulse shaping (TPS) [103–106]. A typical temporal pulse shaping system consists of an ultra-short pulse source, a pair of complementary dispersive elements, and an optical modulator. The optical modulator can be an MZM or a phase modulator. Figure 28 shows the schematic of a temporal pulse shaping system, in which the modulator is a Mach-Zehnder modulator.

Again, if $|\Delta t_0^2/\ddot{\Phi}| \ll 1$, where Δt_0 is the temporal width of the input ultra-short short pulse, the electrical field of the short pulse $g(t)$ after transmitting through the first dispersive element with a value of the dispersion of $-\ddot{\Phi}$ can be expressed as

$$
\begin{aligned}
p(t) = g(t) \times \exp\left(j\frac{t^2}{2\ddot{\Phi}}\right) &= \int_{-\infty}^{\infty} g(\tau) \times \exp\left[j\frac{(t-\tau)^2}{2\ddot{\Phi}}\right] d\tau \\
&\approx \exp\left(j\frac{t^2}{2\ddot{\Phi}}\right) \int_{-\infty}^{\infty} g(\tau) \times \exp\left[j\left(-\frac{t}{\ddot{\Phi}}\right)\tau\right] d\tau
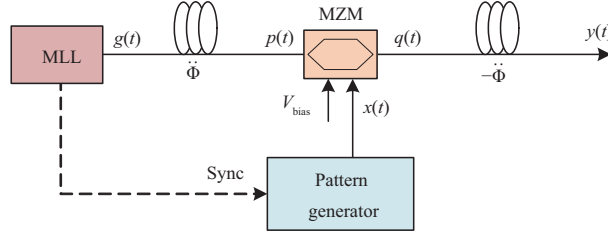\end{aligned}
$$

Figure 28 (Color online) A TPS system for arbitrary waveform generation. An ultra-short pulse is generated by a mode locked laser (MLL) [104].

$$= \exp\left(j\frac{t^2}{2\ddot{\Phi}}\right) G(\omega)|_{\omega=\frac{t}{\ddot{\Phi}}}, \tag{48}$$

where $G(\omega)$ is the Fourier transform of $g(t)$. The signal at the output of the Mach-Zehnder modulator is given by

$$q(t) = p(t) \times x(t) = \exp\left(j\frac{t^2}{2\ddot{\Phi}}\right) \times G\left(\frac{t}{\ddot{\Phi}}\right) \times x(t), \tag{49}$$

where $x(t)$ is the input microwave signal to the MZM.

After passing through the second dispersive element with a value of chromatic dispersion $-\ddot{\Phi}$, we obtain the output signal, which is the convolution between $q(t)$ and the impulse response of the dispersive element $h(t) = \exp(-jt^2/2\ddot{\Phi})$,

$$\begin{aligned} y(t) &= q(t) \times h(t) = q(t) \times \exp\left(-j\frac{t^2}{2\ddot{\Phi}}\right) \\ &= \int_{-\infty}^{\infty} q(\tau) \times \exp\left[-j\frac{(t-\tau)^2}{2\ddot{\Phi}}\right] d\tau \\ &= \exp\left(-j\frac{t^2}{2\ddot{\Phi}}\right) \times F\left[G\left(\frac{t}{\ddot{\Phi}}\right) \times x(t)\right]\Big|_{\omega=-\frac{t}{\ddot{\Phi}}} \\ &= 2\pi \left|\ddot{\Phi}\right| \exp\left(-j\frac{t^2}{2\ddot{\Phi}}\right) \times \left[g(-t) \times X\left(-\frac{t}{\ddot{\Phi}}\right)\right], \end{aligned} \tag{50}$$

where F denotes the Fourier transform operation and $X(\omega)$ is the Fourier transform of $x(t)$.

As can be seen from (50) the output waveform is a convolution between the input optical pulse and the Fourier transform of the input modulation signal. If the input optical pulse is ultrashort, such as a unit impulse function, then the generated waveform is the Fourier transform of the modulation signal since the convolution of a function with a unit impulse is the function itself. One important feature of this approach is that, to generate a fast waveform with a narrow temporal width, a slow waveform with a wide temporal width is needed, making the implementation simplified. Note that the major difficulty in implementing such a system is that the input optical pulse must be precisely synchronized with the input modulation signal, to ensure the dispersed optical pulse is modulated by the input modulation signal.

In summary, microwave arbitrary waveforms can be generated in the optical domain. The key advantages include wide bandwidth and high reconfigurability. Among the three different techniques, the one based on spectral shaping and wavelength-to-time mapping can provide the best flexibility in which the spectral shaper can be implemented using a spatial light modulator with fast reconfigurability. The use of a photonic integrated circuit [99] as a spectral shaper can have both small size and fast reconfigurability, which is considered a potential solution for future fully integrated microwave arbitrary waveform generators.

5 True time delay beamforming

Microwave beamforming based on phased array antennas is playing an important role in modern radar and wireless communication systems to increase transmission and receiving performance. The beam steering in a conventional phased array antenna is realized by introducing phase shifts to a microwave
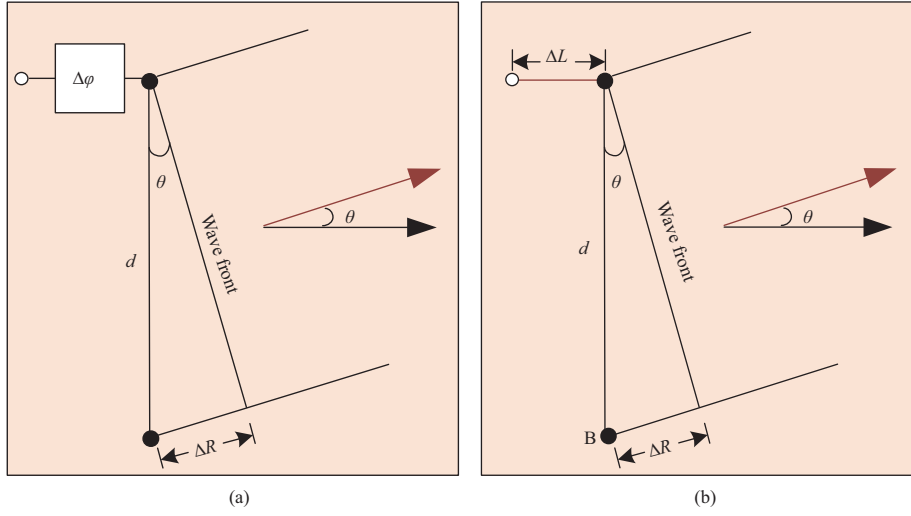
Figure 29 (Color online) Beam steering using (a) a phase shifter and (b) a delay line.

signal to be radiated to the free space using electronic phase shifters. The advantage of electronic phase shifters is that they can be implemented using electronic integrated circuits, making the beamforming network have a compact size with small power consumption and good stability. However, microwave beam steering based on electronic phase shifters suffers from the well-known beam squint problem, which would make the radiated microwave beam point in different directions. Thus, a phase array antenna based on phase shifters can only support narrowband operations. For many applications, such as wideband radar and broadband wireless communications, it is highly desirable that phase array antennas can support broadband operations. An effective solution is to replace the phase shifters with true-time delay (TTD) lines [1].

5.1 Beam squint phenomenon

The beam squint phenomenon is characterized by the position of the mainlobe being oriented at different angles for different microwave frequency components. In other words, the energy associated with different frequency components is oriented in different directions. To ensure that the beam is pointing to one direction, the microwave signal radiated to the free space via a phased array antenna must have a narrow bandwidth, which would limit the phased array antenna to operate for narrow-band only. The squint problem is caused due to the use of phase shifters. If true-time delay lines are employed, then the squint problem is solved [1].

The difference between the use of a phase shifter and a true-time delay line is illustrated in Figure 29. As can be seen from Figure 29(a), to steer the beam to a direction with angle of θ with respect to the broadside direction, the phase shifter should provide a phase shift given by

$$\Delta\phi = 2\pi\left(\frac{d\sin\theta}{\lambda}\right), \tag{51}$$

where λ is the wavelength of the microwave signal and d is the antenna array element spacing. The beam pointing direction is then given by

$$\theta = \sin^{-1}\left(\frac{\Delta\phi\lambda}{2\pi d}\right). \tag{52}$$

As can be seen by changing the phase shift, the beam pointing direction is changed. However, the beam pointing direction is also a function of the microwave wavelength. For a microwave signal with a finite bandwidth, the frequency components will be pointing in different directions, a phenomenon known as beam squint. Thus, to reduce the impact of beam squint, a beamforming network using electronic phase shifters should only operate for a narrowband signal. The problem can be solved if the phase shifters are replaced by optical true-time delay lines. As shown in Figure 29(b), the phase shifter is replaced by a delay line. The beam pointing direction is now given by

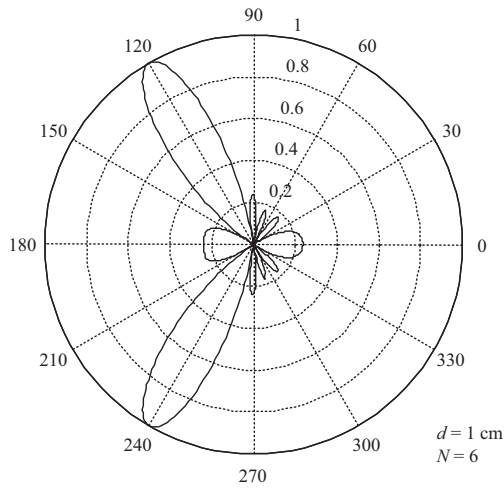$$\theta = \sin^{-1}\left(\frac{\Delta L}{d}\right), \tag{53}$$

Figure 30 Radiation pattern of a six-element array antenna with $d = \lambda_0/2$ at $f_0 = 15$ GHz.
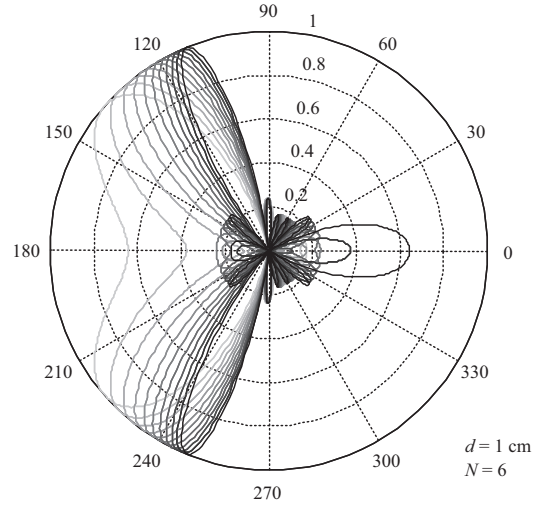
Figure 31 Beam squint effect for a phased array antenna based on electronic phase shifters operating in a frequency range from 10 to 20 GHz.

where ΔL is the physical length of the delay line. It can be seen that the beam pointing direction is independent of the microwave wavelength or frequency. Thus, microwave beamforming with a wide instantaneous bandwidth is achieved, and the system is squint free.

Figure 30 gives an example of an array antenna having six array elements with adjacent array elements separated by a distance of 1 cm ($d = \lambda_0/2$) operating at a central frequency of 15 GHz. To illustrate the beam squint effect, the bandwidth of a microwave signal to be radiated is assumed to be 10 GHz, covering a frequency range from 10 to 20 GHz. The far-field radiation pattern for the central frequency pointing at 120° is given in Figure 30.

Figure 31 illustrates the far-field radiation pattern for the microwave signal with a bandwidth of 10 GHz, from 10 to 20 GHz. As can be clearly seen, the beam pointing direction of the mainlobe varies with the feed signal frequency. This phenomenon would decrease significantly the performance of the beamforming system.

To eliminate the beam squint, a solution is to use true-time delays. This method is to introduce a time delay progression to the multi-channel feed signals instead of a phase progression. For a delay line, the time delay is constant for all frequencies and thus translates into a linearly variable phase shift with respect to frequency. Figure 32 shows the far-field radiation pattern by using the same phased array antenna operating at the same central frequency of 15 GHz. The behavior of the antenna is studied again for the microwave signal with a bandwidth covering a frequency range from 10 to 20 GHz. This time, true-time delay lines are used instead of electronic phase shifters. These elements introduce a time progression of 16.67 ps which corresponds to a phase of $\pi/2$ at the frequency of 15 GHz. As can be seen, the orientation of the mainlobe does not vary with the feed signal frequency. Thus, the beam squint problem is resolved.

5.2   Implementation of true-time delay beamforming

Conventional beamforming networks are implemented using electronic phase shifters. To eliminate beam squint, phase shifters have to be replaced by true-time delay lines. Electronic delay lines with tunable time delays are difficult to implement and the performance in terms of bandwidth and loss is very limited. For example, copper wires exhibit high loss at high frequencies resulting in a limited bandwidth. With the fast advancement in photonics technology, true-time delay lines implemented in the optical domain have been considered a strong candidate for broadband squint-free beamforming. In addition to the inherent broad bandwidth offered by modern photonics, the implementation of true-time delay lines in the optical domain can also benefit from the ultra-low loss of optical fibers, enabling not only effective true-time delay generation, but also low loss and broadband microwave signal transmission over fiber.

True-time delay beamforming based on photonics has been extensively researched in the past few years [107–125]. A beamforming network can be implemented using free space optics [107,108], but with
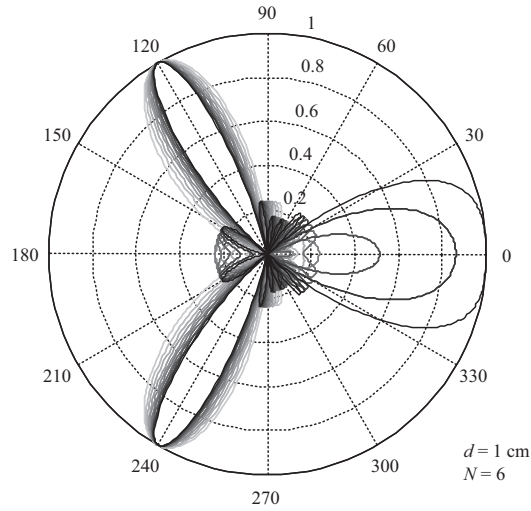
Figure 32 Far-field radiation pattern of a phased array antenna based on true-time delay lines operating in a frequency range from 10 to 20 GHz.
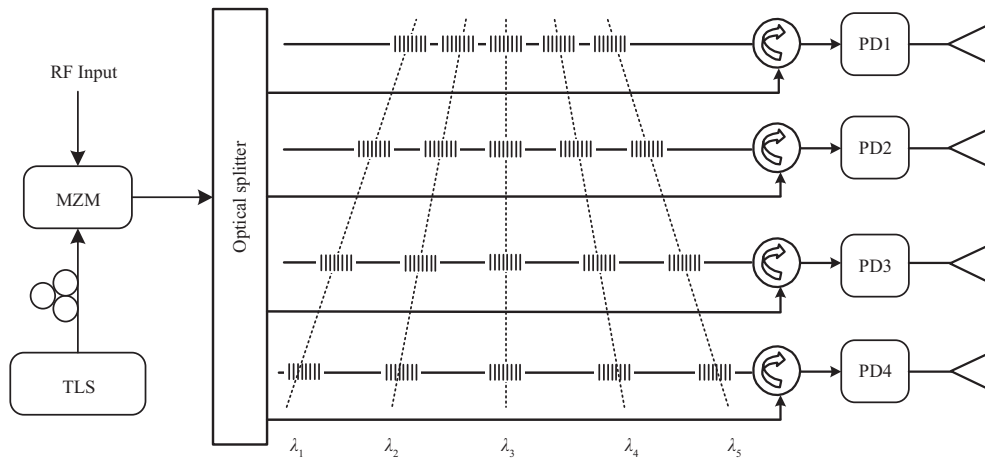

Figure 33 A photonic true-time delay beamforming system based on fiber Bragg grating based delay lines.

large size and high loss. A beamforming network can also be implemented based on fiber optics [109–125]. Since the loss of state-of-the-art fibers is very low, a fiber-optics-based beamforming network has better performance in terms of smaller size and lower loss. Figure 33 shows a fiber Bragg grating based true-time delay beamforming network. As can be seen, it consists of a tunable laser source, a modulator, four channels of fiber Bragg grating delay lines, and four photodetectors. By tuning the wavelength of the light from the tunable laser source, the four-channel signals will be reflected at different locations and the beam pointing direction can be steered. Note that the time delays are discretely tunable due to the use of fiber Bragg grating delay lines. If all the fiber Bragg gratings in the delay lines are replaced by chirped gratings, continuous beam steering would be realized.

In summary, the implementation of microwave beamforming based on photonic delay lines has a key advantage of squint free, which is highly needed to support beam steering with wide instantaneous bandwidth. A photonic true-time delay beamforming network can be implemented based either on free space optics, but the size is large and the weight is high, or fiber optics with smaller size and lower weight, but the stability is poor. Advanced packaging may be needed to reduce the sensitivity to environmental interferences, but the cost will be increased. With the advances in photonic integrated circuits, a microwave beamforming system on an integrated chip could be implemented with a much smaller size and lower weight, and is able to support broadband beamforming with a large number of channels.

6 Integrated microwave photonics

The microwave photonic subsystems and systems discussed in the previous sections are implemented based on discrete components. Despite its tremendous potential, and a considerable number of functionalities that have been demonstrated over the last 40 years, the widespread use and application of microwave photonics have been limited by the high cost, bulky, complex and power-consuming nature of the systems. A major challenge in microwave photonics implies a reduced cost, size, weight and power consumption (SWaP) of its devices, subsystems and systems. Integrated photonics has the potential to change the scaling laws of high-bandwidth systems through proper architectural choices that combine photonics with electronics to optimize the performance, power, footprint, and cost [126]. Drastic space and weight reductions are immediate gains from integration.

IMWP deals with the application of integrated photonics technologies to microwave photonics systems [127,128]. During the last few years, IMWP has become probably the most active area of current research and development in the discipline of microwave photonics [129], capitalizing upon the outstanding progress of integrated photonics in various material platforms such as InP, SOI, silicon nitride (Si_3N_4), and LOI. In this section, we will first outline the salient characteristics of available material platforms that can be employed for the implementation of IMWP chips. We will compare the features of the more mature material platforms and then describe the two salient approaches that are available for the implementation of IMWP chips from a functional point of view. On one hand, we review the recent progress in application-specific photonic integrated circuits (ASPICs), where a particular circuit configuration is designed to optimally perform a particular microwave photonics functionality. Examples of different functionalities recently reported will be presented, including tunable filtering, optoelectronic oscillation, instantaneous frequency measurement, and frequency up and down conversion. On another hand, recent progress will be reported on a radically different approach, programmable photonics, that enables the implementation of general purpose programmable microwave photonics signal processors that can be integrated on a chip and are capable of performing all the main functionalities by suitable software programming of its control signals. This approach is inspired by the flexibility of digital signal processors, where a common hardware is shared by multiple functionalities through a software-defined approach (or programmability), leading to significant cost reduction in the hardware fabrication. Further coverage of IMWP can be found in two existing monographic reviews [127,129].

6.1 Design, fabrication, and material platforms

IMWP design and fabrication processes must align with the state-of-the-art generic integration (GIM) and generic foundry (GFM) models [130] to leverage the already existing ecosystem. In the GIM, a small set of standardized basic building blocks (BBBs) are provided to control the basic properties of light and more complex circuits or compound building blocks (CBBs) are then built by connecting several BBBs. In the GFM, the foundry provides a shared open access to its generic integration process through multi project wafers, where different designs or ASPICs from different users are combined on the same wafer providing cost sharing and additional advantages, such as on-wafer testing. Since the GIM and GFM allow a broad range of functionalities to be synthesized from a small set of BBBs, they have been identified as the only path leading to mass production and subsequent cost reduction for PIC manufacturing, where figures in the order of $10 \, €/mm^2$ can already be reached at volumes of 1000 chips for InP technology [130]. Three material platforms: (1) InP, (2) SOI, and (3) Si_3N_4, have reached the required degree of maturity to be considered as viable options for the implementation of complex photonic integrated circuits, either monolithic or hybrid or heterogeneous. These operate mainly in the 1.3 and 1.55 μm wavelength regions. Recently, a new platform based on lithium niobate on insulator (LNOI) is starting to be considered a viable alternative for the implementation of IMWP circuits requiring high-performance modulators. We now describe the salient features of each of them.

Indium phosphide PIC technology. Indium phosphide is a III-V compound semiconductor material and the only technology capable of the monolithic integration of active (i.e., featuring optical amplification) and passive photonic components [131,132][1]. A variety of techniques, including butt-joint regrowth, selective area growth, offset and dual quantum well placing and quantum well intermixing, can be employed to integrate regions with different absorption/gain properties along a single waveguide. Waveguide types
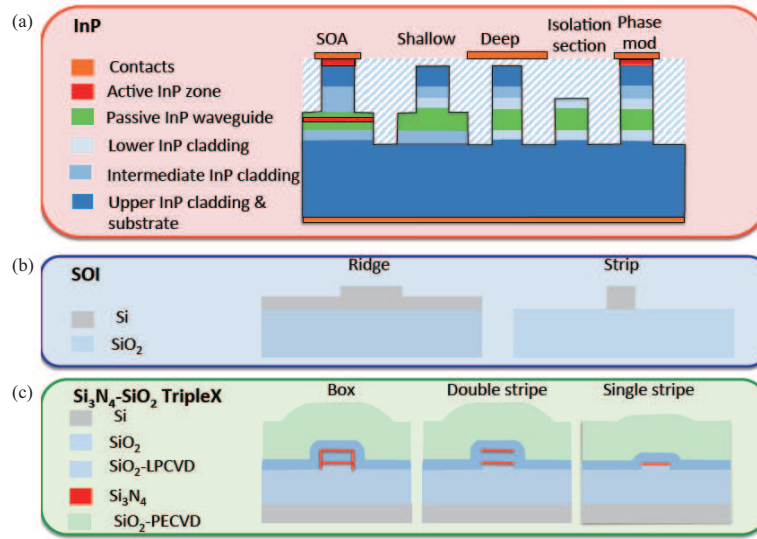
---

1) JePPIX Roadmap 2015. http://www.jeppix.eu.

Figure 34 (Color online) Waveguide structures for the InP (a), SOI (b), and Si_3N_4-SiO_2 (c) platforms.

include shallow (low loss and long bending radius) and deeply etched (higher losses and lower bending radius) designs (see Figure 34(a)).

Shallow waveguides have typical widths of 2 μm and this figure is approximately 1.5 μm for deeply etched designs. Typical losses are around 1.5 and 3 dB/cm for shallow and deeply etched waveguides, respectively, and this is usually quoted as one of the disadvantages of this technology. These losses can be reduced, however, to figures below 1 dB/cm by removing the p-type top layer in the non-active parts of the chip. Minimum bending radii are between 10 and 500 μm for deeply etched and shallow etched waveguides, respectively. Another quoted limitation of the InP platform is related to the difficulty of its integration with electronics into the same chip. However, highly promising work is underway towards the integration of full photonic functionality in a single InP membrane on Silicon that could be implemented both in a CMOS or an InP fab, merging InP photonics with silicon electronics.

InP provides the most complete list of available components for integration [131] including passives, optical filters, arrayed waveguide gratings, semiconductor optical amplifiers, saturable absorbers, optical sources (Fabry-Perot, distributed Bragg reflector, distributed feedback, and mode-locked lasers), detectors (pin single and balanced configurations), amplitude and phase modulators and polarization handling devices. Moreover, it has shown record performance in integrated component count on the same chip with figures exceeding 450 and now targeting values in the thousands range [132].

Silicon photonics PIC technology. Also known as SOI [133–136], silicon photonics is a semiconductor technology where components are etched/patterned/fabricated in a 180–220 nm silicon layer placed on top of a 1–3 μm insulator layer. Silicon passives are formed by initial few mask layers through partial and/or full silicon etching steps after which multiple ion implantations are conducted for "active" devices such as Ge photodetectors and silicon modulators. Coupling into and outside the chip can be performed via edge couplers (with typical losses of 1 dB/facet) or vertically, via silicon surface gratings (3.5–6 dB/coupler with 40–70 nm 3-dB bandwidth). The main advantage of the SOI technology resides in its potential compatibility with the well-developed CMOS fabrication processes and the infrastructure used in microelectronics and thus in the potential for monolithic integration of the electronic and photonic parts of the same chip. Refractive index contrast is over 100% (3.4 for silicon and 1.45 for SiO_2), leading to small footprint circuits.

Two main types of waveguides are available (see Figure 34(b)). Ridge or shallow (1–8 μm width), which exhibit relatively low losses down to 0.1–0.5 dB/cm, but are limited in bending radius to around 100 μm, and strip waveguides (500 nm width) that exhibit much higher losses (1–3 dB/cm) but support lower values for minimum bending radius (5–20 μm). Integration density on a chip is currently below 100 components [136], but the component count integration trend is exceeding the rate given by Moore's law indeed. Several basic photonic components are available in monolithic SOI, including passives, such as arrayed waveguide gratings and optical filters, Ge photodetectors, ring and traveling-wave electro-refractive modulators (up to 50 GHz). The main disadvantage of monolithic SOI technology is that it

does not support optical sources and other active components such as optical amplifiers. To overcome this limitation, III-V functionalities have to be integrated into the SOI platform by means of molecular [137], adhesive [138] wafer bonding and more recently by transfer printing [139]. This approach, known as hybrid silicon or hybrid integration technology has succeeded in incorporating amplifiers, saturable absorbers, optical sources (Fabry-Perot, distributed Bragg reflector, distributed feedback, and mode-locked lasers), optical amplifiers, electroabsorption (>70 GHz), and Mach-Zehnder (>25 GHz) modulators, photodetectors (>35 GHz) and polarization handling components into SOI chips. However, GFM and GIM have not yet been developed for hybrid integration technology.

Silicon nitride Si_3N_4-SiO_2 PIC technology. This waveguide technology is based on a combination of stoichiometric Si_3N_4 as waveguide layers, filled by and encapsulated with silica (SiO_2) as cladding layers grown on a silicon wafer [140, 141]. SiO_2 and Si_3N_4 layers are fabricated with CMOS-compatible industrial standard low-pressure chemical vapour deposition equipment that enables cost-effective volume production. A special technology known as TriPleX^{TM} [140], developed by a Dutch company, LioniX International, allows the fabrication of waveguides with minimized surface roughness allowing high refractive index contrast (20%–30%) and low scattering losses. The TriPleX^{TM} platform offers seven waveguide cross-sectional geometries [140], some of which are shown in Figure 34(c). Their salient characteristics at 1550 nm are low index contrast box-shaped (1 μm × 1 μm) that features reduced birefringence, $\leqslant$0.2 dB/cm losses and minimum bending radius (R_{min}) around 500 μm and mode field area (MFA) of 3.6 μm × 3.6 μm; high-index contrast featuring R_{min} of 150 μm and MFA of 1.4 μm × 1.4 μm; single-stripe (R_{min} of 2000 μm, <0.03 dB/cm losses and MFA of 4.7 μm × 2.9 μm); double-stripe (1 μm × 1 μm, R_{min} of 100 μm and MFA of 1.6 μm × 1.7 μm) obtained by removing the sidewalls of the box configuration, which leads to the significant reduction of the waveguide losses that are now in the <0.1 dB/cm range. In/out coupling is achieved by means of adiabatically tapered spot-size converters to low index contrast double-stripe cross-sections with <1 dB coupling loss. Several fundamental building blocks are available including the optical waveguide, tuning elements, and directional and multimode interference couplers. From these, more complex subsystems have been demonstrated. For the double-stripe geometry, a library of standard optical components with predictable characteristics is available. The main disadvantage of this technology is that no optical sources, detectors, amplifiers, and modulators are available. The integration of these components requires a hybrid approach with separately fabricated InP platform chips [141]. The recent development of InP device transfer printing techniques [139, 142] and InP membranes on Silicon [143] opens the path for the compact and versatile implementation of this required hybrid integration approach.

Lithium niobate on silicon technology. Lithium niobate ($LiNbO_3$ or LN) on insulator (LNOI) is a promising material platform for integrated photonics due to single crystal $LiNbO_3$ film's wide transparent window, high refractive index, and high second-order nonlinearity [144]. Compared with traditional material platforms described above, LNOI has several advantages, including strong electro-optic effect (largest r_{33} = 27 pm/V at 1500 nm), large refractive index (n_o = 2.21 and n_e = 2.14 at 1550 nm), wide transparency wavelength (from 400 nm to 5 μm), and stable physical and chemical characteristics, thus making it a competitive material for linear and nonlinear integrated photonics [145]. Similar to SOI, LNOI on insulator consists of a submicrometer LN film on a silica buried layer, which is on top of a substrate made from silicon or LN. To fabricate an LNOI device, a single-crystal sub-micrometer LN film is first obtained by ion slicing a bulk crystal and then is bonded to a low index substrate by using benzocyclobutene bonding [146] or crystal bonding [147]. This fabrication process has already matured and a typical LNOI wafer has an LN film thickness of hundreds of nanometers (typically 300–900 nm) and a diameter of 3 or 4 inches[2]. Nanostructuring techniques include wet etching, dry etching, chemical mechanical polishing (CMP), diamond dicing, femtosecond laser direct writing, and focused ion beam (FIB). All these techniques enable fabricating LN ridge waveguides. Although propagation loss of LN waveguide has a theoretical limitation down to 0.001 dB/cm [148, 149]. So far, even the best LN waveguide shows a loss higher than this limitation due to radiation loss caused by waveguide bending and scattering loss induced by surface roughness. Nevertheless, progress in improving losses has led to losses as low as 0.027 dB/cm while a standard figure is 0.32 dB/cm. Several devices have been reported in this technology, including modulators (featuring bandwidths up to 70 GHz) cavity ring and micro-disk resonators, and periodically poled waveguides and electrooptic comb sources.

---

2) Jinan Jingzheng Electronics Co., Ltd. https://www.nanoln.com.

Table 1 Excerpt of recent IMWP devices after [127, 150][a)]

Function	Material	FSR	CF	BW	R
Filter	InP	23.5 GHz or 47 GHz	28 GHz	1.9–5.4 GHz	32 dB
Filter	InP	–	10–40 GHz	3.9–7.1 GHz	40 dB
Filter	TriPleX	–	2–8 GHz	247–840 MHz	60 dB
Function	Material	Pulse rate	Pulse width	BW	FCC
AWG	SiN	595 GHz	300 fs	–	–
AWG	As2S3 Chalc.	–	–	4–15 GHz	Yes
AWG	InP	–	–	4–15 GHz	Yes
AWG	TriPleX	–	–	4–15 GHz	Yes
Function	Material	PS	PS BW		
TBPS	SOI	$0°–90°$	16–20 GHz	–	–
Function	Material	Delay	Delay BW		
TTTD	SOI	0–25.7 ps	8 GHz	–	–
TTTD	TriPleX	0–396 ps	1 GHz	–	–
TTTD	SOI	21–96 ps	–	–	–
Function	Material	Range	Error	Power	
IFM	InP	5–15 GHz	200 MHz	[−3, 7] dBm	–
IFM	TriPleX	0.5–4 GHz	93.6 MHz	–	–
Function	Material	Lock range	Loop BW		
OPLL	InP	[−9, 7.5] GHz	400 MHz	–	–
Function	Material	RF band	Inst. BW	# AE	
BFM	TriPleX	2–10 GHz	8 GHz	16	–

a) FSR: free spectral range; CF: center frequency; BW: bandwidth; *R*: rejection; FCC: US federal communications commission compliance; PS: phase shift; Inst.: instantaneous; AE: antenna element.

6.2 Application-specific photonic integrated circuits for microwave photonics

Microwave photonics with a variable degree of complexity arising from the combination of building blocks has been reported for a variety of functionalities during the last years. In particular, ASPICS has been demonstrated. For some of these functions, an excerpt of relevant studies is provided in the following subsections, and summarized in Table 1. For further details refer to [127–129, 150]. We now review some salient results.

Filters. As far as integrated coherent filtering is concerned, many of the preliminary approaches reported so far have been based mainly on single cavity ring resonators (RRs). A few, however, have also focused on more elaborated designs involving more than one cavity and programmable features. Representative results for single and multiple cavity filters or ring resonators can be found in [151–157]. For instance, Norberg et al. [154] reported the results for a unit cell, shown in Figure 35(b) that can be employed as a basic building block of more complex filters as displayed in Figure 35(a).

The unit cell integrated in InP-InGaAsP is a ring loaded Mach-Zehnder interferometer. By selectively biasing the SOAs and phase modulators placed in the arms of the unit cell, filters with a single pole, a single zero or a combination of both can be programmed as shown in Figure 35(c). The cell concatenation scheme shown in Figure 35(a) to form complex filters consists of the uncoupled cascade of a set of N unit cells, where each one can be programmed to independently act as an FIR, IIR or FIR+IIR cell. Synthesis algorithms developed in [158] can be therefore applied to implement discrete-time optical filtering with arbitrary complexity.

A hybrid version incorporating silicon waveguides has also been reported [156, 157] that combines III-V quantum well layers bonded with low loss passive silicon waveguides. Low loss waveguides allow for long loop delays while III-V quantum devices provide active tuning capability. The same group involved in [154] reported results of more complex designs involving two and up to three coupled ring cavities inside the Mach-Zehnder structure [155], which enables second- and third-order filters as shown in Figure 36. In particular, for this design the frequency tuning range spans around 100 GHz.

Multistage, coupled cavity filters, also known as CROWS (coupled resonant optical waveguides), have been reported in SOI technology. In [159, 160], 1–2 GHz-bandwidth filters with very high extinction ratios (∼50 dB) have been demonstrated. The silicon waveguides employed to construct these filters had propagation losses of ∼0.5 dB/cm and insertion losses (excluding fiber to waveguide coupling) in the range of 2–3.5 dB. Each ring was thermally controlled by means of metal heaters, placed on the top of the
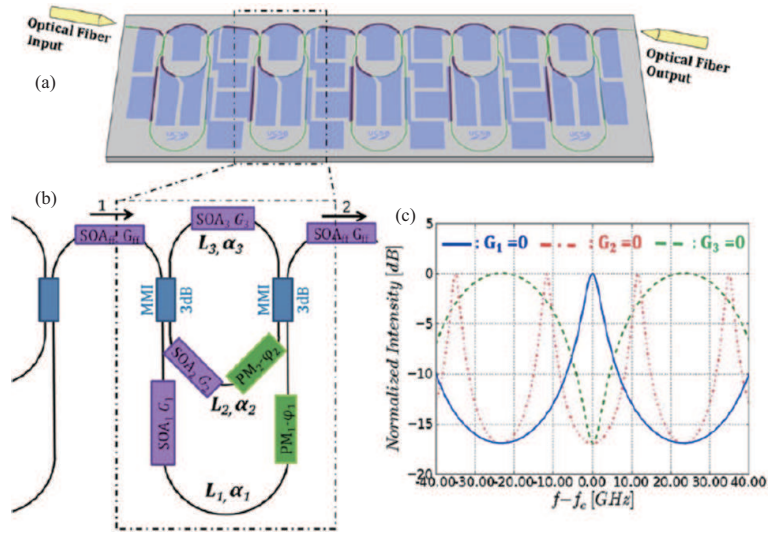
Figure 35 (Color online) Integrated InP-InGaAsP first-order MWP coherent filter providing one pole and one zero reported in [154]. (a) Cascade configuration of unit cells to implement high-order filters; (b) unit cell configuration; (c) examples of measured transfer functions for one pole and one zero configurations.
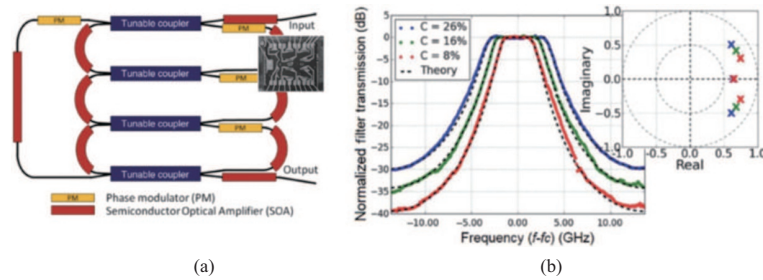

Figure 36 (Color online) (a) Layout of a multistage InP filter with tunable poles and zeros (after [155]); (b) detail of the resonance shapes for different reconfiguration parameter setups with their corresponding pole positions.
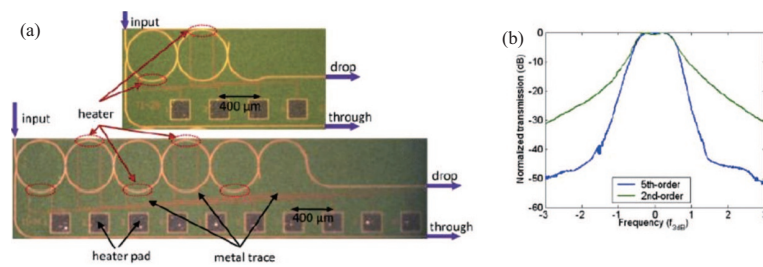

Figure 37 (Color online) (a) Optical images of fully fabricated 2nd-order and 5th-order CROW filters (after [159]); (b) measured (drop and through) transfer functions for the filters.

ring. With a power dissipation of ∼72 mW, the ring resonance could be tuned by one free spectral range, resulting in wavelength-tunable optical filters. Both the second-order and fifth-order ring resonators were demonstrated. Figure 37 shows the relevant results for this filter.

More recently filters with a higher degree of sophistication obtained by the cascade of several CROW stages have been reported for channel selection in dense wavelength division multiplexed systems. Figure 38 shows the results from Romero-García and co-workers [161]. The reported devices were based on three cascaded stages of CROWS loaded on a common bus waveguide. As shown in the layout of Figure 38(a) and the fabricated device in Figure 38(b), the stages differed in the number of resonators but were implemented with exactly identical unit cells, composed of a matched racetrack resonator layout and a uniform spacing between cells. The different number of resonators in each stage allowed a high rejection in the through port response enabled by the interleaved distribution of zeros. The exact replication of a unique cell avoided the passband ripple and high lobes in the stopband that typically arise in apodized
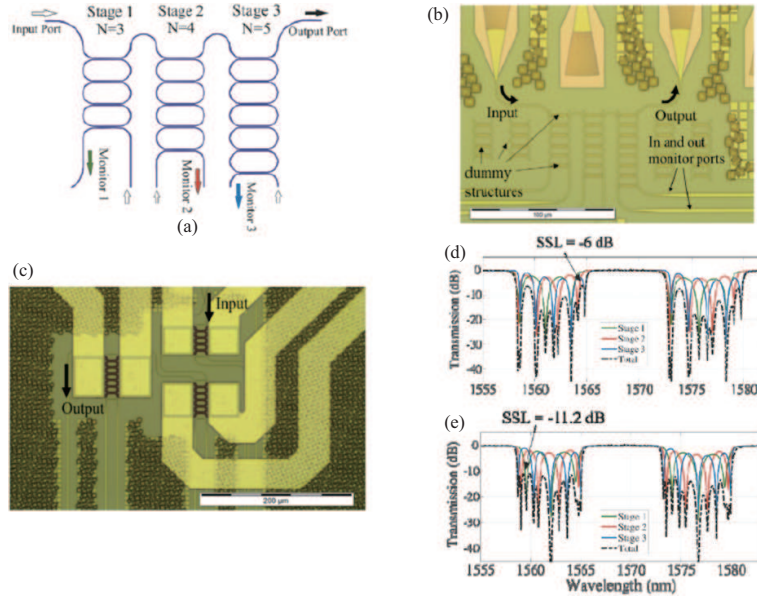
Figure 38 (Color online) Multiple stage CROW filter in SOI (after [161]). (a) Filter layout; (b) fabricated device in SOI; (c) a detail of the electrodes driving the phase shifters in each CROW stage; measurement results of the three individual stages of the filter and combined response (d) before and (e) after tuning with thermal phase shifters.
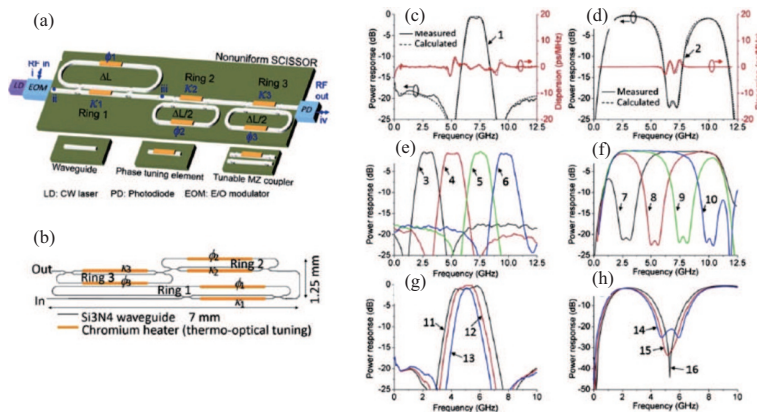

Figure 39 (Color online) (a) and (b) Layout of a Si_3N_4 reconfigurable SCISSOR (after [164]). (c)–(h) Different transfer functions and frequency tunings obtained by reconfiguration. (c) Band-pass and (d) band-stop filter response. (e) and (f) Tuning of filter center frequency. (g) and (h) Variations of filter response shape and bandwidth.

coupled resonator optical waveguide-based filters due to fabrication and coupling induced variations in the effective path length of each resonator. The filters could be reconfigured by means of thermal phase shifters incorporated in each CROW stage as shown in Figure 38(c). The fine tuning enabled the selection of WDM channels with an increased rejection ratio as shown in Figure 38(d) and (e).

Rasras and co-workers [162, 163] demonstrated bandpass and notch filters based on Mach-Zehnder interferometer (MZI) tunable couplers and RRs fabricated in silicon-buried channel waveguides with a width of 2 μm and a propagation loss of 0.25 dB/cm.

High-performance filters have also been demonstrated on other platforms. For instance, in the silicon nitride platform researchers from Monash University in Australia reported a complex side coupled integrated series of optical resonators (SCISSOR) filter composed of the serial cascade of three ring resonators of different FSRs [164–166], as illustrated in Figures 39(a) and (b), and their filter responses shown in Figures 39(c)–(h).

Here, a pair of rings with identical FSRs were employed for filter shape synthesis and a third ring with a smaller FSR was used to perform the function as a modulation translator [165, 166] that enables a separate manipulation of the optical carrier phase. A reconfigurable filter was demonstrated using such a processor where all the reconfiguration operations including filter frequency tuning, bandwidth
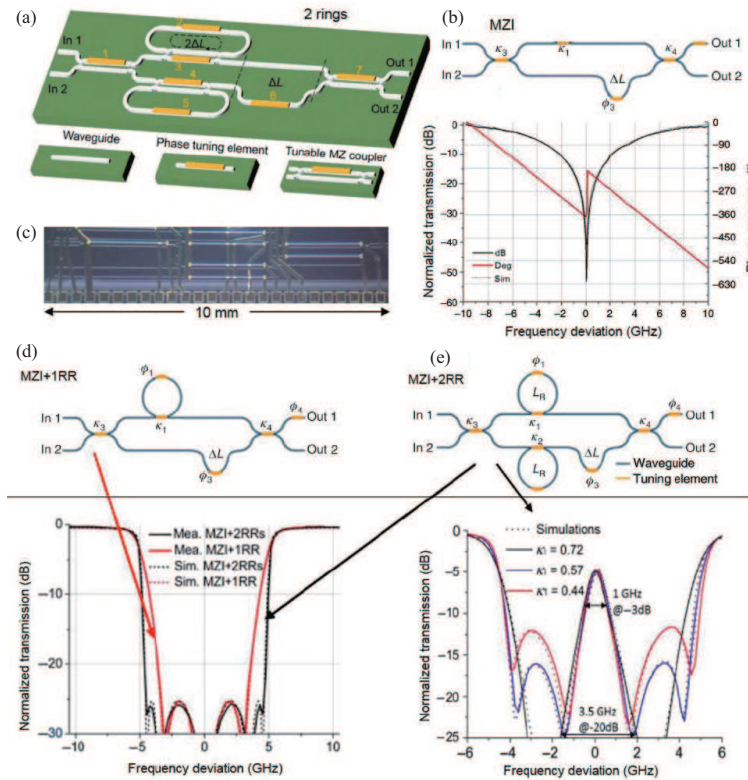
Figure 40 (Color online) (a) RAMZI filter layout based on (b) an asymmetric Mach-Zehnder interferometer. (c) Photograph of the fabricated device in Si_3N_4 (after [168]). (d) and (e) Different filter transfer functions obtained by parameter reconfiguration in one ring and two ring RAMZIs.

variation, and switching between bandpass and bandstop filter shapes were implemented as shown in Figures 39(c)–(h) using the tuning mechanism based on DC-voltage-driven resistor heaters.

Another example of a reconfigurable and versatile filter that combines both FIR and IIR sections is the ring assisted MZI (RAMZI) shown in Figure 40. It comprises an asymmetric MZI with each arm coupled with an RR. This filter can be subject to different parameter settings resulting in the possibility of implementing either an FIR, an IIR or an FIR + IIR response as demonstrated in [159]. A team of researchers from Lionix international, the University of Twente in the Netherlands and Monash University in Australia reported a tunable RAMZI circuit [167, 168] employing a total of seven tuning elements, including two tunable couplers at the input and output of the MZI, two tunable couplers of the two RRs, and three tunable phase shifters in the ring loops and MZI delay line, all implemented using resistor-based heaters. This RAMZI design enabled a variety of different implementations of optical filters as shown in Figure 40. The same team has reported a wide variety of reconfigurable filters for microwave photonics applications. A detailed description of most of these designs can be found in [169]. RAMZI filters have also been fabricated in SOI technology [170] and a monolithic version for radiofrequency filtering has been recently reported in InP [171].

To date, most filter implementations are incomplete in the sense that not all the required elements are included in the chip. The exception is a recently reported monolithic MWP filter implemented in InP technology [171]. The filter layout shown in Figure 41(a) integrates all the required elements into the same substrate, including a tunable distributed Bragg reflector laser (DBR), a dual-drive modulator, a tunable optical filter based on a RAMZI where poles and zeros can be selected by changing the coupling constant of a set of 3-dB MZI couplers via the thermo optic effect and a photodetector. The chip photograph shown in Figure 41(b) includes also other testing structures. The chip was fully packaged as shown in Figure 41(c) and its reconfigurable operation was tested in the laboratory where the transfer function of the RF-Photonic filter could be reconfigured by changing the bias current operating over the thermo optic phase shifters inserted in the arms of the 3-dB MZI tunable couplers as shown in Figure 41(d).

Optoelectronic oscillators. Recently several attempts have been reported towards the full integration of the photonic part of an OEO on a chip [172, 173]. In [172], a silicon photonic integrated OEO that includes
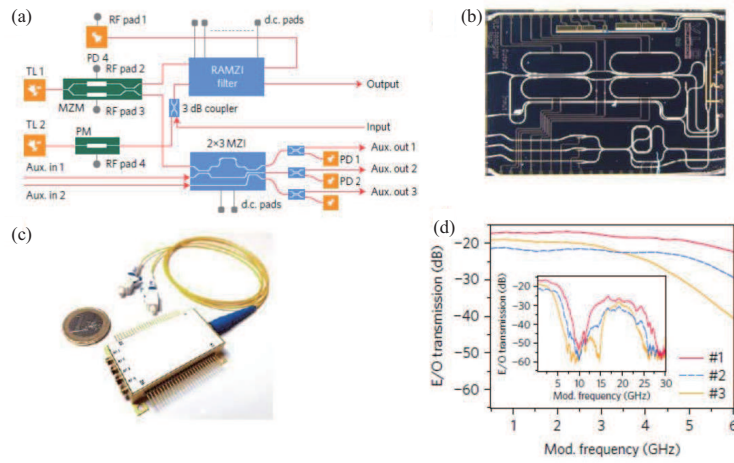
Figure 41 (Color online) (a) Schematic of the InP chip, showing all the main building blocks of a monolithic tunable RF-Photonic filter; (b) image of a fabricated die (6 mm × 4 mm); (c) packaged chip; (d) measured magnitude transfer function response for three different current sets in the thermo-optic heaters. TL: tunable laser; MZM: dual-drive Mach-Zehnder modulator; PD: photodetector; PM: phase modulator; MZI: Mach-Zehnder interferometer (after [171]).
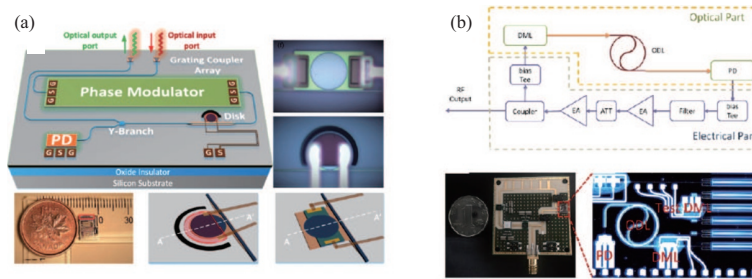

Figure 42 (Color online) Schematic of the proposed integrated photonics OEO (after [172, 173]). (a) Perspective view of the proposed OEO; the fabricated chip prototype captured by a microscope camera; perspective view of the MDR with a top-placed micro-heater; perspective view of the MDR with a p-type doped micro-heater; image of the MDR with a top-placed micro-heater; and an image of the MDR with a p-type doped micro-heater (after [172]). (b) Schematic and photographs of the InP OEO, a photograph of the fabricated device, the photonic part of the OEO. DML: directly modulated laser; ODL: optical delay line; PD: photo detector; EA: electrical amplifier; ATT: attenuator (after [173]).

a high-speed PM, a thermally tunable micro-disk resonator (MDR), and a high-speed PD has been proposed and experimentally demonstrated. The basic features of this circuit are shown in Figure 42(a). The OEO was able to generate a microwave signal with a frequency tuning range from 3 to 8 GHz. The phase noise of the generated microwave signal was measured to be around −80 dBc/Hz at a 10-kHz offset frequency, which is still far from the values achieved with fiber-based OEOs.

In [173], an InP based integrated reconfigurable optoelectronic oscillator has been reported and experimentally demonstrated. In this case, the chip contains the active elements and also all the main RF components are included. The storage cavity here was implemented by means of a spiral waveguide rather than by an integrated resonator. All of the devices needed in the optoelectronic oscillation loop circuit were monolithically integrated on a chip within a size of 5 cm ×6 cm. By tuning the injection current, the output frequency of the proposed OEO was tuned from 7.30 to 8.87 GHz featuring the phase noise value of around −91 dBc/Hz@1 MHz.

Arbitrary radiofrequency waveform generators. Microwave arbitrary waveform generation (AWG) can find very useful applications in future 5G communication systems, pulsed radar, and modern instrumentation. The currently available electronic arbitrary waveform generation is limited in frequency and bandwidth to around 22 and 6 GHz, respectively. The use of photonic techniques provides a promising solution to overcoming the main limitations encountered in electronics systems and a variety of techniques have been proposed [88, 89, 174] including direct space-to-time mapping, spectral shaping and wavelength-to-time mapping and temporal pulse shaping to generate microwave waveforms in the gigahertz and multiple gigahertz regions. Many proofs-of-concept and first demonstrations of these techniques have been implemented through bulky fiber-opticbased systems and clearly an on-chip integrated pulse
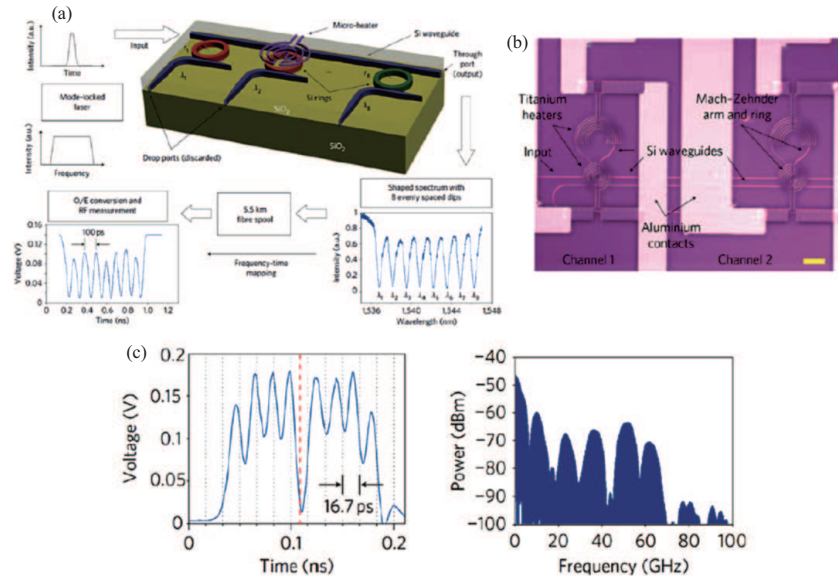
Figure 43 (Color online) On-chip arbitrary waveform generation using cascaded of 8 microring resonators in SOI platform. (a) Waveform generator system; (b) optical image of the pulse shaper; (c) example of waveform generation at 60 GHz (after [175]).

shaper is thus a desirable solution to overcome the limitations commonly associated with these conventional bulk optics pulse shapers.

Khan and co-workers [175] at Purdue University demonstrated an integrated ultrabroadband microwave arbitrary waveform generator that incorporates a fully programmable spectral shaper fabricated on a silicon photonic chip. The spectral shaper is a reconfigurable filter consisting of eight add/drop microring resonators on a silicon photonics platform. Ultra-compact cross-section (500 nm×250 nm) silicon nanowires were used to fabricate the rings. The typical bending radius used was 5 μm and the waveguide propagation loss was around 3.5 dB/cm. This spectral shaper programmability is achieved by thermally tuning both the resonant frequencies and the coupling strengths of the microring resonators. A cartoon of the spectral shaper and an optical image showing two channels of ring resonators with micro-heaters are shown in Figures 43(a) and (b), respectively.

The principle of the photonic microwave arbitrary waveform generation system implemented here is shown in Figure 43(a). The spectral shaper is used to modify the spectrum emitted from a mode-locked laser. The shaped spectrum then undergoes wavelength-to-time mapping in a dispersive device, which in this case is a length (5.5 km) of optical fiber, before being converted to the electrical domain of a microwave waveform using a high-speed photodetector. By incorporating the spectral shaper into a arbitrary waveform generation system, a variety of different waveforms were generated, including those with an apodized amplitude profile, multiple π phase shifts (Figure 43(c)), two-tone waveforms and frequency-chirped waveforms at the central frequency of 60 GHz.

The main drawback of this design stems from the fact that it requires a dispersive element for the frequency to time mapping operation. This of course can be provided on the flight by an optical fiber link if the signal is to be generated at a centralized site and then delivered to a remote location for radiation. If, however, the full signal generation is to be achieved on-chip, then the use of the dispersive delay line must be avoided and then resorts to the alternative techniques. Figure 44 shows the results of a silicon chip based on spectral shaping as well, but where the time delays for each spectral component are provided by separate tunable delay lines, implemented with SCISSORS [176].

The AWG layout is shown in Figure 44(a). An input ultra-fast pulse is sampled by eight microring add-drop filters of different radii R_i (λ_i denotes the associated resonance wavelength, $i = 1, 2, \ldots, 8$) that download and produce eight replica pulses. Since the wide bandwidth of the input pulse covers several free spectral ranges of the silicon microrings, each replica generation microring downloads up to six small slices of the input spectrum. Although in the time domain, each pulse replica actually consists of a series of densely packed exponentially decaying amplitude pulses. Only the envelopes of the pulse replicas can be detected during optical/electrical conversion, the width of each pulse replica's envelope being inversely proportional to the optical round-trip time in the ring and the ring's power coupling coefficients to bus
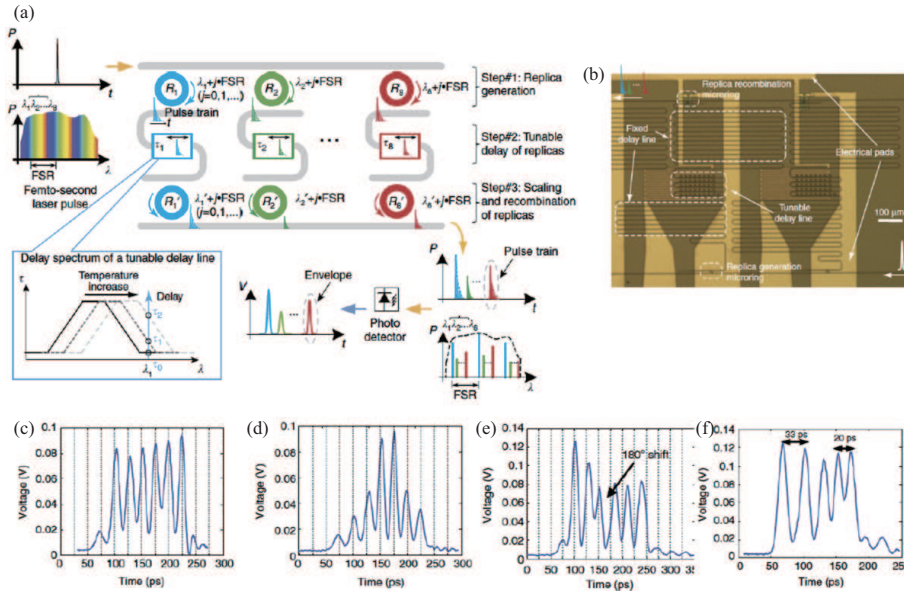
Figure 44 (Color online) Chip design (a) and fabricated layout (b) for a reconfigurable arbitrary waveform generator, using wavelength to time mapping and selective tunable delay lines based on SCISSORS. (c)–(f) Examples of generated waveforms. (c) 40-GHz uniform RF burst; (d) 40-GHz apodized RF burst; (e) 40-GHz burst with an intermediate p phase shift; (f) frequency up-chirped burst from 30 to 50 GHz (after [176]).

waveguides. The frequency spacing between the selected channels in the filter bank can be arbitrary and non-uniform as long as they are not too small to cause interference between channels.

After the pulse replication is performed in each stage for a given wavelength region of the pulse, a selective delay is impressed by means of an on-chip tuneable delay element consisting of a fixed part and a tuneable part shown in Figure 44(b). The fixed part is a long waveguide with a delay value at multiples of a given set value τ ps, and each channel has τ ps more delay than the previous one. The tuneable part consists of cascaded microring SCISSOR all-pass filters, which are activated to provide more or less additional delay. A final stage composed of another eight microring add-drop filters of different radii R_i provides the final amplitude for the wavelength sample and combines all the wavelength samples into a common output waveguide bus. Figures 44(c)–(f) provide examples of several AWG waveforms generated by reconfiguring the chip parameters.

A particular waveform of interest for radar and communication applications is the linearly chirped microwave waveform (LCMW). For LCMW generation, the optical spectral shaper should have a spectral response with an increasing or decreasing FSR. The approach based on spectral shaping and wavelength to time (SS-WTT) mapping provides large flexibility, since the spectral response of the spectral shaper can be easily reconfigured.

The key component in an SS-WTT mapping system is the spectral shaper. In fact, the configuration proposed in [176] can provide an increasing or decreasing FSR by thermal tuning of the MRR. However, the chirp rate that can be obtained is quite limited. To generate an LCMW with a large chirp rate, other approaches have been recently proposed and demonstrated in silicon photonics and fabricated using a CMOS-compatible technology with 193-nm deep ultraviolet lithography. Figure 45(a) shows the layout of a spectral shaper [177] that consists of multiple cascaded MRRs with largely different radii. It has an MZI structure incorporating multiple cascaded MRR. The incident light beam is split by the first adiabatic 3-dB coupler into two beams that travel through the upper and lower arms of the MZI. Each ring selectively transfers the optical power at its resonance wavelength from the through-port waveguide to its drop-port waveguide (note that different colors of the rings shown in the figure indicate that each ring is designed to have a different radius and therefore a different resonant wavelength). The spacing between two neighboring rings is large enough to avoid mutual interferences. In the upper and lower waveguides, S-shape waveguide bends, which are designed using Bezier curves to minimize the mode mismatch and thus reduce the waveguide bending loss, are added to accommodate the change of the rings. The resonant wavelengths from both waveguides are then recombined at the first adiabatic 3-dB coupler and constructively interfere as reflected signals while non-resonant wavelengths are recombined
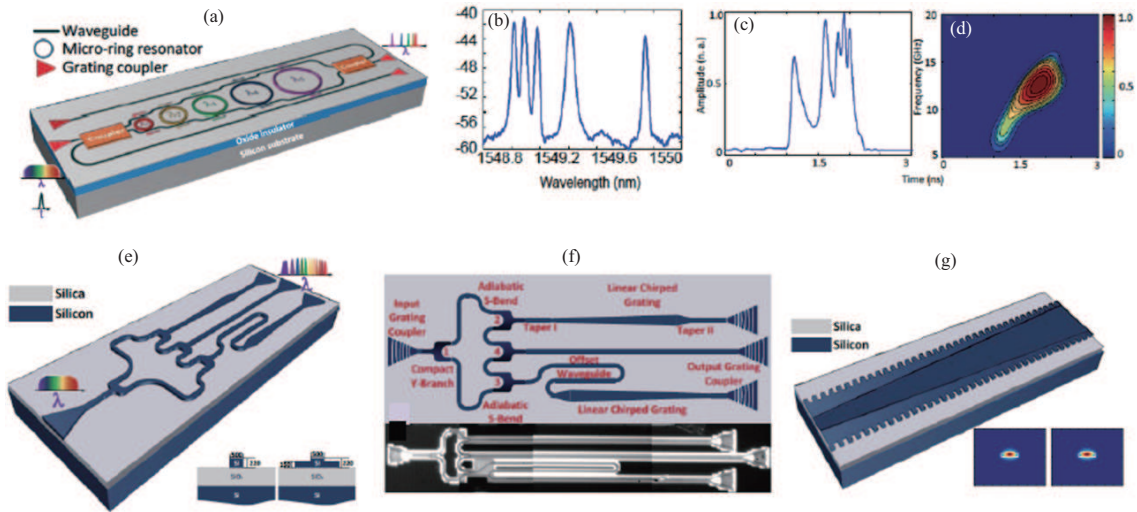
Figure 45 (Color online) Silicon Photonics chirped microwave signal generators reported in [178]. (a) Schematic view of a silicon-based on-chip spectral shaper consisting of five MRR; (b) measured spectral response of the spectral shaper consisting of five cascaded MRRs; (c) and (d) generated LCMW and its spectrogram when for the spectral shaper consisting of five cascaded MRRs; (e) perspective view of the silicon-based on-chip optical spectral shaper incorporating LC-WBGs (inset: wire waveguide (left) and rib waveguide (right)); (f) schematic layout of the designed on-chip spectral shaper, and image of the fabricated spectral shaper with the length of the offset waveguide equal to the length of the LC-WBG captured by a microscope camera; (g) view of an LC-WBG (inset: simulated fundamental TE mode profile of the rib waveguide with the rib width of 500 nm (left) and 650 nm (right)).

at the second adiabatic 3-dB coupler at the transmission port.

In order to achieve maximum reflection power, each ring is designed to work in the critical coupling condition. By carefully designing the ring radii, at the reflection port, the reflection peaks with a linearly increasing spacing can be achieved. Figures 45(b)–(d) show, respectively, the spectral response, the generated waveform, and its spectrogram at the reflection port of an on-chip spectral shaper consisting of five MRRs.

While compared with the work in [175], the distinct feature of this optical spectral shaper is that the MRRs are designed to have largely different radii for the generation of an LCMW with a much higher chirp rate (17.2 GHz/ns compared to 8 GHz/ns), the TBWP of this configuration is quite small (18.7); hence, for practical applications where large pulse compression is required, an LCMW with a much greater TBWP is needed.

A spectral shaper designed to provide a much larger TBWP [178] is shown in Figure 45(e). The shaper layout and photograph are shown in Figure 45(f). It has an MZI structure that incorporates two identical linearly chirped waveguide Bragg gratings (LC-WBGs) with opposite chirp rates in its two arms. An input light wave is split by a compact Y-branch into two beams to travel through the LC-WBGs in the upper and lower arms. Spectral components of the light waves of different wavelengths are reflected from different positions in the LC-WBGs. By the second and the third Y-branches, the reflected light waves are collected and recombined at the fourth Y-branch. The combined light wave is guided to an output grating coupler to couple the light out of the chip. When recombined, due to the optical interference, the optical spectral shaper has a spectral response with a wavelength-dependent FSR, which is required to generate an LCMW. The central frequency of the generated LCMW can be controlled by using an offset waveguide added in the lower arm of the spectral shaper to control the length difference between the two arms. By properly designing the LC-WBGs and choosing the length of the offset waveguide, the spectral response of the spectral shaper can be controlled to have a symmetrical, uniformly increasing or decreasing FSR. The two LC-WBGs are the key components in the spectral shaper. These gratings are realized by introducing periodic sidewall corrugations on the slab as shown in Figure 45(g). Keeping the grating period uniform and linearly increasing the width of the rib along the grating, a linear chirp is produced since the effective refractive index is linearly increasing as the rib width increases in a definite range. Using this design, LCMW with TBWP values over 200 have been reported.

Frequency combs. The generation of optical combs on a chip [179] enables several applications such as the precise measurement of optical frequencies through direct referencing to microwave atomic clocks and the production of multiple taps for high sidelobe rejection signal processors. Recently the generation of
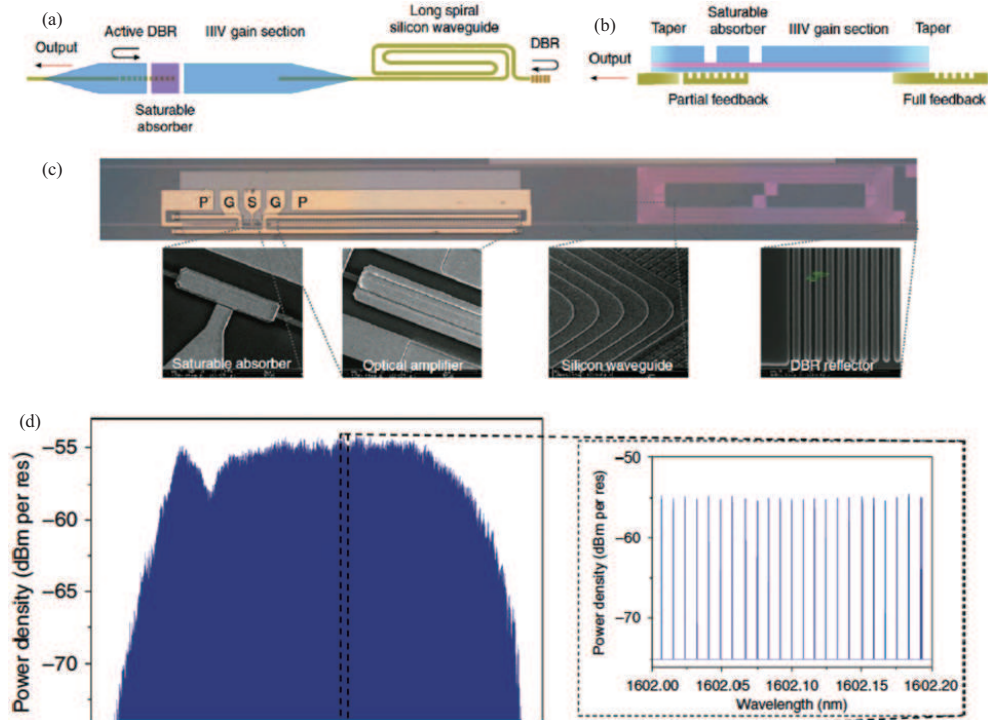
Figure 46 (Color online) (a) Top and (b) side views of a III-V on Si anti-colliding MLL comb source design (after [180]). (c) Microscope image of the III-V-on-Si MLL. Insets: scanning electron microscope images of various constituent parts of the laser. (d) Optical comb generated by the passively locked 1 GHz MLL. Inset: detail of evenly spaced optical modes in the comb.

optical frequency combs through the nonlinear process of continuous-wave optical-parametric oscillation using micro-scale resonators or (also known as optical micro-combs) has attracted significant interest since these devices have the potential to yield highly compact and frequency agile comb sources. Several authors have reported the generation of optical frequency combs from highly-robust CMOS-compatible integrated microresonator optical parametric oscillators (see a complete and updated review in [179]), however we will not delve deeper into this approach as it is based on nonlinear effects, which are outside the scope of this article.

Combs have been traditionally based on bulky and high-cost femtosecond lasers with line spacing in the range of 100 MHz to 1 GHz. However, their integrated and low-cost counterparts, i.e., integrated semiconductor mode-locked lasers, are limited by their large comb spacing, a small number of lines, and broad optical linewidth. However, a recent study [180], has reported a demonstration of a III-V-on-Si comb laser that can function as a compact, low-cost frequency comb generator after frequency stabilization. Figure 46 shows the layout and the emitted spectrum of the integrated comb source under optimum operating conditions.

The use of low-loss passive silicon waveguides enables the integration of a long laser cavity, which enables the laser to be locked in the passive mode at a repetition rate of 1 GHz. The optical spectrum features a 12 nm bandwidth comb structure with 10-dB output optical spectrum. The very small optical mode spacing results in a dense optical comb of over 1400 equally spaced optical lines with sub-kHz 10-dB radio frequency linewidth. Furthermore, the narrow longitudinal mode linewidth ($<$400 kHz) indicates notably stable mode-locking.

The main problem with the former approach is the reconfigurability, as it is set by the cavity length and might require the use of external phase filters to tune the repetition frequency. One solution, which can also be integrated on a chip is to generate the comb spectrum by cascading amplitude and phase modulators at the output of a continuous-wave laser source [181], driven by specially tailored RF waveforms to generate an optical frequency comb with very high spectral flatness. In [181] this technique has been experimentally demonstrated and shown to lead to extremely flat comb spectrum with a spectral power variation below 1 dB. The number of comb lines that can be generated is limited by the power handling capability of the phase modulator, and this can be scaled without compromising the spectral flatness.
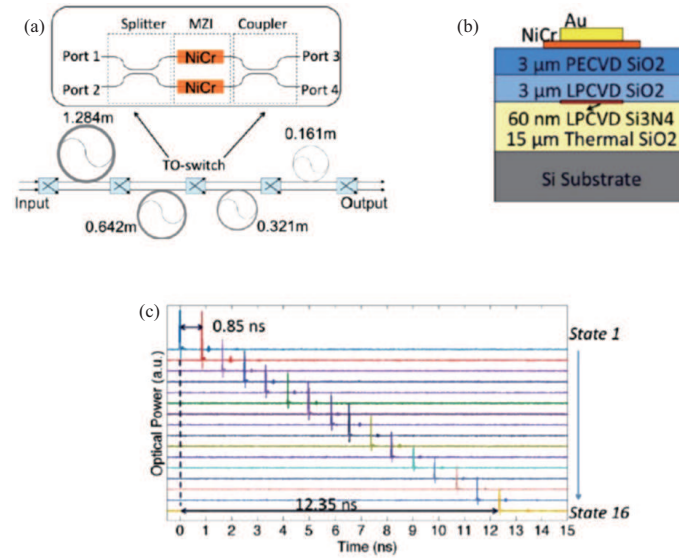
Figure 47 (Color online) Integrated 4-bit switched optical delay line (after [194]). (a) Circuit layout; (b) waveguide cross section; (c) optical output for all delay settings.

Optical delay lines. Reconfigurable optical delay lines are classified into two main categories: variable-length delay lines (VLDLs) and variable-propagation-velocity lines (VLDLs) based on optical filters. VLDLs can be implemented by means of the so-called switched delay lines (SDLs), where the amount of delay is reconfigured in discrete steps by selectively using integrated optical switches in a cascade of optical waveguide paths of different lengths. SDLs have been proposed in a completely integrated photonics form allowing increased compactness and improved stability versus thermal and mechanical stress, with reduced delay switching times reaching a few tens of nanoseconds [109]. Higher delay resolution (required for antennas operating at high frequency) can also be improved with an integrated photonics approach. A number of photonic integration platforms have been used including polymer technology [182–184], silica [185–188], LiNbO$_3$ [189], GaAs [190, 191], and InP [192, 193]. Figure 47 illustrates the case of a recent example [194] using an ultralow-loss Si$_3$N$_4$ substrate featuring a fully integrated 4-bit TTD line capable of delays above 12 ns, corresponding to about 2.4 m of propagation length, on a chip area of 4.5 cm×8.5 cm, with waveguide losses as low as 1 dB/m.

VPVL lines can be implemented using optical filters or dispersive optical transmission lines. Their main advantage as compared to VLDLs resides in their capability for continuous delay tuning that translates into the possibility of continuous steering of the antenna beam direction. Recent efforts have been directed towards their on-chip implementations using photonic crystals, integrated Bragg gratings and integrated filters. Photonic crystals have been employed as a single fully integrated dispersive delay element. Sancho et al. [195] demonstrated the use of a single, very compact, low loss photonic crystal to implement multiple variable TTDs. The operation is based on the slow-light properties of photonic crystals, in which the group delay can be increased to very high values depending on the wavelength demonstrating a 1.5-mm-long device capable of generating delays up to 70 ps with losses below 10 dB over the complete 0–50-GHz band. More recently Zhang and Yao [196] have proposed an electronically reconfigurable Bragg grating device that can operate as an electrically tunable linearly chirped grating providing a dispersive delay line. The device layout is shown in Figures 48(a)–(d). It consists of multiple series-connected uniform Bragg sub-grating sections and a Fabry-Perot (FP) cavity section in the center of the grating. Each uniform Bragg sub-grating section incorporates an independent lateral PN junction as shown in Figure 48(b), and between two neighbouring sections there is an undoped grating to function as an insulator. Distributed electrodes are connected to the independent PN junctions.

By applying a bias voltage to a PN junction, the refractive index of the grating in that particular section could be tuned locally based on the free-carrier plasma dispersion effect as seen in Figure 48(c). Thus, the entire index modulation profile of the grating can be electrically reconfigured by field programming all the bias voltages enabling the grating to have diverse spectral characteristics for diverse functionalities. Since the uniform sub-gratings in the left and right sections can be independently tuned, by shifting the spectral response of one of the two uniform sub-gratings with different bias voltages, the device can be
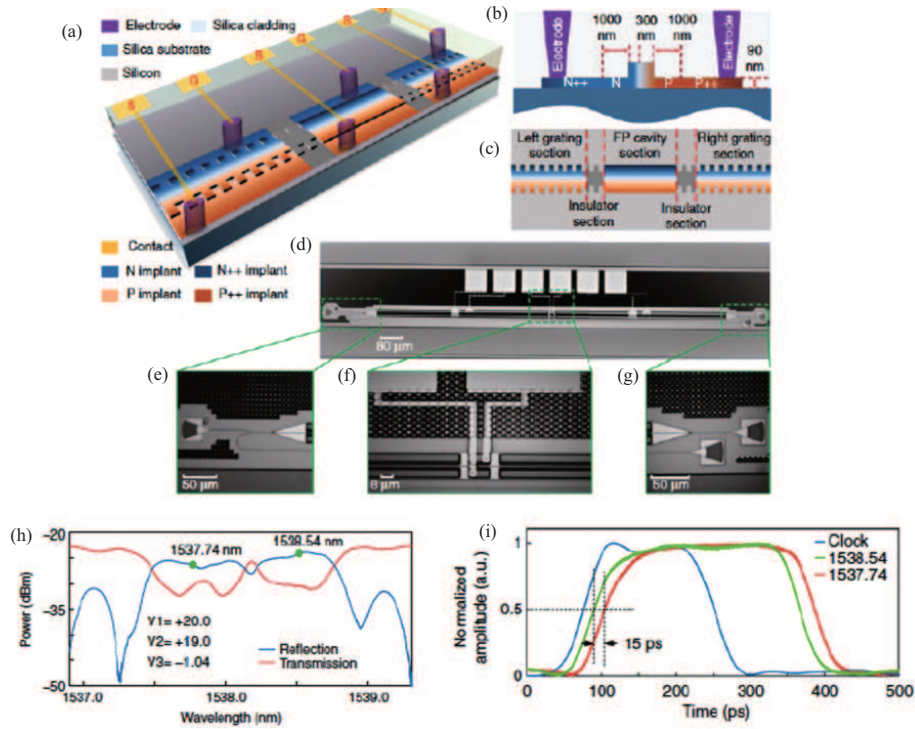
Figure 48 (Color online) Electrically tunable silicon Bragg grating (after [195]). (a) Perspective view of the grating on a silicon chip. (b) Cross-sectional view of the grating rib waveguide. (c) Top-view of the grating. (d)–(g) Microscope camera images of the fabricated grating, the input grating coupler and compact Y-branch, the FP cavity section, and the transmission and reflection grating couplers. (h) Reflection and transmission spectra when the device is reconfigured to be a chirped grating. (i) Ime-domain measurement when the fabricated grating is reconfigured to be a chirped grating.

reconfigured to be a chirped grating.

Figure 48(h) presents the measured reflection and transmission spectra of the chirped grating when a maximum reverse bias voltage of $+20$ V is applied to the left PN junction and a forward bias voltage of -1.04 V is applied to the right PN junction. The 3-dB bandwidth of the spectra is increased to be 1.29 nm, which is larger than the 0.79 nm corresponding to the uniform grating setting. Figure 48(i) demonstrates the time delay function, a microwave rectangular pulse with a temporal width of 290 ps is modulated on two optical carriers with different wavelengths and sent to the grating. The two reflected pulses experience two different time delays since they are carried by two different wavelengths at 1537.74 and 1538.54 nm. Specifically, the pulse carried by the optical wavelength at 1537.74 nm is reflected by the right sub-grating from its center. The pulse carried by the optical wavelength at 1538.54 nm is reflected by the left sub-grating from its center. The time delay difference is 15 ps. Larger time delays are possible if the length of the grating is increased, and more independent grating sections are incorporated for high-level tuning in terms of group delay and chirp rate.

Integrated optical filters have also been used to implement broadband tunable optical delays. For example, cascaded optical ring resonators (ORRs) have been demonstrated in silica [185, 188], TriPleX [196–198] and SOI [199, 200]. This solution combines optical ring resonators comprising tunable phase shifts in the ring loops and tunable couplers. The basic principle is that the optical ring resonators can be configured to be an optical all-pass filter [159, 198], as shown in Figure 49(a), featuring a group delay at the resonance frequency, which can be set to be much larger than the round-trip delay of the ring loop and can be controlled via the coupler. This enables the realization of long delays using a small chip area, which can be further increased by cascading multiple RRs in series to form a SCISSOR structure, as illustrated in Figure 49(b). A limitation of this scheme resides in the fact that the delay $\times$ bandwidth product is constant and thus, increasing the available delay at resonance implies a reduction in the available bandwidth. This can be overcome by slightly detuning the resonances of the optical ring resonators in the cascade as reported and experimentally demonstrated in [201] for an 8 ORR SCISSOR structure fabricated in Si_3N_4. Figure 49(c) provides the basic waveguide structure, individual and SCISSOR layouts and a photograph of one of the fabricated optical ring resonators, including the
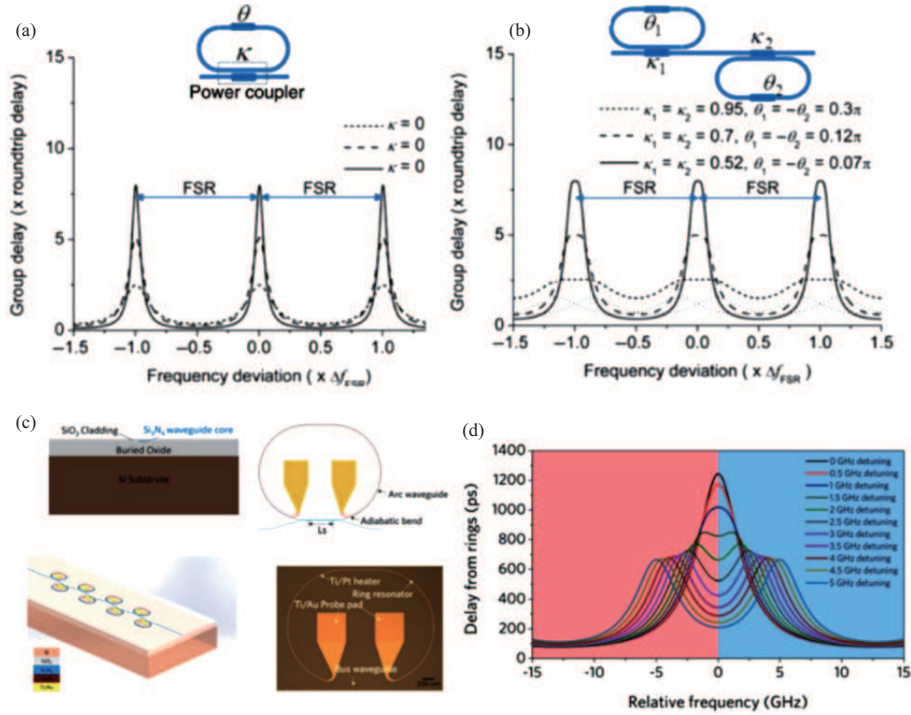
Figure 49 (Color online) Tunable resonant delay line based on optical ring resonators acting as an all-pass filter (after [196]). (a) Single ORR structure; (b) cascade ORR structure; (c) details from an 8 ORR SCISSOR fabricated in Si_3N_4 (after [201]); (d) bandwidth increase by slightly detuning the resonances of the rings I (c) (after [201]).

electrodes placed on top of the ring waveguide to tune its resonance through the thermo optic effect.

Finally, a novel concept to implement OTTDLs is based on the principle of index-variable delay lines. Here true-time delay control can be realized through varying the group index/ propagation velocity in the waveguides. One efficient way to achieve this is by the inscription of subwavelength gratings (SWGs) [202] in SOI waveguides by alternating sections of silicon and silica. These waveguides can provide a variable group delay by changing the duty cycle relationship between the silicon section within the grating period. In [202], a 4-tap OTTDL is reported where each tap is based on one SWG waveguide, and all waveguides have the same length of $L = 8$. The SWG waveguides are realized by alternating periodically segments of silicon and silica, with a period of $\Lambda = 250$ nm along the propagation direction. Figure 50 shows the schematic and performance operation for an input 1 ps Gaussian pulse featuring a 9 ps incremental delay between waveguides by choosing four different values of the SWG duty cycles (60%, 50%, 40% and 30%).

Phase shifters. In addition to delay, phase shifting is also attractive for a number of signal processing applications. Tunable RF phase shifters have been demonstrated using SOI [203, 204] and hybrid SOI and III-V semiconductor ring resonators [205]. Here the phase shift is obtained after beating the optical carrier and the single sideband RF modulating signal [206]. The principle is shown in Figure 51 for a structure composed of two optical ring resonators in cascade (to achieve a full 2π phase excursion [203]). One of the two carriers is placed in coincidence with the resonance of the all-pass transfer function of the resonator where it experiences a different phase-shift compared to the component that is outside the resonance. Tuning is achieved either by moving the resonance of the ring cavity through an internal phase shifter or by tuning the optical carrier.

Both tunable time delay and phase shift operations can be incorporated into a single photonic chip using the separate carrier tuning (SCT) scheme, proposed by Morton and Khurgin [207]. Burla and co-workers [208] have reported and demonstrated the SCT scheme altogether with optical single sideband filtering monolithically integrated in a single chip. The circuit, shown in Figure 52(a) consists of a reconfigurable optical delay line, a separate carrier tuning unit, and an optical sideband filter. The optical sideband filter, a RAMZI, removes one of the radio frequency sidebands of a double-sideband intensity-modulated optical carrier. The ODL and separate carrier tuning units are individually implemented using a pair of cascaded optical ring resonators. The group delay of the signal sideband is changed by tuning the resonance frequencies and the coupling factor of the optical ring resonators in ODL. This is
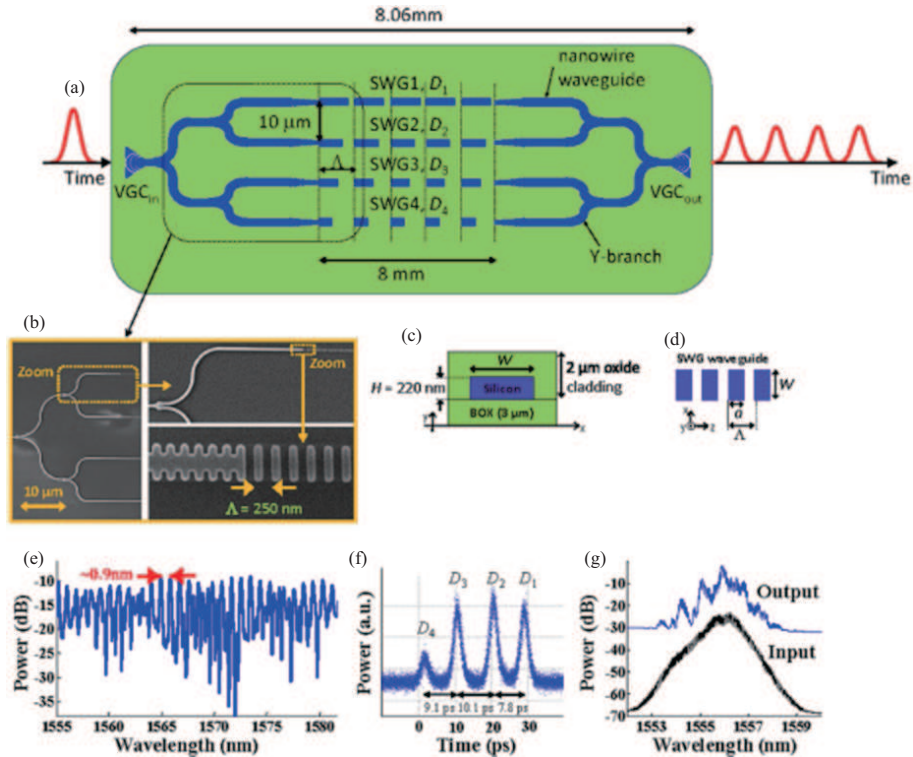
Figure 50 (Color online) (a) Schematic and (b) an SEM image of our fabricated 4-tap OTTDL structure based on SWG waveguides in SOI reported in [202]; (c) waveguide cross-section and (d) parameters of the SWG waveguides; (e) measured power spectral response of the fabricated OTTDL; (f) generated time-domain pulse train at the output of the fabricated OTTDL device in response to a single input optical pulse; (g) input and amplified output signal spectra.
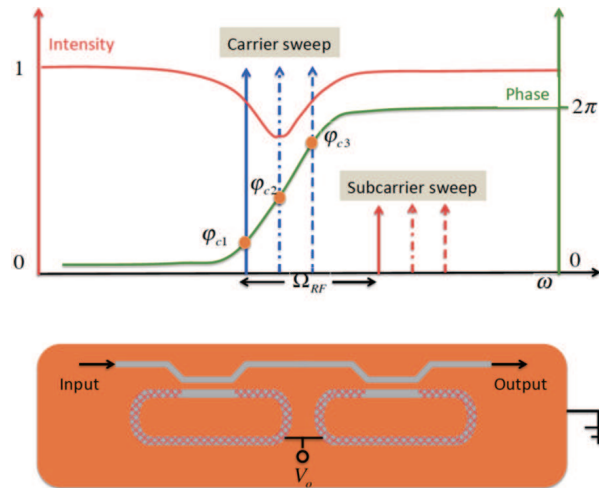

Figure 51 (Color online) Illustration of the basic principle behind the implementation of a tunable RF phase shifter using a resonant integrated resonator and a single sideband modulated signal (after [206]). The tuning of the chip resonance is here performed using a voltage activated phase-shifter inside the cavities.

supplemented by applying an additional phase shift in the $[0, 2\pi]$ range to the carrier. In [208], this module was employed to demonstrate of a two-tap microwave photonic filter whose notch position could be shifted by 360° over a bandwidth of 1 GHz. The operation of the different modules in the chip is depicted in Figures 52(b)–(d).

Waveguide Bragg gratings realized on SOI can also implement tunable ultrabroadband phase shifts in conjunction with optical single-sideband modulation. In [207], a compact (130-nm long) device has been employed to create broadband phase shifts for RF frequencies beyond 900 GHz.

Beamformers. In phased array antennas a beam is formed and steered to a given angle by adjusting
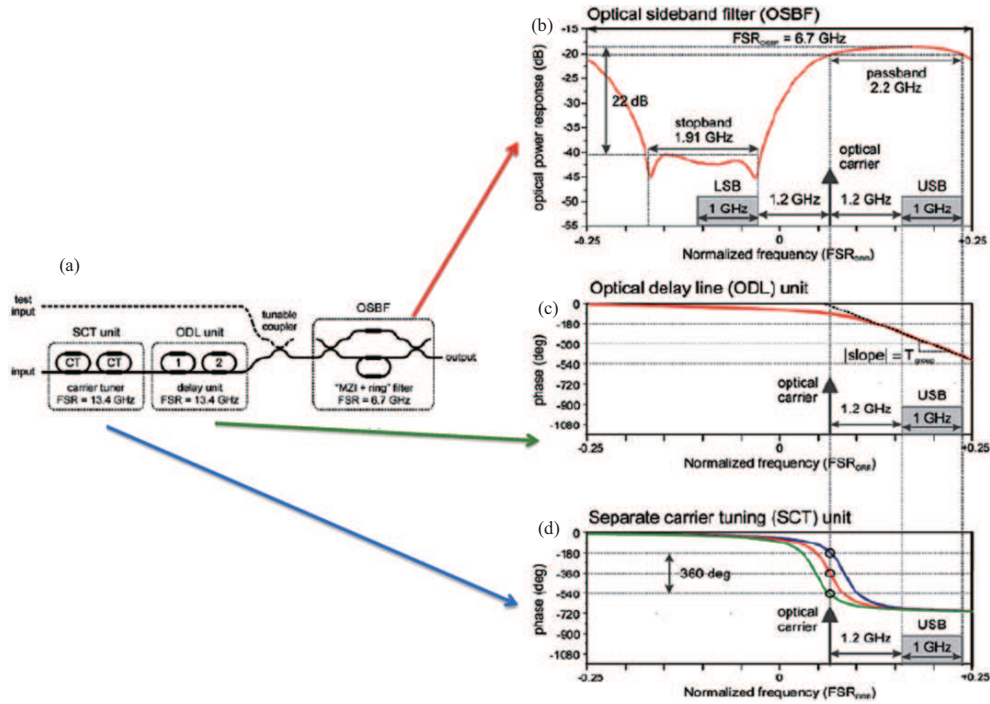
Figure 52   (Color online) Reconfigurable circuit simultaneously implementing tunable phase shifting and delays using the separate carrier tuning technique (after [208]). (a) Circuit layout; (b) operation of the tunable SSB filter; (c) operation of the ODL for the radiofrequency sideband; (d) operation of the phase shifter for the optical carrier.

the phase relationship between a given number of radiating elements [1–3]. This principle of operation works correctly for narrowband signals but, in the case of wideband signals, a limitation arises since if a constant phase shift is produced from element to element, the beam pointing is different for different frequency components. This deleterious effect, known as beam squint, can be compensated by using tunable delay lines, rather than by employing phase shifters. Thus, it turns out that both delay lines and phase shifters can be advantageously employed to implement beam steering circuits, each one in a particular context. Attending to the different types of delay lines and phase shifters considered in the prior section there are three categories of integrated photonic beam formers that can be implemented: wideband beam formers based on discretely tunable delay lines TTD [209], wideband beam formers based on continuously tunable delay lines TTD [210–217] and narrowband beam formers based on optical phase shifters [189, 218, 219].

Figure 53 shows the configuration and some measured results of a complete tunable broadband beam former based on optical ring resonators arranged in a binary-tree network architecture reported in [216] and fabricated in TriPleX waveguide technology. The beamformer was composed of a 4-element array shown in Figure 53(a), subsequently completed by 1×4 RF phase shifting stages to feed a final 1×16 linear antenna array as shown in Figure 53(b). Basic true-time delays are obtained using the ODL configuration shown in Figure 53(c). Delays up to 236 ps were demonstrated over a bandwidth of 2 GHz for Ku-Band satellite communication applications [216] as shown in Figure 53(c). The beam former elements could be configured as true delay lines or as pure phase shifters. In the first case it provided squint-free operation in the (10.7–12.75) GHz, while in the second the quint effect was clearly appreciable, as shown in Figure 53(d).

6.3   Programmable integrated microwave photonics

The fact that several ASPIC designs have proven to operate successfully as multifunctional circuits [220] raise the question of whether it is possible to design a simple and replicable photonic hardware architecture that under suitable programming could implement the different functionalities required in MWP. This so-called programmable integrated microwave photonics would be inspired on similar grounds as the field programmable gate array (FPGA) device in electronics or the digital signal processor (DSP) in advanced communications. In this section we provide some insight into the recent and currently undergoing efforts
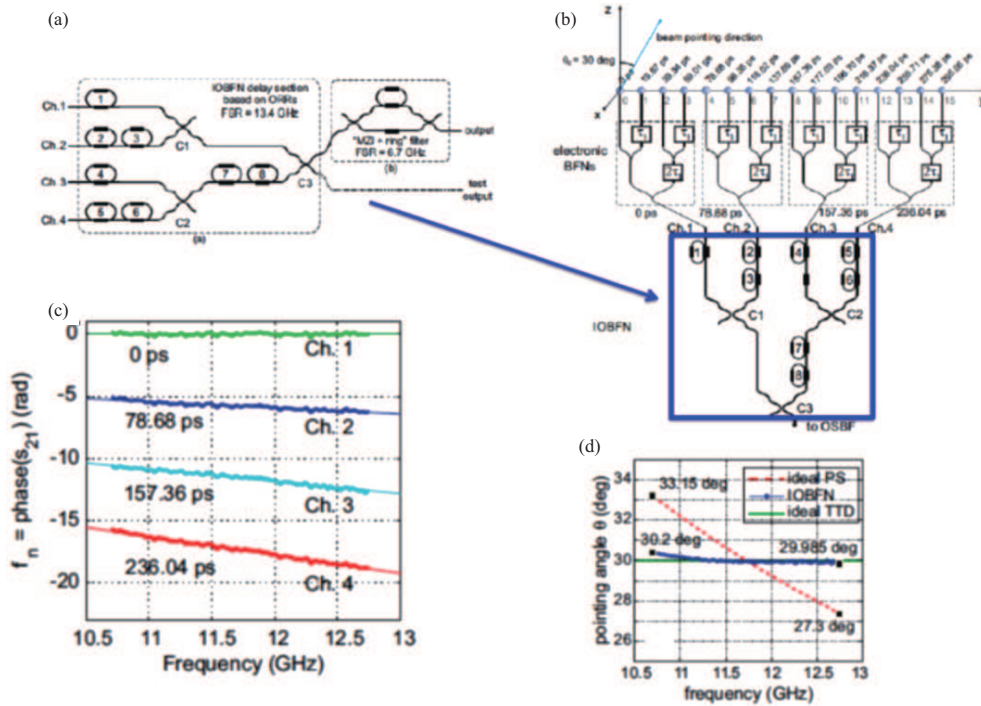
Figure 53 (Color online) Reconfigurable delay and phase 1 × 16 beamformer (after [216]). (a) Reconfigurable optical 1 × 4 circuit; (b) complete beam forming network; (c) phase shift vs. frequency in the four outputs of the optical beam forming stage; (d) squint and squint free operation in the Ku band for a targeted pointing angle of 30°.
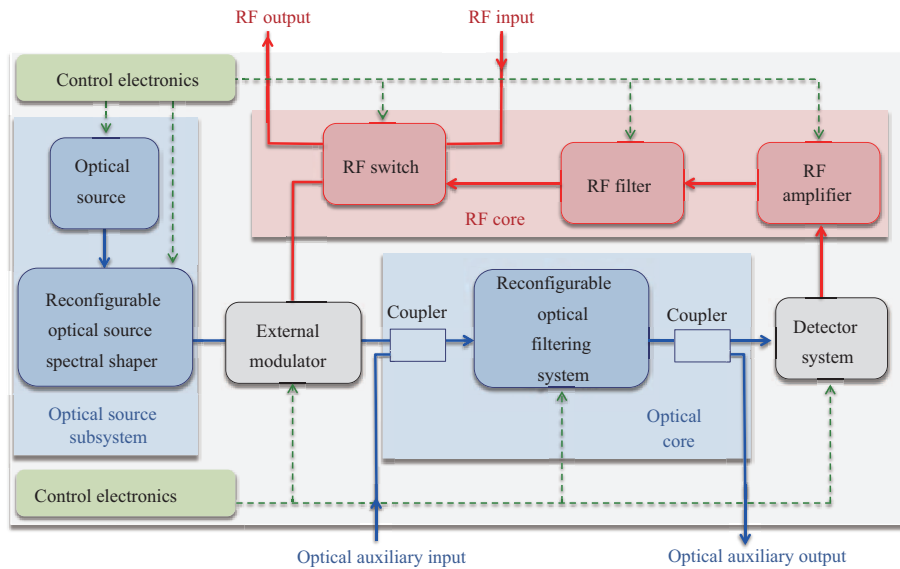

Figure 54 (Color online) Layout of an MWP transistor (after [221]).

in this field.

Early efforts. The starting point for the MWP programmable processor can be traced back to the proposal of the MWP transistor [221] shown in Figure 54, which is composed of subsystems, each of which is a collection of connected fixed-and-variable components.

The transistor configuration is obtained by opening the feedback loop of a generalized optoelectronic oscillator. As it was shown in [221], this architecture is in principle capable of performing few, but important, required functionalities in MWP provided that its optical subsystems can be reconfigured by means of suitable control signals. The main limitation of the MWP transistor is however that it does not support the reconfiguration of interconnections between its internal optical subsystems. This results in
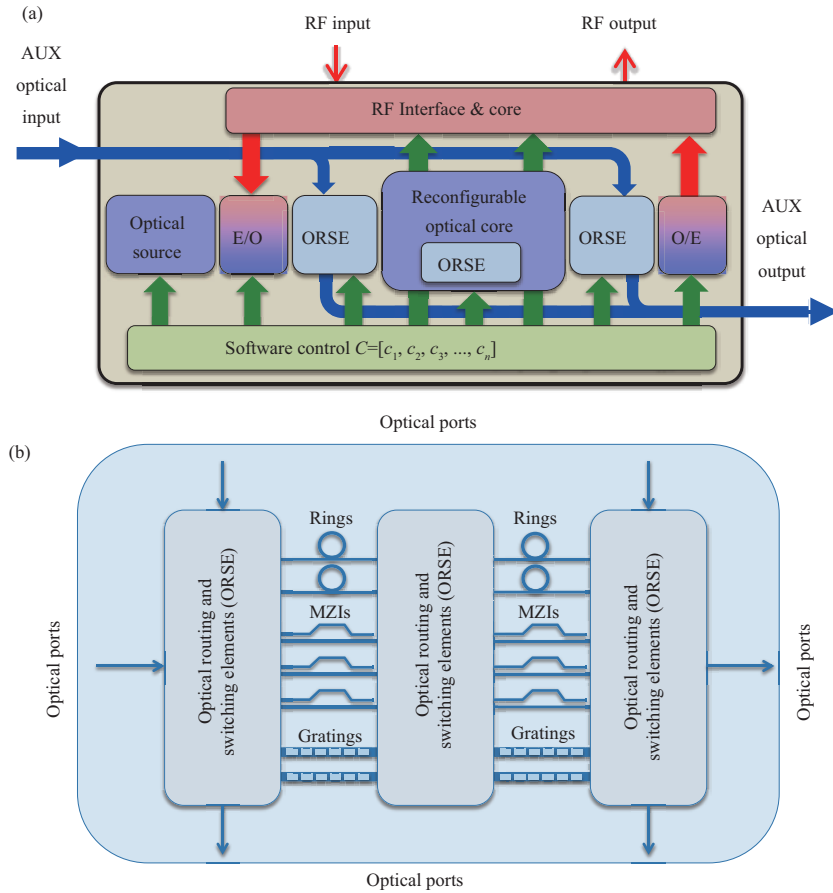
Figure 55 (Color online) (a) Layout of the universal processor (after [222]). (b) Particular implementation of the optical core using ad-hoc photonic components such as Mach-Zehnder interferometers (MZIs), ORRs and gratings connected by several optical routing and switching elements (ORSEs).

an intermediate performance between ASPIC and a universal MWP processor.

As a first alternative to going one step further in terms of flexibility, the former approach can be extended to implement a programmable MWP processor architecture [222], which incorporates optical routing and switching elements (ORSEs) into the MWP transistor layout and replaces the reconfigurable optical filtering system by a more powerful and versatile optical core. Figure 55(a) schematizes the concept.

The central element of the programmable optical processor is the optical core, where the main signal processing tasks are carried out in the photonic domain. Ideally, the optical core should be built upon a versatile architecture capable of implementing different functionalities in response to different electronic control signals. In practice, among the reconfigurable photonic circuits proposed in the literature, the ones that could especially emerge as candidates for this core are either based on the cascade of finite (i.e., Mach-Zehnder interferometers) or infinite (i.e., ring cavity) impulse response cells or a combination of both. These structures feature periodic filters and allow for bandwidth reconfiguration and notch tunability by moving the zeros and poles along the z-plane. Thus, to further increase the degree of flexibility of the processor, the former configuration can be extended with a subsystem of switched optical signal processing elements including different types of fixed and reconfigurable filtering structures and interconnections, as illustrated in Figure 55(b). This example includes FIR filters, IIR and dispersive delay lines (DDL) that can be accessible by the correct programming of the ORSEs that interconnect them. The optical routing and switching elements would need to have medium-count ports depending on the number of component banks. This architecture, as discussed in [223], is still limited in (a) flexibility, as ad-hoc designed photonic subsystems must be included and interconnected within the optical core, (b) scalability, as fixed size photonic components are the building blocks for more complex circuits and (c) loss, as a considerable number of ORSEs need to be traversed to implement complex configurations.

Waveguide mesh core processors. A more versatile optical core architecture can be obtained by following
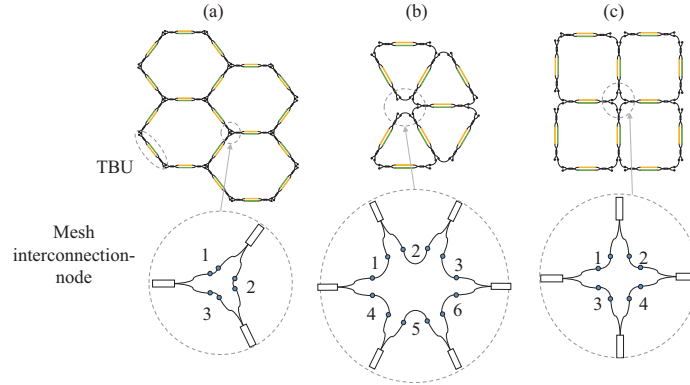
Figure 56 (Color online) Reconfigurable mesh designs [226] (upper): (a) Hexagonal type, (b) triangular type, (c) square type, and their associated interconnections points (bottom).

similar principles as those of the FPGAs in electronics [224]. The central concept is based on breaking down complex circuits into a large network of identical two-dimensional (2D) unit cells implemented by means of an MZI waveguide mesh or lattice. Zhuang and co-workers [225] have been the first to propose a programmable optical chip architecture connecting MZI devices in a square-shaped mesh network grid. The distinctive feature of this approach is that it enables both feedforward and feedbackward filtering configurations, selecting the adequate path through the mesh and providing independent tuning of circuit parameters to complex valued coefficients by introducing phase tuning elements in both arms of the MZIs to enable independent control of amplitude and phase of light at coupler outputs. Further to the square shaped mesh, other configurations, such as the triangular and hexagonal geometries have been reported [226].

Figure 56 shows three different types of waveguide mesh designs. Figures 56(a)–(c) illustrate a 4-cell arrangement for the hexagonal, triangular, and square-type meshes, respectively.

The basic building block of these meshes is a tunable coupler that must provide, independently, a complete splitting ratio tuning and phase response. This switching/tapping/de-phasing mechanism can be obtained either by exploiting the electro-refraction and/or the electro-absorption effect, or by means of the thermo-optic effect in a broadband 3-dB balanced MZI. By configuring each tunable coupler placed at each side of the cell perimeter as a switch (in either its cross or bar state) or as a tunable coupler, one can synthesize a given photonic integrated circuit topology, as shown in [227].

The upper part of Figure 57(a) shows the tunable basic unit (TBU) composed of the tunable coupler and its access (input/output) waveguides. The geometry of the latter is a function of the bending radius and varies for each mesh topology due to different angles between elements. The basic unit length (BUL) is

$$\mathrm{BUL} = L_{\mathrm{access}} + L_{\mathrm{Tunable\text{-}Coupler}}, \tag{54}$$

where L_{access} is the overall length of the access waveguide segment and $L_{\mathrm{Tunable\text{-}Coupler}}$ is the length of the tunable coupler.

Referring to Figure 57(b), the tunable basic unit can implement 3 different states: cross state switch (light path connects in_1 to out_2 and in_2 to out_1), bar state switch (light path connects in_1 to out_1 and in_2 to out_2) and tunable splitter. For a balanced MZI loaded with heaters on both arms, the splitting ratio is obtained by increasing the effective index due to the Joule effect in the upper or lower arm, producing a φ_{upper} and φ_{lower} phase shift, respectively. Once set, a common drive in both heaters will provide a common phase shift, leading to independent control of the amplitude ratio and the phase. The device matrix is defined by

$$h_{\mathrm{TBU}} = \mathrm{j}e^{\mathrm{j}\Delta} \begin{pmatrix} \sin\theta & \cos\theta \\ \cos\theta & -\sin\theta \end{pmatrix} \gamma, \tag{55}$$

where θ is $(\varphi_{\mathrm{upper}} - \varphi_{\mathrm{lower}})/2$ and Δ is $(\varphi_{\mathrm{upper}} + \varphi_{\mathrm{lower}})/2$. The coupling factor K is then defined as the $\cos^2(\theta)$ and the general loss term γ includes the effect of propagation losses in the access waveguides, the tunable coupler waveguide and the insertion losses for both 3-dB couplers.

The different waveguide mesh geometries have been analyzed and compared against a set of different figures of merit in [226], concluding that the hexagonal lattice yields the best performance for almost all
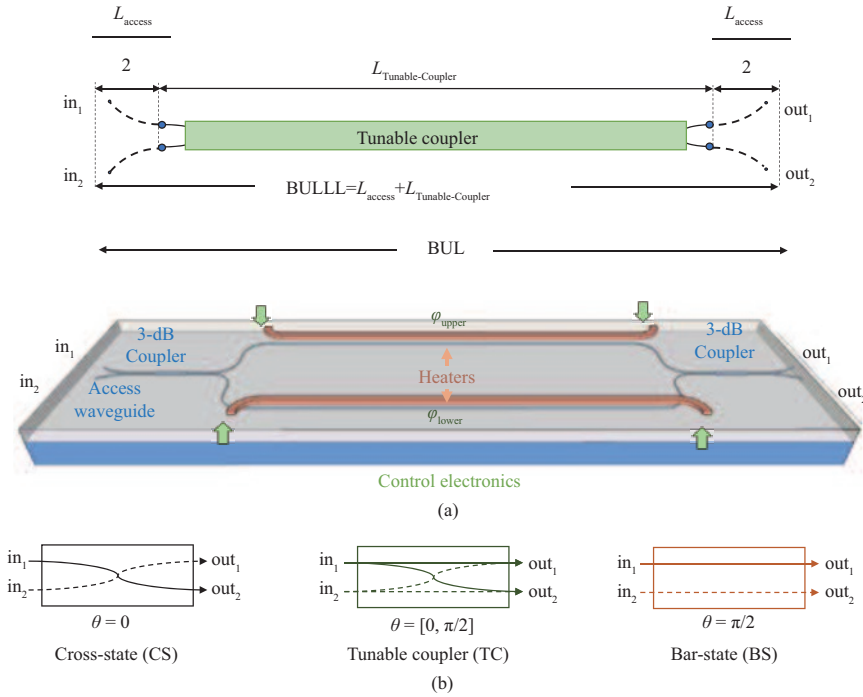
Figure 57 (Color online) (a) (Upper) Labeled schematic of a general tunable coupler acting as the basic building block of the mesh. The basic unit length (BUL) is illustrated as the sum of the tunable coupler length and the arc length of the access waveguides. (Lower) Particular case of an integrated balanced MZI-based tunable coupler. (b) Signal flow for the different tunable basic unit (TBU) configuration states (after [227]).

the performance metrics. Table 2 summarizes the results of that analysis.

For reference, the spatial tuning resolution step quantifies which is the minimum step in BUL units by which the arm length mismatch or the cavity length can be increased/decreased, the reconfiguration performance of the mesh is given by the number of filters with different spectral period values that can be implemented given a maximum value X (in BUL units) for the path imbalance in unbalanced Mach-Zehnder interferometers (UMZIs) or the cavity length in optical ring resonators. The replication flexibility gives the number of possible alternative geometries for a specific filter implementation, while the switching elements per unit area denote the amount of required BULs per surface unit to achieve equivalent functionality. Finally, the two last rows in Table 2 quantify the overall losses in the TBUs of triangular and hexagonal waveguide meshes as compared to those in the square mesh configuration. A complete definition of the figures of merit can be found in [226].

With suitable programming of a selected set of TBUs in the 2D waveguide mesh, different circuit layouts of variable complexity can be programmed over the same hardware. For example, Figures 58(a) and (b) show two implementation examples of simple UMZI FIR filters and optical ring resonator IIR filters with different path unbalance and cavity lengths, respectively. Filters with the increased degree of complexity can be built upon cascading of these simple units.

Since waveguide mesh processors are a quite recent area of research, there are only a few experimental results reported based on silicon nitride [225] and SOI [227] technologies.

Figure 59(a) shows the basic layout and photograph of the programmable optical chip architecture connecting MZI devices in a square-shaped mesh network grid proposed by Zhuang and co-workers [225]. The structure, fabricated in Si_3N_4, comprised two square cells and was employed to demonstrate simple FIR and IIR impulse response filters with single and/or double input/output ports of synthetized optical ring resonators. The processor featured an FSR of 14 GHz and is fully programmable. By appropriate programming of this processor, Zhuang et al. have demonstrated bandpass filters with a tunable center frequency that spans two octaves (1.6–6 GHz) and a reconfigurable band shape (including flat-top resonance with up to passband-stopband 25 dB extinction). They also demonstrated notch filters with up to 55 dB rejection ratio, Hilbert transformers and tunable delay lines as shown in Figure 59(b).

A recent contribution has reported the results of a waveguide mesh composed of 7 hexagonal cells fabricated in silicon on insulator [227]. The chip photograph is shown in Figure 60. The device was

Table 2 Summary of values for the figures of merit of the different mesh designs (see the definitions in [226])

Figure of merit	Triangular	Square	Hexagonal
ORR cavity spatial tuning resolution step in BUL units (the lower the better)	3	4	2* The first and second steps have a resolution of 6 and 4
MZI arm imbalance spatial tuning resolution step in BUL units (the lower the better)	3	4	2
ORR reconfiguration performance (the higher the better) (for $X = 25$ BUL)	8	6	9
MZI reconfiguration performance (for $X = 25$ BUL)	8	6	12
Switching elements per unit area compared to square % (the lower the better for a fixed value of reconfiguration performance)	+65.00%	0.00%	−36.66%
Replication ratio for ORR structures up to 16 BUL cavity length (the higher the better)	1	2.68	1.31
Replication ratio for MZI structures up to 12 BUL interferometric length (the higher the better)	1	3	3.36
$L_{access}/L_{access square}$ % for a fixed radius of curvature Ra (the lower the better)	+33.33%	+0.00%	−33.33%
Ra/Ra_{square} % for a fixed BUL value (the higher the better)	−25.00%	+0.00%	**+50.00%**
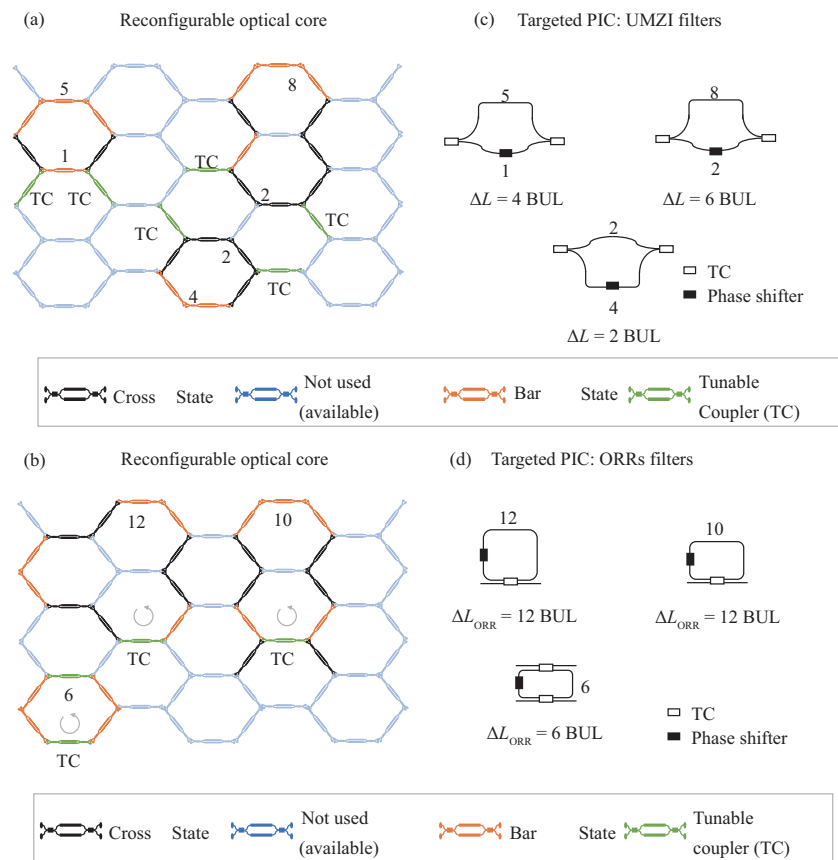
Figure 58 (Color online) (a) and (b) FIR filter implementations using a hexagonal waveguide mesh. Mesh setting for (c) three different targeted UMZI filters and (d) three different targeted ORRs [226].

fabricated at the Southampton Nanofabrication Centre at the University of Southampton. SOI wafers with a 220-nm thick silicon overlayer and a 3-μm thick buried oxide layer were used (for more details on fabrication and testing, see [227]).
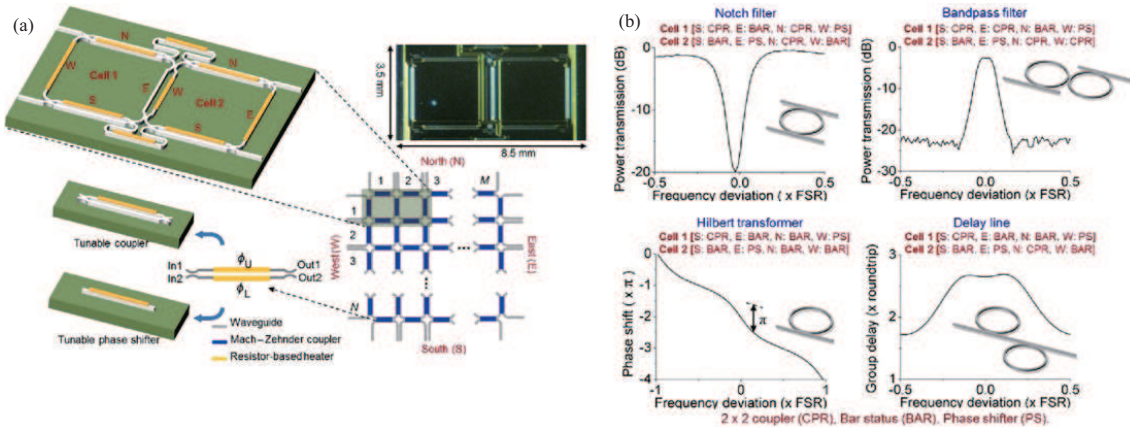
Figure 59 (Color online) (a) Schematic and a photo of the Si_3N_4 waveguide technology (TriPleX) chip implementing a 2 square cell waveguide mesh reported in [225]; (b) different programmed circuit configurations obtained by varying phase-tuning elements in the chip and the measurements of their corresponding frequency responses.
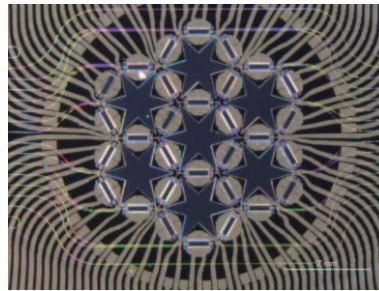

Figure 60 (Color online) Photograph of the 7-hexagonal cell waveguide mesh core fabricated in SOI and reported in [227].

The overall structure comprised 30 independent MZI devices and 60 thermo optic heaters. The waveguide mesh MZI devices were independently tuned in power splitting ratio and overall phase shift by means of current injection to the heaters deposited on top of the waveguides implementing the interferometer arms. Despite the simplicity of the layout depicted in Figure 61, the 7-cell structure can implement over 100 different circuits. For MWP filtering applications basic MZI, FIR transversal filters, basic tunable ring cavities and IIR filters, as well as compound structures such as CROWS and side-coupled integrated spaced sequence of resonators (SCISSORS) are of particular interest. In [227], a different configuration featuring a wide variety of FSR values was reported. Figure 61 shows, for instance, 5 examples of microwave photonic FIR and IIR filters synthesized with the same hardware just by changing the operation state point of the different MZI elements in the mesh.

Another application of interest in microwave photonics is true-time delay lines as these are the basic building blocks of key functionalities, including arbitrary waveform generation and optical beamforming. The hexagonal waveguide mesh core can implement both dispersive as well as discrete time programmable true-time delay lines [228].

Waveguide mesh MWP universal processors. The incorporation of the waveguide mesh structure in the MWP processor core enables a more versatile processor architecture, which is the one we propose for future development. In this architecture, which we show in Figure 62, all the subsystems are directly connected to the reconfigurable optical core. This architecture is the first proposal for a generic-purpose software-defined MWP processor that incorporates the possibility of modifying the control signal flow to reconfigure the processing and interconnecting subsystems as required. It supports four different modes of operation as far as the input/output signals are concerned: electrical/electrical, electrical/optical, optical/electrical, and optical/optical operations.

Electrical/electrical operations are typically employed in MWP functionalities such as RF-filtering, instantaneous frequency measurement, frequency mixing, RF and millimeter-wave arbitrary signal generation to cite a few. It requires the processor to enable an optical source, electro-optic (EO) and optoelectronic (OE) converters as well as the reconfigurable optical core. Figures 62(a)–(d) illustrate the signal flows for these operations. Note that if a second modulator is integrated, it can be enabled to
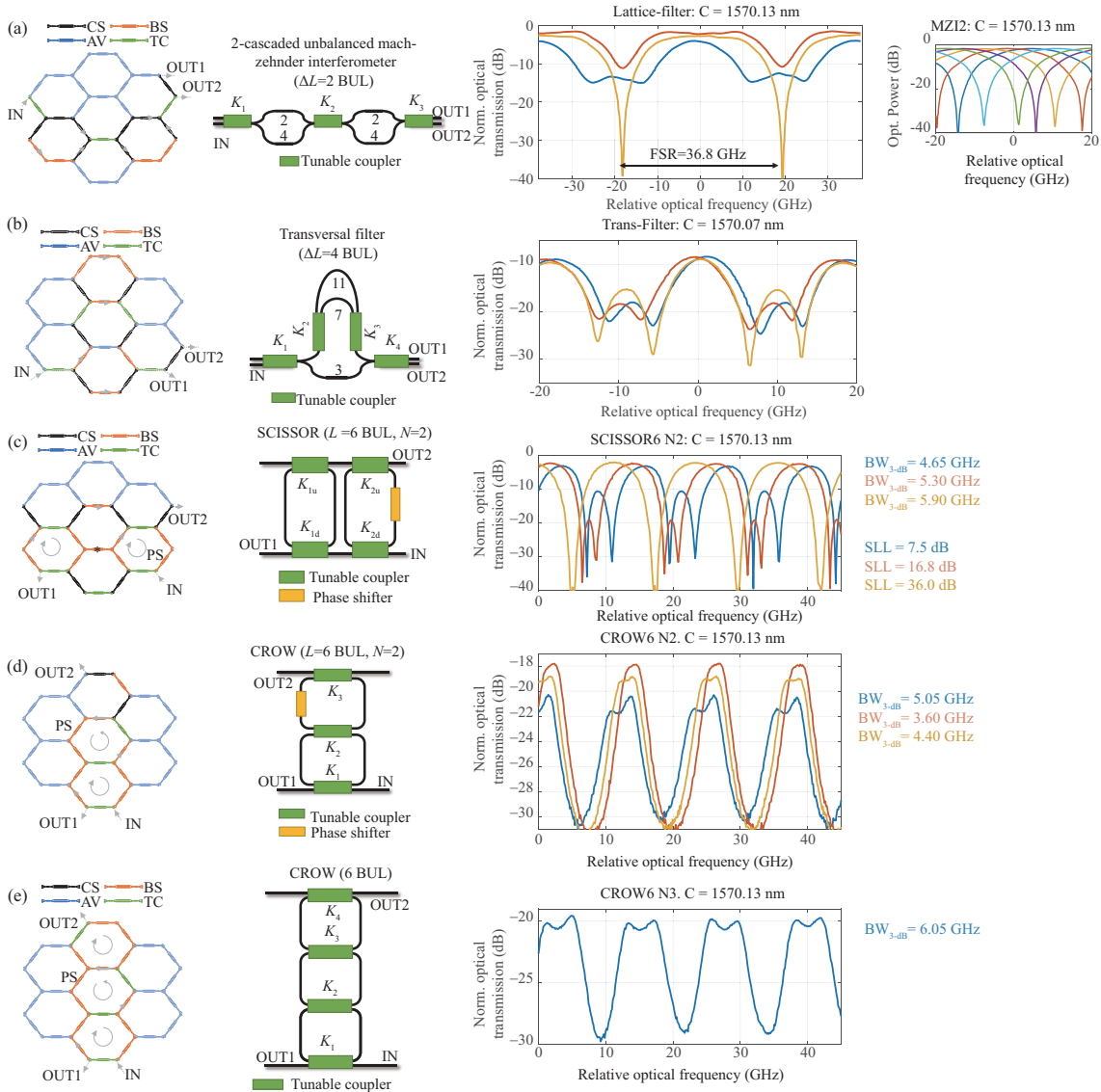
Figure 61 (Color online) Five examples of synthesized RF-photonic filters using the same 7-cell hexagonal mesh. In each case, the left part shows the TBU settings in the mesh. The intermediate part shows the circuit layout and the right part shows the measured results for the RF transfer function modules. (a) Two-cascaded unbalanced 2-MZI FIR filter; (b) three-tap transversal FIR filter; (c) two-cavity SCISSOR FIR filter; (d) two-cavity CROW filter; (e) three-cavity CROW Filter. MZI programming code: CS: cross state switch; BS: bar state switch; TC: tunable coupler; and AV: available (unused) [**227**].

perform frequency mixing operations based on the cascade of two EO modulators.

Sometimes, the processed signal has to be distributed over a particular fiber link length after generation and/or processing. The processor can leverage the inherent properties of optical fibers for distribution purposes. The electrical/optical mode is widely employed in radio-over-fiber MWPLs. At the receiver point of the link, another multipurpose MWP processor can be employed. In this case, the receiver would be working in optical/electrical mode, processing the signal before the photo-detection. Optionally, the receiver can enable its own optical source to act as a local oscillator as well. Both modes of operation are displayed in Figures 62(b) and (c), respectively.

The last mode of operation, illustrated in Figure 62(d), is the optical input/optical output. In this case, the input signal can be processed directly in the optical domain. Optical channel management can then perform common optical processing operations such as add/drop, switching, and broadcasting. Note that all the previous modes of operation may coexist for certain multi-task functionality. For example, a modulated signal could be divided after being processed and both distributed through the optical ports and down-converted by the photodetectors.

We have shown that the hexagonal waveguide core is the best candidate to perform the reconfigurable
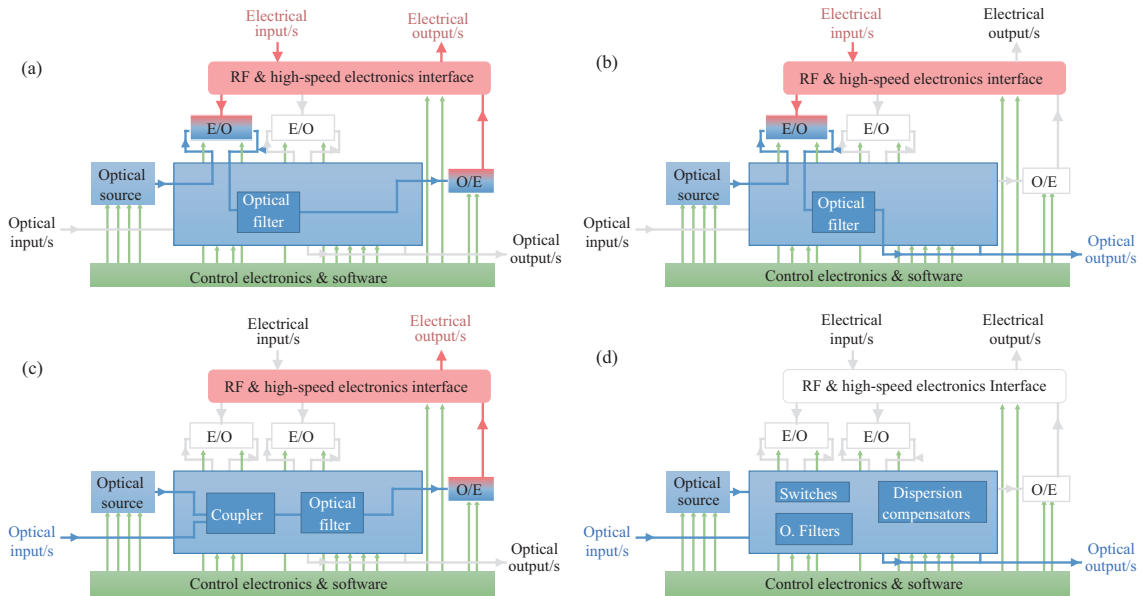
Figure 62 (Color online) Generic purpose MWP processor architecture programmed different modes of operation. (a) Electrical/electrical, (b) electrical/optical, (c) optical/electrical and (d) optical/optical [228].

optical core task: featuring subsystems interconnection as well as enabling versatile optical processing operations. By suitable programming each element on the processor, including the reconfigurable optical core, the same hardware can be configured to perform all the main functionalities required in MWP, as we illustrate in Figures 63 and 64.

True-time delay lines TTDs. Discretely and continuously tunable DLs [229, 230] can be supported by the MWP processor. Figure 63(a) illustrates, for example, the processor settings for the implementation of a discrete true-time delay based on the SCT approach [231]. Note that four optical ring resonators need to be enabled for the carrier tuning and optical delay line sections, as well as a double-loaded MZI for the implementation of the optical single side-band filter.

Filtering applications. The same hardware can be programmed as well to perform versatile RF-photonic tunable filtering. Here, the spectral characteristics of the optical filter implemented by the optical waveguide mesh core are directly translated into the RF spectrum by means of a self-beating homodyne technique, where part of the un-modulated optical carrier is sent separately and combined with the RF-modulated and optically filtered prior to photodetection, as illustrated in Figure 63(b) [231]. In this example, the synthesized RF filter is implemented by means of 6 cascaded optical ring resonators.

Microwave and mm-wave tone generation. This functionality enables the photonic generation and distribution of high-frequency RF signals, [232]. Among the different approaches reported, we illustrate here the implementation of two. Figure 63(c) depicts the programmable processor employing the external modulator with different modulation biasing points together with an optical filter to suppress the optical carrier and the undesired (odd or even) modes. The filter is implemented here with a fourth-order lattice of MZIs. The second approach consists of programming an optoelectronic oscillator [46] by closing the feedback loop of the RF section, as shown in Figure 63(d). In this example, the reconfigurable optical core implements a High-Q optical storage section with seven optical ring resonators.

Arbitrary waveform generation. Wavelength-to-time mapping is a promising solution and can be integrated on a chip. A broadband optical source is filtered by a spectral shaper. The spectral shape can be translated to the time domain by a dispersive element. Figure 64(a) illustrates the processor settings to configure the spectral shaper by means of five cascaded optical ring resonators [175], and a dispersive element implemented by a fourth-order lattice filter [232]. Note that versatility is the most valuable property of the spectral shaper, and the hexagonal waveguide processor core suits perfectly for this task, as demonstrated. Higher dispersive delays might be required and could be obtained by employing the optical ports for the connection of dispersive fiber reels.

Beamforming networks. The use of tunable delay lines allows a stable pointing angle independent of the transmitted frequency, enabling broadband operation. Figure 64(b) illustrates the implementation of a beamformer based on the natural discrete delay lines of the hexagonal core. By modifying the length of
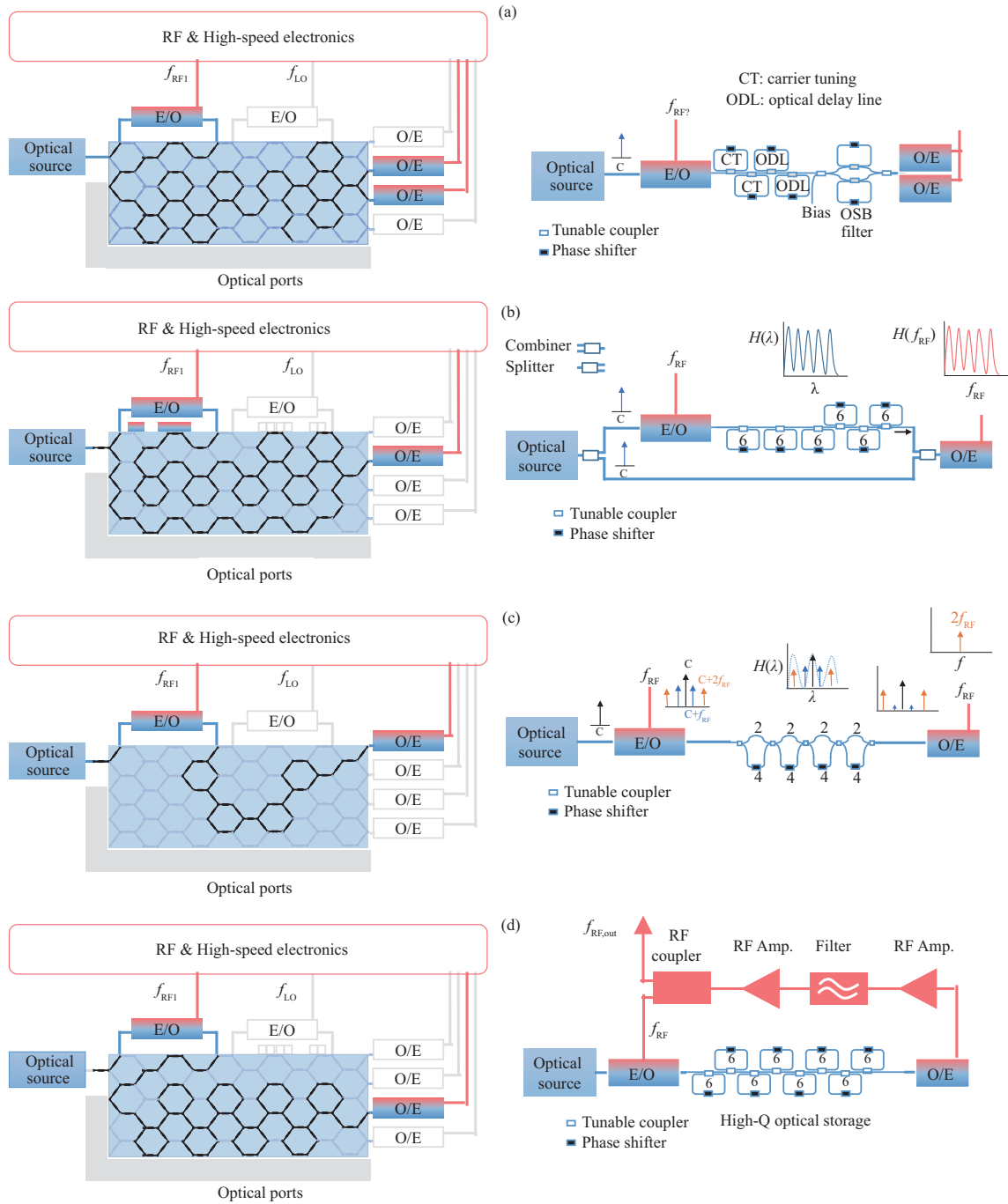
Figure 63 (Color online) (Left) Examples of MWP processor settings for the implementation of different MWP functionalities. For each functionality the circuit schemes are shown on the right hand side: (a) true time delay line employing the single carrier tuning (SCT) technique, (b) self-homodyne filter FIR, microwave and mm-wave tones generation based on (c) external modulation, and (d) optoelectronic oscillatio [228].

the paths, the differential delay can be changed. The tilt angle tuning will be limited to discrete values in the range of $[-\pi, \pi]$.

Instantaneous frequency measurement. These systems are employed to measure the frequency of microwave signals in real-time applications. Figure 64(c) depicts one of the approaches that consist in mapping the unknown microwave frequency to an optical power ratio by establishing a unique relationship, commonly referred to as the amplitude comparison function (ACF), that is independent of both the laser and input RF powers. The ACF can be performed by a 2×2 complementary filter [233]. In this case, the filter is implemented by means of 2 cascaded balanced MZIs loaded with a total of 4 optical ring
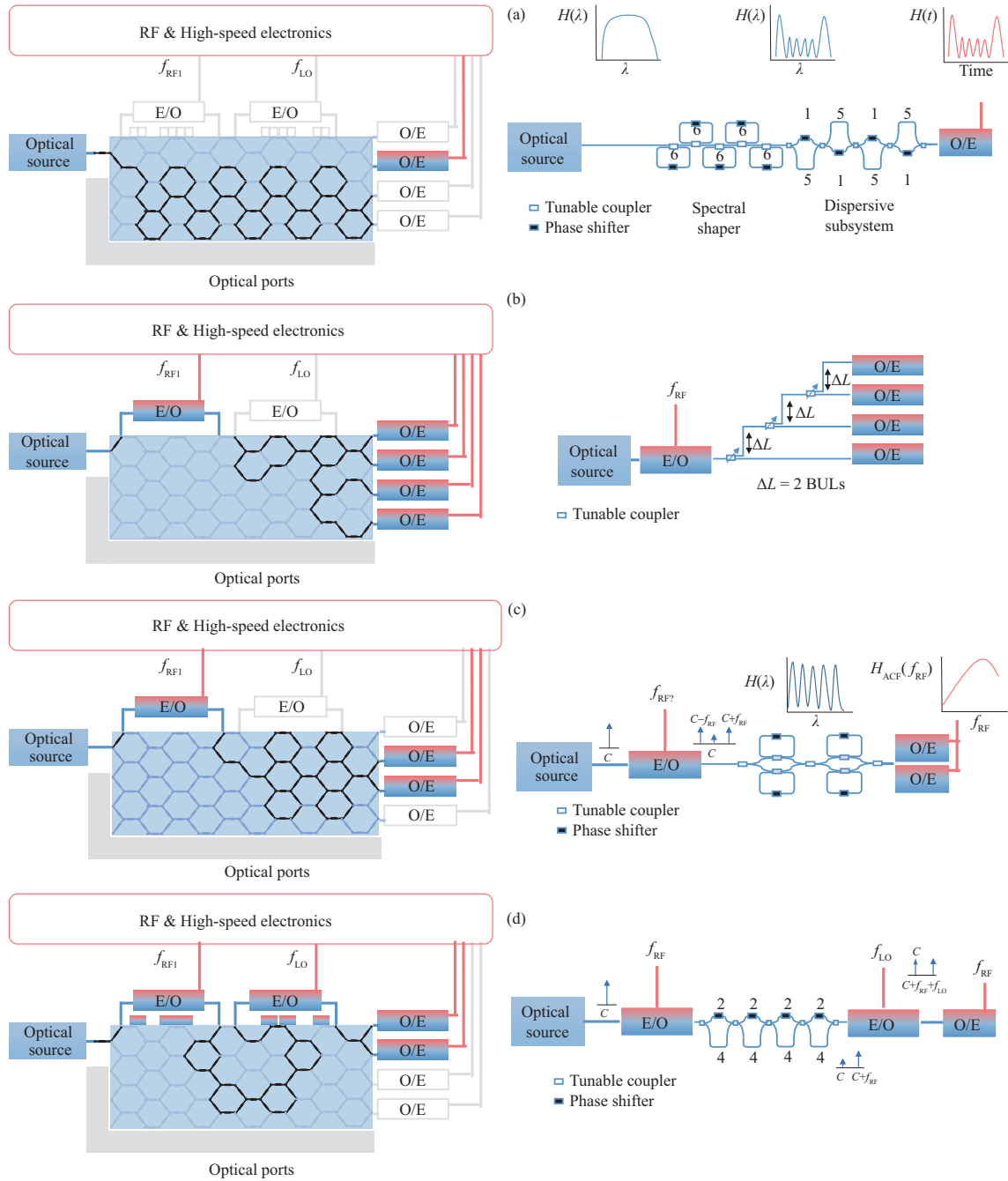
Figure 64 (Color online) (Left) General-purpose photonic processor settings for the implementation of a particular MWP scheme (right): (a) arbitrary waveform generation based on wavelength-to-time mapping, (b) beamforming networks based on true time delay, (c) instantaneous frequency measurement, and (d) RF-mixing based on 2 cascaded modulators [228].

resonators. Sharper filter functions lead to an increase in the resolution at the expense of reducing the frequency range. A key advantage of the reconfigurable processor is that the ACF can be made reconfigurable, so multiple measurements can be done while reconfiguring an ACF for each frequency range of measurement.

Frequency mixing. Frequency up-and/or down-conversion of RF signals is typically required in many radio-over-fiber and intermediate-frequency-over-fiber systems [234]. Figure 64(d) illustrates the processor configuration to achieve this functionality, where an optional optical filter, this time implemented by a fourth-order lattice filter, is employed to suppress the possible intermodulation contributions prior to the second modulator input.

For some of the previous functionalities, the integration of an optical amplifier subsystem or an optical
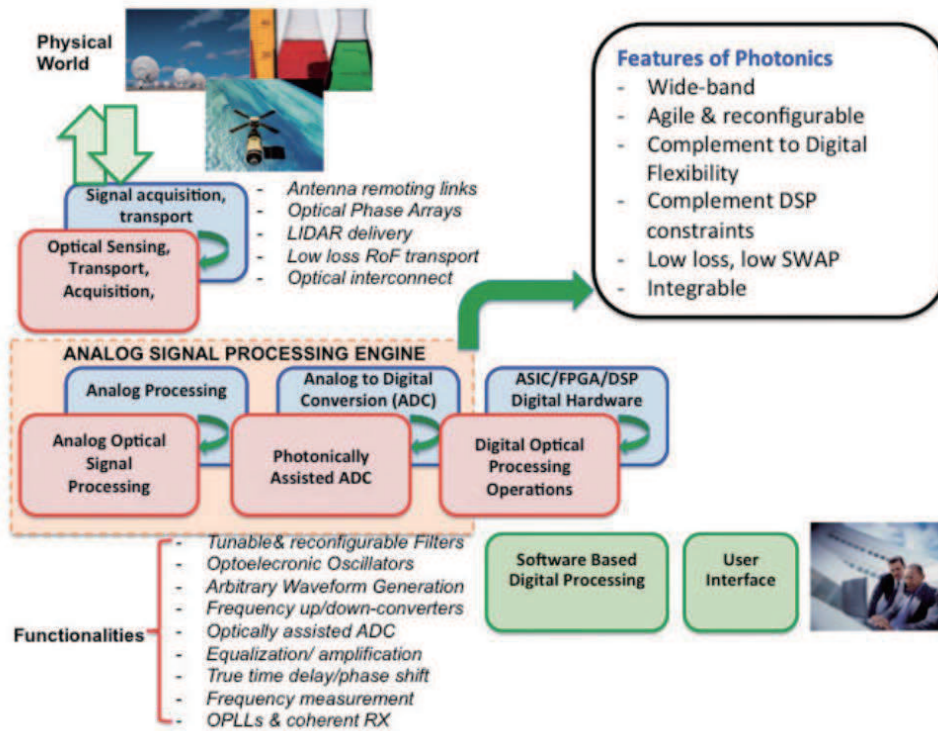
Figure 65 (Color online) Analog signal processing engine in the context of ICT systems. This concept is transversal and enables different applications for microwave photonics systems.

amplifier array prior to photodetection would be required to overcome the electrooptic and optoelectronic conversion losses.

The key challenge in implementing a microwave photonic signal processor is the relatively high loss, which would limit the scale of the photonic signal processor and would make it not ready to replace a state-of-the-art electronic signal processor. However, with the fast advances in PIC technology, especially the maturity of the heterogeneous integration techniques, a PIC that incorporates both photonic and electronic (including both analog and digital) devices would outperform the current electronic-only signal processors and would find practical applications in communications and radar systems.

7 Applications

Microwave photonics technology found initial niche applications mainly in security and defense systems [4]. However, with information and communication technology (ICT) systems expanding at an awesome pace in terms of capacity demand, the number of connected end-users, and required infrastructure, it has become evident that there is and will be in the forthcoming years a need for a flexible, scalable, and future-proof solution for seamlessly interfacing the wireless and photonic segments of communication networks. Microwave photonics with its inherent capability of interfacing these highly dissimilar media is the best positioned technology to provide a flexible, adaptive, and future-proof physical layer with unmatched characteristics by enabling the realization of key functionalities in microwave systems, which are either complex or even not directly possible within the RF domain.

As shown in Figure 65, microwave photonics systems are usually envisioned at the heart of analog signal processing engines, placed in between the signal acquisition devices and front-end digital signal processors (DSPs) to accommodate the signal formats with the constraints imposed by the DSP-limited sampling rates.

By realizing the wide variety of functionalities that we have previously described, MWP systems are expected to span dramatically their areas of application embracing civil applications with the expected massive takeover. Some examples shown in Figure 66 include the following.

(i) 5/6G communications where MWP filtering, Radio over fiber communications and beamforming

Figure 66 (Color online) Different application scenarios for microwave photonic systems in emerging fields (courtesy of iPronics).

techniques will be extensively exploited.

(ii) Internet of Things (IoT) and Industry 4.0 where MWP signal generation, transmission and interfacing capabilities will enable the integration of man-to-man, man-to-machine and machine-to-machine communications and sensor data collection in mixed fiber-wireless scenarios.

(iii) Car-to-car communications and autonomous driving which will require advanced and flexible radar and lidar techniques based on advanced high frequency radio signal generation and beamforming,

(iv) Avionics and drone engineering which will require the integration of advanced, compact, and flexible RF signal generators, antenna beamformers, and broadband analog communications.

(v) High resolution sensing, molecular and bio spectroscopy, and imaging which will require the integration of advanced tunable optoelectronic oscillators, optical generation of THz waves with optical spectrum analyzers.

These emerging paradigms are currently on the increasing slope of their S development curve and are expected to push this pressure even further. The requirements demanded by most of these scenarios call for novel technology developments in both the physical layer and the network architectures. In particular, an evolution to higher frequencies is expected as 5/6G communications will target K (18–26.5 GHz), Ka (26.5–40 GHz), Q (30–50 GHz), and E (60–90 GHz) bands, radar at the W band (75–110 GHz) and new standards for WLAN at the V band (50–75 GHz). This will require a smaller footprint in the RF frontends and increased processing bandwidths possibly carried by application-specific microwave photonics chips in the first instance and programmable microwave photonics chips in a later stage as the multifunction operation will be required.

Another important application of microwave photonics is wideband and high-resolution radars. Thanks to the wide bandwidth offered by photonics, wideband microwave waveforms can be generated based on photonics, which would help increase the resolution of a radar system. The first demonstration of a microwave photonic radar was in 2014 [235] in which a mode locked laser was employed to generate a high frequency microwave signal for transmission, and at the same time, mode locked laser was used as a high repetition rate pulse train for high-speed sampling for receiver signal processing. Since then, a great number of studies have been published to report different architectures of radar systems implemented based on microwave photonics [236].

8 Discussion and conclusion

A comprehensive review of microwave photonics techniques with their implementation based on discrete components and photonic integrated circuits has been performed. Despite the great potential offered by microwave photonic subsystems and systems based on discrete components with unique features not offered by state-of-the-art electronics, their applications are still limited. Recent activities in high-speed modulators [237,238] and photodetectors [239,240] have made discrete component-based microwave photonic systems operate at much higher speed and wider bandwidth. However, the high manufacturing costs have made them mainly for some specific applications where the costs are not a major issue. The

activities in integrated photonics to integrate both active and passive photonic devices in a single photonic integrated chip have helped to realize integrated microwave photonics systems at significantly reduced cost with greatly improved performance. In this article, a detailed review of the recent progress in integrated microwave photonics was provided including the materials systems that are suitable for integrated microwave photonics, and two types of integrated microwave photonics systems, application-specific photonic integrated circuits, and general-purpose programmable microwave photonic signal processors, were provided.

We would like to emphasize that among the different materials systems, SOI has been considered a material system with the highest potential for integrated microwave photonics thanks to the key advantages including small footprint, low loss, and low fabrication cost by using the well-developed and mature CMOS fabrication technology. Both active and passive photonic components can be realized in Si-based chips except for light sources and optical amplifiers. For microwave photonics applications, light sources are always needed. In most of the demonstrations reported in the literature, an external light source was employed, which makes the systems complicated and costly. In addition, due to fiber-to-chip and chip-to-fiber coupling being needed, the system loss is high. To solve these problems, heterogeneous integration should be implemented by jointly using Si and InP, with light sources and optical amplifiers implemented based on InP/Si and all other photonic components based on Si, to make monolithically integrated microwave photonics subsystems and systems to have a compact size, low loss, and better stability.

References

1 Yao J. Microwave photonics. J Lightw Technol, 2009, 27: 314–335
2 Capmany J, Novak D. Microwave photonics combines two worlds. Nat Photon, 2007, 1: 319–330
3 Seeds A J, Williams K J. Microwave photonics. J Lightwave Technol, 2006, 24: 4628–4641
4 Berceli T, Herczfeld P R. Microwave photonics—a historical perspective. IEEE Trans Microwave Theor Techn, 2010, 58: 2992–3000
5 Cox III C H. Analog Photonic Links: Theory and Practice. Cambridge: Cambridge University Press, 2004
6 Chang W S C. RF Photonic Technology in Optical Fiber Links. Cambridge: Cambridge University Press, 2007
7 Iezekiel S. Microwave Photonics. Hoboken: John Wiley & Sons, 2009
8 Vilcot A, Cabon B, Chazelas J. Microwave-Photonics: From Components to Applications and Systems. Berlin: Springer, 2003
9 Rumerhald C, Algani C, Billabert A L. Microwaves Photonic Links: Components and Circuits. Hoboken: John Wiley & Sons, 2013
10 Cox C H, Ackerman E I, Betts G E, et al. Limits on the performance of RF-over-fiber links and their impact on device design. IEEE Trans Microwave Theor Techn, 2006, 54: 906–920
11 Roussell H V, Regan M D, Prince J L, et al. Gain, noise figure and bandwidth-limited dynamic range of a low-biased external modulation link. In: Proceedings of Interntional Topical Meeting on Microwave Photonics, Victoria, 2007. 84–87
12 Gasulla I, Capmany J. Analytical model and figures of merit for filtered microwave photonic links. Opt Express, 2011, 19: 19758–19774
13 Goldberg L, Taylor H F, Weller J F, et al. Microwave signal generation with injection-locked laser diodes. Electron Lett, 1983, 19: 491–493
14 Goldberg L, Yurek A, Taylor H F, et al. 35 GHz microwave signal generation with injection locked laser diode. Electron Lett, 1985, 21: 714–715
15 Bouyer P, Gustavson T L, Haritos K G, et al. Microwave signal generation with optical injection locking. Opt Lett, 1996, 21: 1502–1504
16 Cui W, Shao T, Yao J. Wavelength reuse in a UWB over WDM-PON based on injection locking of a Fabry-Pérot laser diode and polarization multiplexing. J Lightwave Technol, 2014, 32: 220–227
17 Pan S, Tang Z, Zhu D, et al. Injection-locked fiber laser for tunable millimeter-wave generation. Opt Lett, 2011, 36: 4722–4724
18 Pan S, Yao J. Wideband and frequency-tunable microwave generation using an optoelectronic oscillator incorporating a Fabry-Perot laser diode with external optical injection. Opt Lett, 2010, 35: 1911–1913
19 Harrison J, Mooradian A. Linewidth and offset frequency locking of external cavity GaAlAs lasers. IEEE J Quantum Electron, 1989, 25: 1252–1255
20 Ramos R T, Seeds A J. Fast heterodyne optical phase-lock loop using double quantum well laser diodes. Electron Lett, 1992, 28: 82–83
21 Gliese U, Nielsen T N, Bruun M, et al. A wideband heterodyne optical phase-locked loop for generation of 3–18 GHz microwave carriers. IEEE Photon Technol Lett, 1992, 4: 936–938
22 Bordonalli A C, Walton C, Seeds A J. High-performance phase locking of wide linewidth semiconductor lasers by combined use of optical injection locking and optical phase-lock loop. J Lightwave Technol, 1999, 17: 328–342
23 Fan F Z, Dagenais M. Optical generation of a megahertz-linewidth microwave signal using semiconductor lasers and a discriminator-aided phase-locked loop. IEEE Trans Microwave Theor Techn, 1997, 45: 1296–1300
24 Rideout H R, Seregelyi J S, Paquet S, et al. Discriminator-aided optical phase-lock loop incorporating a frequency down-conversion module. IEEE Photon Technol Lett, 2006, 18: 2344–2346
25 Rideout H R, Seregelyi J S, Yao J. A true time delay beamforming system incorporating a wavelength tunable optical phase-lock loop. J Lightwave Technol, 2007, 25: 1761–1770
26 Balakier K, Ponnampalam L, Fice M J, et al. Integrated semiconductor laser optical phase lock loops. IEEE J Sel Top Quantum Electron, 2018, 24: 1500112
27 Balakier K, Shams H, Fice M J, et al. Optical phase lock loop as high-quality tuneable filter for optical frequency comb line selection. J Lightwave Technol, 2018, 36: 4646–4654
28 O'Reilly J J, Lane P M, Heidemann R, et al. Optical generation of very narrow linewidth millimetre wave signals. Electron Lett, 1992, 28: 2309–2311

29 O'Reilly J J, Lane P M. Remote delivery of video services using mm-waves and optics. J Lightwave Technol, 1994, 12: 369–375

30 O'Reilly J J, Lane P M. Fibre-supported optical generation and delivery of 60 GHz signals. Electron Lett, 1994, 30: 1329–1330

31 Qi G H, Yao J P, Seregelyi J, et al. Generation and distribution of a wide-band continuously tunable millimeter-wave signal with an optical external modulation technique. IEEE Trans Microwave Theor Techn, 2005, 53: 3090–3097

32 Qi G H, Yao J P, Seregelyi J, et al. Optical generation and distribution of continuously tunable millimeter-wave signals using an optical phase modulator. J Lightwave Technol, 2005, 23: 2687–2695

33 Qasymeh M, Li W, Yao J. Frequency-tunable microwave generation based on time-delayed optical combs. IEEE Trans Microwave Theor Techn, 2011, 59: 2987–2993

34 Li W, Yao J. Investigation of photonically assisted microwave frequency multiplication based on external modulation. IEEE Trans Microwave Theor Techn, 2010, 58: 3259–3268

35 Pan S L, Yao J P. Tunable subterahertz wave generation based on photonic frequency sextupling using a polarization modulator and a wavelength-fixed notch filter. IEEE Trans Microwave Theor Techn, 2010, 58: 1967–1975

36 Liu W L, Wang M G, Yao J P. Tunable microwave and sub-terahertz generation based on frequency quadrupling using a single polarization modulator. J Lightwave Technol, 2013, 31: 1636–1644

37 Qi G, Yao J, Seregelyi J, et al. Phase-noise analysis of optically generated millimeter-wave signals with external optical modulation techniques. J Lightwave Technol, 2006, 24: 4861–4875

38 Robins W P. Phase Noise in Signal Sources: Theory and Applications. London: The Institution of Engineering and Technology, 1984. 77

39 Fortier T M, Kirchner M S, Quinlan F, et al. Generation of ultrastable microwaves via optical frequency division. Nat Photon, 2011, 5: 425–429

40 Yao X S, Maleki L. Optoelectronic microwave oscillator. J Opt Soc Am B, 1996, 13: 1725–1735

41 Yao X S, Maleki L. Optoelectronic oscillator for photonic systems. IEEE J Quantum Electron, 1996, 32: 1141–1149

42 Yao X S, Maleki L. Multiloop optoelectronic oscillator. IEEE J Quantum Electron, 2000, 36: 79–84

43 Ozdur I, Mandridis D, Hoghooghi N, et al. Low noise optically tunable optoelectronic oscillator with Fabry-Perot etalon. J Lightw Technol, 2010, 28: 3100–3106

44 Pan S, Yao J. Wideband and frequency-tunable microwave generation using an optoelectronic oscillator incorporating a Fabry-Perot laser diode with external optical injection. Opt Lett, 2010, 35: 1911–1913

45 Li W, Yao J. An optically tunable optoelectronic oscillator. J Lightwave Technol, 2010, 28: 2640–2645

46 Li W, Yao J. A wideband frequency tunable optoelectronic oscillator incorporating a tunable microwave photonic filter based on phase-modulation to intensity-modulation conversion using a phase-shifted fiber Bragg grating. IEEE Trans Microwave Theor Techn, 2012, 60: 1735–1742

47 Maleki L. The optoelectronic oscillator. Nature Photon, 2011, 5: 728–730

48 Zhang J, Yao J. Parity-time-symmetric optoelectronic oscillator. Sci Adv, 2018, 4: eaar6782

49 Liu Y, Hao T, Li W, et al. Observation of parity-time symmetry in microwave photonics. Light Sci Appl, 2018, 7: 38

50 Bender C M, Boettcher S. Real spectra in non-Hermitian Hamiltonians having PT symmetry. Phys Rev Lett, 1998, 80: 5243–5246

51 Bender C M. Making sense of non-Hermitian Hamiltonians. Rep Prog Phys, 2007, 70: 947–1018

52 Feng L, El-Ganainy R, Ge L. Non-Hermitian photonics based on parity-time symmetry. Nat Photon, 2017, 11: 752–762

53 El-Ganainy R, Makris K G, Khajavikhan M, et al. Non-Hermitian physics and PT symmetry. Nat Phys, 2018, 14: 11–19

54 Qi B, Chen H Z, Ge L, et al. Parity-time symmetry synthetic lasers: physics and devices. Adv Opt Mater, 2019, 7: 1900694

55 Hodaei H, Miri M A, Heinrich M, et al. Parity-time-symmetric microring lasers. Science, 2014, 346: 975–978

56 Feng L, Wong Z J, Ma R M, et al. Single-mode laser by parity-time symmetry breaking. Science, 2014, 346: 972–975

57 Hodaei H, Miri M A, Hassan A U, et al. Parity-time-symmetric coupled microring lasers operating around an exceptional point. Opt Lett, 2015, 40: 4955–4958

58 Hodaei H, Miri M A, Hassan A U, et al. Single mode lasing in transversely multi-moded PT-symmetric microring resonators. Laser Photon Rev, 2016, 10: 494–499

59 Liu W, Li M, Guzzon R S, et al. A photonic integrated parity-time symmetry wavelength-tunable single-mode microring laser. Nat Commun, 2017, 10: 15389

60 Fan Z, Zhang W, Qiu Q, et al. Hybrid frequency-tunable parity-time symmetric optoelectronic oscillator. J Lightwave Technol, 2020, 38: 2127–2133

61 Li P, Dai Z, Fan Z, et al. Parity-time-symmetric frequency-tunable optoelectronic oscillator with a single dual-polarization optical loop. Opt Lett, 2020, 45: 3139–3142

62 Dai Z, Fan Z Q, Li P, et al. Frequency-tunable parity-time-symmetric optoelectronic oscillator using a polarization-dependent Sagnac loop. J Lightw Technol, 2020, 38: 5327–5332

63 Fan Z Q, Dai Z, Qiu Q, et al. Parity-time symmetry in a single-loop photonic system. J Lightwave Technol, 2020, 38: 3866–3873

64 Chi H, Wang C, Yao J. Photonic generation of wideband chirped microwave waveforms. IEEE J Microw, 2021, 1: 787–803

65 Hao T, Cen Q, Dai Y, et al. Breaking the limitation of mode building time in an optoelectronic oscillator. Nat Commun, 2018, 9: 1839

66 Tang J, Zhu B, Zhang W, et al. Hybrid Fourier-domain mode-locked laser for ultra-wideband linearly chirped microwave waveform generation. Nat Commun, 2020, 11: 3814

67 Capmany J, Ortega B, Pastor D. A tutorial on microwave photonic filters. J Lightwave Technol, 2006, 24: 201–229

68 Minasian R A. Photonic signal processing of microwave signals. IEEE Trans Microwave Theor Techn, 2006, 54: 832–846

69 Yao J. Photonics to the rescue: a fresh look at microwave photonic filters. IEEE Microwave, 2015, 16: 46–60

70 Capmany J, Pastor D, Martinez A, et al. Microwave photonic filters with negative coefficients based on phase inversion in an electro-optic modulator. Opt Lett, 2003, 28: 1415–1417

71 Wang Q, Yao J. Multitap photonic microwave filters with arbitrary positive and negative coefficients using a polarization modulator and an optical polarizer. IEEE Photon Technol Lett, 2008, 20: 78–80

72 Yan Y, Blais S R, Yao J P. Tunable photonic microwave bandpass filter with negative coefficients implemented using an optical phase modulator and chirped fiber Bragg gratings. J Lightwave Technol, 2007, 25: 3283–3288

73 Yan Y, Yao J. A tunable photonic microwave filter with a complex coefficient using an optical RF phase shifter. IEEE Photon Technol Lett, 2007, 19: 1472–1474

74 Shahoei H, Yao J. A continuously tunable multi-tap complex-coefficient microwave photonic filter based on a tilted fiber Bragg grating. Opt Express, 2013, 21: 7521–7527

75 Dai Y, Yao J. Nonuniformly spaced photonic microwave delay-line filters and applications. IEEE Trans Microwave Theor Techn, 2010, 58: 3279–3289

76 Yi X, Minasian R A. Microwave photonic filter with single bandpass response. Electron Lett, 2009, 45: 362–363

77 Palaci J, Villanueva G E, Galan J V, et al. Single bandpass photonic microwave filter based on a notch ring resonator. IEEE Photon Technol Lett, 2010, 22: 1276–1278

78 Marpaung D, Morrison B, Pant R, et al. Frequency agile microwave photonic notch filter with anomalously high stopband rejection. Opt Lett, 2013, 38: 4300–4303

79 Li W, Li M, Yao J. A narrow-passband and frequency-tunable microwave photonic filter based on phase-modulation to intensity-modulation conversion using a phase-shifted fiber Bragg grating. IEEE Trans Microwave Theor Techn, 2012, 60: 1287–1296

80 Erdogan T. Fiber grating spectra. J Lightwave Technol, 1997, 15: 1277–1294

81 Gao L, Chen X, Yao J. Tunable microwave photonic filter with a narrow and flat-top passband. IEEE Microw Wireless Compon Lett, 2013, 23: 362–364

82 Dai Y, Chen X, Jiang D, et al. Equivalent phase shift in a fiber Bragg grating achieved by changing the sampling period. IEEE Photon Technol Lett, 2004, 16: 2284–2286

83 Gao L, Zhang J, Chen X, et al. Microwave photonic filter with two independently tunable passbands using a phase modulator and an equivalent phase-shifted fiber Bragg grating. IEEE Trans Microwave Theor Techn, 2014, 62: 380–387

84 Yan Y, Yao J. Photonic microwave bandpass filter with improved dynamic range. Opt Lett, 2008, 33: 1756–1758

85 Li W, Yao J. A narrow-passband frequency-tunable microwave photonic filter with an improved dynamic range. In: Proceedings of Optical Fiber Communication Conference and Exposition and the National Fiber Optic Engineers Conference, Anaheim, 2013. 1–3

86 Chen X, Li W, Yao J. Microwave photonic link with improved dynamic range using a polarization modulator. IEEE Photon Technol Lett, 2013, 25: 1373–1376

87 Han X, Xu E, Yao J. Tunable single bandpass microwave photonic filter with an improved dynamic range. IEEE Photon Technol Lett, 2016, 28: 11–14

88 Yao J. Photonic generation of microwave arbitrary waveforms. Optics Commun, 2011, 284: 3723–3736

89 Leaird D E, Weiner A M. Femtosecond opticalpacket generation by a direct space-to-time pulse shaper. Opt Lett, 1999, 24: 853–855

90 Leaird D E, Weiner A M. Femtosecond direct space-to-time pulse shaping. IEEE J Quantum Electron, 2001, 37: 494–504

91 Leaird D E, Weiner A M. Chirp control in the direct space-to-time pulse shaper. Opt Lett, 2000, 25: 850–852

92 McKinney J D, Leaird D E, Weiner A M. Millimeter-wave arbitrary waveform generation with a direct space-to-time pulse shaper. Opt Lett, 2002, 27: 1345–1347

93 McKinney J D, Seo D S, Weiner A M. Photonically assisted generation of continuous arbitrary millimetre electromagnetic waveforms. Electron Lett, 2003, 39: 309–310

94 McKinney J D, Seo J D, Leaird D E, et al. Photonically assisted generation of arbitrary millimeter-wave and microwave electromagnetic waveforms via direct space-to-time optical pulse shaping. J Lightwave Technol, 2003, 21: 3020–3028

95 Xiao S, McKinney J D, Weiner A M. Photonic microwave arbitrary waveform generation using a virtually imaged phased-array (VIPA) direct space-to-time pulse shaper. IEEE Photon Technol Lett, 2004, 16: 1936–1938

96 Leaird D E, Weiner A M. Femtosecond direct space-to-time pulse shaping in an integrated-optic configuration. Opt Lett, 2004, 29: 1551–1553

97 Wang C, Yao J P. Chirped microwave pulse generation based on optical spectral shaping and wavelength-to-time mapping using a Sagnac loop mirror incorporating a chirped fiber Bragg grating. J Lightwave Technol, 2009, 27: 3336–3341

98 Wang C, Yao J P. Simultaneous optical spectral shaping and wavelength-to-time mapping for photonic microwave arbitrary waveform generation. IEEE Photon Technol Lett, 2009, 21: 793–795

99 Yao J. Microwave photonics: arbitrary waveform generation. Nat Photon, 2010, 4: 79–80

100 Wang C, Yao J P. Large time-bandwidth product microwave arbitrary waveform generation using a spatially discrete chirped fiber Bragg grating. J Lightwave Technol, 2010, 28: 1652–1660

101 Chi H, Yao J P. Chirped RF pulse generation based on optical spectral shaping and wavelength-to-time mapping using a nonlinearly chirped fiber Bragg grating. J Lightwave Technol, 2008, 26: 1282–1287

102 Wang C, Yao J. Photonic generation of chirped millimeter-wave pulses based on nonlinear frequency-to-time mapping in a nonlinearly chirped fiber Bragg grating. IEEE Trans Microwave Theor Techn, 2008, 56: 542–553

103 Azaña J, Berger N K, Levit B, et al. Reconfigurable generation of high-repetition-rate optical pulse sequences based on time-domain phase-only filtering. Opt Lett, 2005, 30: 3228–3230

104 Chi H, Yao J. Symmetrical waveform generation based on temporal pulse shaping using amplitude-only modulator. Electron Lett, 2007, 43: 415–417

105 Wang C, Li M, Yao J. Continuously tunable photonic microwave frequency multiplication by use of an unbalanced temporal pulse shaping system. IEEE Photon Technol Lett, 2010, 22: 1285–1287

106 Li M, Wang C, Li W, et al. An unbalanced temporal pulse-shaping system for chirped microwave waveform generation. IEEE Trans Microwave Theor Techn, 2010, 58: 2968–2975

107 Dolfi D, Michel-Gabriel F, Bann S, et al. Two-dimensional optical architecture for time-delay beam forming in a phased-array antenna. Opt Lett, 1991, 16: 255–257

108 Dolfi D, Joffre P, Antoine J, et al. Experimental demonstration of a phased-array antenna optically controlled with phase and time delays. Appl Opt, 1996, 35: 5293–5300

109 Ng W, Walston A A, Tangonan G L, et al. The first demonstration of an optically steered microwave phased array antenna using true-time-delay. J Lightwave Technol, 1991, 9: 1124–1131

110 Esman R D, Monsma M J, Dexter J L, et al. Microwave true time-delay modulator using fibre-optic dispersion. Electron Lett, 1992, 28: 1905

111 Esman R D, Frankel M Y, Dexter J L, et al. Fiber-optic prism true time-delay antenna feed. IEEE Photon Technol Lett, 1993, 5: 1347–1349

112 Molony A, Lin Z, Williams J A R, et al. Fiber Bragg-grating true time-delay systems: discrete-grating array 3-b delay lines and chirped-grating 6-b delay lines. IEEE Trans Microwave Theor Techn, 1997, 45: 1527–1530

113 Corral J L, Marti J, Fuster J M, et al. True time-delay scheme for feeding optically controlled phased-array antennas using chirped-fiber gratings. IEEE Photon Technol Lett, 1997, 9: 1529–1531

114 Zmuda H, Soref R A, Payson P, et al. Photonic beamformer for phased array antennas using a fiber grating prism. IEEE Photon Technol Lett, 1997, 9: 241–243

115 Minasian R A, Alameh K E. Optical-fiber grating-based beamforming network for microwave phased arrays. IEEE Trans Microwave Theor Techn, 1997, 45: 1513–1518

116 Matthews P J, Frankel M Y, Esman R D. A wide-band fiber-optic true-time-steered array receiver capable of multiple independent simultaneous beams. IEEE Photon Technol Lett, 1998, 10: 722–724

117 Tong D T K, Wu M C. Multiwavelength optically controlled phased-array antennas. IEEE Trans Microwave Theor Techn,

1998, 46: 108–115

118   Tong D T K, Wu M C. Common transmit/receive module for multiwavelength optically controlled phased array antennas. In: Proceedings of Optical Fiber Communication Conference and Exhibit, 1998. 354–355

119   Yao J P, Yang J L, Liu Y Q. Continuous true-time-delay beamforming employing a multiwavelength tunable fiber laser source. IEEE Photon Technol Lett, 2002, 14: 687–689

120   Liu Y, Yao J, Yang J. Wideband true-time-delay unit for phased array beamforming using discrete-chirped fiber grating prism. Optics Commun, 2002, 207: 177–187

121   Vidal B, Madrid D, Corral J L, et al. Photonic true-time delay beamformer for broadband wireless access network at 40 GHz band. In: Proceedings of IEEE MTT-S International Microwave Symposium Digest, 2002. 3: 1949–1952

122   Liu Y Q, Yang J L, Yao J P. Continuous true-time-delay beamforming for phased array antenna using a tunable chirped fiber grating delay line. IEEE Photon Technol Lett, 2002, 14: 1172–1174

123   Chen Y H, Chen R T. A fully packaged true time delay module for a K-band phased array antenna system demonstration. IEEE Photon Technol Lett, 2002, 14: 1175–1177

124   Liu Y, Yao J, Yang J. Wideband true-time-delay beam former that employs a tunable chirped fiber grating prism. Appl Opt, 2003, 42: 2273–2277

125   Jung B M, Shin J D, Kim B G. Optical true time-delay for two-dimensional X-band phased array antennas. IEEE Photon Technol Lett, 2007, 19: 877–879

126   Blumenthal D J, Barton J, Beheshti N, et al. Integrated photonics for low-power packet networking. IEEE J Sel Top Quantum Electron, 2011, 17: 458–471

127   Marpaung D, Roeloffzen C, Heideman R, et al. Integrated microwave photonics. Laser Photon Rev, 2013, 7: 506–538

128   Iezekiel S, Burla M, Klamkin J, et al. RF engineering meets optoelectronics: progress in integrated microwave photonics. IEEE Microwave, 2015, 16: 28–45

129   Marpaung D, Yao J, Capmany J. Integrated microwave photonics. Nat Photon, 2019, 13: 80–90

130   Smit M, Leijtens X, Ambrosius H, et al. An introduction to InP-based generic integration technology. Semicond Sci Technol, 2014, 29: 083001

131   Coldren L A, Nicholes S C, Johansson L, et al. High performance InP-based photonic ICs—a tutorial. J Lightwave Technol, 2011, 29: 554–570

132   Kish F, Nagarajan R, Welch D, et al. From visible light-emitting diodes to large-scale III-V photonic integrated circuits. Proc IEEE, 2013, 101: 2255–2270

133   Hochberg M, Baehr-Jones T. Towards fabless silicon photonics. Nat Photon, 2010, 4: 492–494

134   Bogaerts W, Fiers M, Dumon P. Design challenges in silicon photonics. IEEE J Sel Top Quantum Electron, 2014, 20: 1–8

135   Soref R. The past, present, and future of silicon photonics. IEEE J Sel Top Quantum Electron, 2006, 12: 1678–1687

136   Chrostowski L, Hochberg M. Silicon Photonics Design: From Devices to Systems. Cambridge: Cambridge University Press, 2015

137   Heck M J R, Bauters J F, Davenport M L, et al. Hybrid silicon photonic integrated circuit technology. IEEE J Sel Top Quantum Electron, 2013, 19: 6100117

138   Keyvaninia S, Muneeb M, Stanković S, et al. Ultra-thin DVS-BCB adhesive bonding of III-V wafers, dies and multiple dies to a patterned silicon-on-insulator substrate. Opt Mater Express, 2013, 3: 35–46

139   Haq B, Kumari S, van Gasse K, et al. Micro-transfer-printed III-V-on-silicon C-band semiconductor optical amplifiers. Laser Photon Rev, 2020, 14: 1900364

140   Heideman R G, Hoekman M, Schreuder E. TriPleX$^{\mathrm{TM}}$-based integrated optical ring resonators for lab-on-a-chip and environmental detection. IEEE J Sel Top Quantum Electron, 2012, 18: 1583–1596

141   Roeloffzen C G H, Zhuang L, Taddei C, et al. Silicon nitride microwave photonic circuits. Opt Express, 2013, 21: 22937–22961

142   Corbett B, Loi R, Zhou W, et al. Transfer print techniques for heterogeneous integration of photonic components. Prog Quantum Electron, 2017, 52: 1–17

143   van der Tol J J G M, Jiao Y, Shen L, et al. Indium phosphide integrated photonics in membranes. IEEE J Sel Top Quantum Electron, 2018, 24: 1–9

144   Qi Y, Li Y. Integrated lithium niobate photonics. Nanophotonics, 2020, 9: 1287–1320

145   Nikogosyan D N. Nonlinear Optical Crystals: A Complete Survey. 1st ed. New York: Springer, 2005

146   Poberaj G, Koechlin M, Sulser F, et al. Ion-sliced lithium niobate thin films for active photonic devices. Optical Mater, 2009, 31: 1054–1058

147   Rabiei P, Gunter P. Optical and electro-optical properties of submicrometer lithium niobate slab waveguides prepared by crystal ion slicing and wafer bonding. Appl Phys Lett, 2004, 85: 4603–4605

148   Wu R, Wang M, Xu J, et al. Long low-loss-litium niobate on insulator waveguides with sub-nanometer surface roughness. Nanomaterials, 2018, 8: 910

149   Zhang M, Wang C, Cheng R, et al. Monolithic ultra-high-Q lithium niobate microring resonator. Optica, 2017, 4: 1536–1537

150   Muñoz P, Capmany J, Pérez D, et al. Integrated microwave photonics: state of the art and future trends. In: Proceedings of International Conference on Transparent Optical Networks (ICTON), Graz, 2014

151   Guzzon R S, Norberg E J, Parker J S, et al. Monolithically integrated programmable photonic microwave filter with tunable inter-ring coupling. In: Proceedings of IEEE International Topical Meeting on Microwave Photonics, Montreal, 2010. 23–26

152   Norberg E J, Guzzon R S, Parker J S, et al. A monolithic programmable optical filter for RF-signal processing. In: Proceedings of IEEE International Topical Meeting on Microwave Photonics, Montreal, 2010. 365–368

153   Norberg E J, Guzzon R S, Parker J S, et al. Programmable photonic filters from monolithically cascaded filter stages. In: Proceedings of Integrated Photonics Research, Silicon and Nanophotonics, Monterey, 2010

154   Norberg E J, Guzzon R S, Parker J S, et al. Programmable photonic microwave filters monolithically integrated in InP-InGaAsP. J Lightwave Technol, 2011, 29: 1611–1619

155   Guzzon R S, Norberg E J, Parker J S, et al. Integrated InP-InGaAsP tunable coupled ring optical bandpass filters with zero insertion loss. Opt Express, 2011, 19: 7816–7826

156   Chen H-W, Fang A W, Bovington J, et al. Hybrid silicon tunable filter based on a Mach–Zehnder interferometer and ring resonator. In: Proceedings of IEEE International Topical Meeting on Microwave Photonics, Valencia, 2009. 1–4

157   Chen H W, Fang A W, Peters J D, et al. Integrated microwave photonic filter on a hybrid silicon platform. IEEE Trans Microwave Theor Techn, 2010, 58: 3213–3219

158   Madsen C K, Zhao J H. Optical Filter Design and Analysis: A Signal Processing Approach. Hoboken: John Wiley & Sons, Inc. 1999

159   Dong P, Feng N N, Feng D, et al. GHz-bandwidth optical filters based on high-order silicon ring resonators. Opt Express, 2010, 18: 23784–23789

160   Feng N N, Dong P, Feng D, et al. Thermally-efficient reconfigurable narrowband RF-photonic filter. Opt Express, 2010, 18:

24648–24653

161 Romero-García S, Moscoso-Mártir A, Müller J, et al. Wideband multi-stage CROW filters with relaxed fabrication tolerances. Opt Express, 2018, 26: 4723–4737

162 Rasras M S, Tu K, Gill D M, et al. Demonstration of a tunable microwave-photonic notch filter using low-loss silicon ring resonators. J Lightwave Technol, 2009, 27: 2105–2110

163 Rasras M S, Gill D M, Patel S S, et al. Demonstration of a fourth-order pole-zero optical filter integrated using CMOS processes. J Lightwave Technol, 2007, 25: 87–92

164 Zhuang L. Flexible RF filter using a nonuniform SCISSOR. Opt Lett, 2016, 41: 1118

165 Zhuang L, Taddei C, Hoekman M, et al. Ring resonator-based on-chip modulation transformer for high-performance phase-modulated microwave photonic links. Opt Express, 2013, 21: 25999–26013

166 Zhuang L, Khan M R, Beeker W, et al. Novel microwave photonic fractional Hilbert transformer using a ring resonator-based optical all-pass filter. Opt Express, 2012, 20: 26499–26510

167 Taddei C, Yen N T H, Zhuang L M, et al. Waveguide filter-based on-chip differentiator for microwave photonic signal processing. In: Proceedings of IEEE International Topical Meeting on Microwave Photonics (MWP), Alexandria, 2013. 28–31

168 Zhuang L M, Hoekman M, Oldenbeuving R M, et al. CRIT-alternative narrow-passband waveguide filter for microwave photonic signal processors. IEEE Photon Technol Lett, 2014, 26: 1034–1037

169 Xie Y, Geng Z, Zhuang L, et al. Programmable optical processor chips: toward photonic RF filters with DSP-level flexibility and MHz-band selectivity. Nanophotonics, 2017, 7: 421–454

170 Orlandi P, Morichetti F, Strain M J, et al. Photonic integrated filter with widely tunable bandwidth. J Lightwave Technol, 2014, 32: 897–907

171 Fandiño J S, Muñoz P, Doménech D, et al. A monolithic integrated photonic microwave filter. Nat Photon, 2017, 11: 124–129

172 Zhang W, Yao J. Silicon photonic integrated optoelectronic oscillator for frequency-tunable microwave generation. J Lightwave Technol, 2018, 36: 4655–4663

173 Tang J, Hao T, Li W, et al. Integrated optoelectronic oscillator. Opt Express, 2018, 26: 12257–12265

174 Lin I S, McKinney J D, Weiner A M. Photonic synthesis of broadband microwave arbitrary waveforms applicable to ultra-wideband communication. IEEE Microw Wireless Compon Lett, 2005, 15: 226–228

175 Khan M H, Shen H, Xuan Y, et al. Ultrabroad-bandwidth arbitrary radiofrequency waveform generation with a silicon photonic chip-based spectral shaper. Nat Photon, 2010, 4: 117–122

176 Wang J, Shen H, Fan L, et al. Reconfigurable radio-frequency arbitrary waveforms synthesized in a silicon photonic chip. Nat Commun, 2015, 6: 5957

177 Zhang W, Zhang J, Yao J. Largely chirped microwave waveform generation using a silicon-based on-chip optical spectral shaper. In: Proceedings of IEEE Topical Meeting Microwave Photonics, Sapporo, 2014. 20–23

178 Zhang W, Yao J. Photonic generation of linearly chirped microwave waveform with a large time-bandwidth product using a silicon-based on-chip spectral shaper. In: Proceedings of International Topical Meeting on Microwave Photonics (MWP), Paphos, 2015. 26–29

179 Wu J, Xu X, Nguyen T G, et al. RF photonics: an optical microcombs' perspective. IEEE J Sel Top Quantum Electron, 2018, 24: 1–20

180 Wang Z, van Gasse K, Moskalenko V, et al. A III-V-on-Si ultra-dense comb laser. Light Sci Appl, 2017, 6: e16260

181 Wu R, Supradeepa V R, Long C M, et al. Generation of very flat optical frequency combs from continuous-wave lasers using cascaded intensity and phase modulators driven by tailored radio frequency waveforms. Opt Lett, 2010, 35: 3234

182 Chen Y, Wu K, Zhao F, et al. Loss compensated photonic true-time delay for phased-array antenna. IEEE Antenn Propag Soc Int Symp, 2004, 4: 4324–4327

183 Wang X, Howley B, Chen M Y, et al. Fully- integrated 4-bit true time delay module using polymer optical switches and waveguide delay lines. In: Proceedings of the Integrated Photonics Research Applications, 2006

184 Chen Y, Wu K, Zhao F, et al. Reconfigurable true-time delay for wideband phased-array antennas. In: Proceedings of SPIE, 2004. 5363: 125–130

185 Horikawa K, Ogawa I, Ogawa H, et al. Photonic switched true time delay beam forming network integrated on silica waveguide circuits. In: Proceedings of 1995 IEEE MTT-S International Microwave Symposium, Orlando, 1995. 65–68

186 Horikawa K, Ogawa I, Kitoh T, et al. Silica-based integrated planar lightwave true-time-delay network for microwave antenna applications. In: Proceedings of Optical Fiber Communications, 1996. 100–101

187 LeGrange J, Kasper A, Madsen C, et al. Demonstration of an integrated, tunable high resolution true time delay line. In: Proceedings of the 17th Annual Meeting IEEE Lasers Electro-Optics Society, 2004. 2: 790–791

188 Rasras M S, Madsen C K, Cappuzzo M A, et al. Integrated resonance-enhanced variable optical delay lines. IEEE Photon Technol Lett, 2005, 17: 834–836

189 Horikawa K, Nakasuga Y, Ogawa H. Self-heterodyning optical waveguide beam forming and steering network integrated on Lithium Niobate substrate. IEEE Trans Microwave Theor Techn, 1995, 43: 2395–2401

190 Ng W W, Yap D, Narayanan A A, et al. GaAs and silica-based integrated optical time-shift network for phased arrays. In: Proceedings of SPIE, 1994. 2155: 114–123

191 Ng W, Yap D, Narayanan A, et al. High-precision detector-switched monolithic GaAs time-delay network for the optical control of phased arrays. IEEE Photon Technol Lett, 1994, 6: 231–234

192 Stulemeijer J, van Vliet F E, Benoist K W, et al. Compact photonic integrated phase and amplitude controller for phased-array antennas. IEEE Photon Technol Lett, 1999, 11: 122–124

193 Flamand G, de Mesel K, Moerman I, et al. InP-based PIC for an optical phased-array antenna at 1.06 μm. IEEE Photon Technol Lett, 2000, 12: 876–878

194 Moreira R L, Garcia J, Li W, et al. Integrated ultra-low-loss 4-bit tunable delay for broadband phased array antenna applications. IEEE Photon Technol Lett, 2013, 25: 1165–1168

195 Sancho J, Bourderionnet J, Lloret J, et al. Integrable microwave filter based on a photonic crystal delay line. Nat Commun, 2012, 3: 1075

196 Zhang W, Yao J. A fully reconfigurable waveguide Bragg grating for programmable photonic signal processing. Nat Commun, 2018, 9: 1396

197 Zhuang L, Roeloffzen C G H, Heideman R G, et al. Single-chip ring resonator-based 1 × 8 optical beam forming network in CMOS-compatible waveguide technology. IEEE Photon Technol Lett, 2007, 19: 1130–1132

198 Zhuang L, Hoekman M, Beeker W, et al. Novel low-loss waveguide delay lines using Vernier ring resonators for on-chip multi-λ microwave photonic signal processors. Laser Photon Rev, 2013, 7: 994–1002

199 Cardenas J, Foster M A, Sherwood-Droz N, et al. Wide-bandwidth continuously tunable optical delay line using silicon microring resonators. Opt Express, 2010, 18: 26525–26534

200 Morton P A, Cardenas J, Khurgin J B, et al. Fast thermal switching of wideband optical delay line with no long-term transient. IEEE Photon Technol Lett, 2012, 24: 512–514

201 Xiang C, Davenport M L, Khurgin J B, et al. Low-loss continuously tunable optical true time delay based on Si_3N_4 ring resonators. IEEE J Sel Top Quantum Electron, 2018, 24: 1–9

202 Wang J, Ashrafi R, Adams R, et al. Subwavelength grating enabled on-chip ultra-compact optical true time delay line. Sci Rep, 2016, 6: 30235

203 Pu M, Liu L, Xue W, et al. Widely tunable microwave phase shifter based on silicon-on-insulator dual-microring resonator. Opt Express, 2010, 18: 6172–6182

204 Lloret J, Sancho J, Pu M, et al. Tunable complex-valued multi-tap microwave photonic filter based on single silicon-on-insulator microring resonator. Opt Express, 2011, 19: 12402–12407

205 Lloret J, Morthier G, Ramos F, et al. Broadband microwave photonic fully tunable filter using a single heterogeneously integrated III-V/SOI-microdisk-based phase shifter. Opt Express, 2012, 20: 10796–10806

206 Adams D B, Madsen C K. A novel broadband photonic RF phase shifter. J Lightwave Technol, 2008, 26: 2712–2717

207 Morton P A, Khurgin J B. Microwave photonic delay line with separate tuning of the optical carrier. IEEE Photon Technol Lett, 2009, 21: 1686–1688

208 Burla M, Marpaung D, Zhuang L, et al. On-chip CMOS compatible reconfigurable optical delay line with separate carrier tuning for microwave photonic signal processing. Opt Express, 2011, 19: 21475–21484

209 Howley B, Wang X, Chen M, et al. Reconfigurable delay time polymer planar lightwave circuit for an X-band phased-array antenna demonstration. J Lightwave Technol, 2007, 25: 883–890

210 Meijerink A, Roeloffzen C G H, Meijerink R, et al. Novel ring resonator-based integrated photonic beamformer for broadband phased array receive antennas-part I: design and performance analysis. J Lightwave Technol, 2010, 28: 3–18

211 Zhuang L M, Roeloffzen C G H, Meijerink A, et al. Novel ring resonator-based integrated photonic beamformer for broadband phased array receive antennas-part II: experimental prototype. J Lightwave Technol, 2010, 28: 19–31

212 Marpaung D, Zhuang L, Burla M, et al. Towards a broadband and squint-free Ku-band phased array antenna system for airborne satellite communications. In: Proceedings of the 5th European Conference Antennas Propagation, Rome, 2011. 2623–2627

213 Marpaung D, Zhuang L, Burla M, et al. Photonic integration and components development for a Ku-band phased array antenna system. In: Proceedings of International Topical Meeting on Microwave Photonics jointly held with the 2011 Asia-Pacific Microwave Photonics Conference, 2011. 458–461

214 Burla M, Roeloffzen C G H, Zhuang L, et al. System integration and radiation pattern measurements of a phased array antenna employing an integrated photonic beamformer for radio astronomy applications. Appl Opt, 2012, 51: 789–802

215 Zhuang L, Marpaung D, Burla M, et al. Low-loss, high-index-contrast Si_3N_4/SiO_2 optical waveguides for optical delay lines in microwave photonics signal processing. Opt Express, 2011, 19: 23162–23170

216 Burla M, Marpaung D, Zhuang L, et al. Integrated photonic K_u-band beamformer chip with continuous amplitude and delay control. IEEE Photon Technol Lett, 2013, 25: 1145–1148

217 Burla M, Marpaung D A I, Zhuang L, et al. Multiwavelength-integrated optical beamformer based on wavelength division multiplexing for 2-D phased array antennas. J Lightwave Technol, 2014, 32: 3509–3520

218 Horikawa K, Ogawa I, Kitoh T, et al. Silica-based integrated planar lightwave true-time-delay network for microwave antenna applications. In: Proceedings of Optical Fiber Communications, 1996. 100–101

219 Grosskopf G, Eggemann R, Ehlers H, et al. Maximum directivity beam-former at 60 GHz with optical feeder. IEEE Trans Antennas Propagat, 2003, 51: 3040–3046

220 Liu W, Li M, Guzzon R S, et al. A fully reconfigurable photonic integrated signal processor. Nat Photon, 2016, 10: 190–195

221 Capmany J, Mora J, Muñoz P, et al. A microwave photonics transistor. In: Proceedings of IEEE Topical Meeting on Microwave Photonics 2013, Alexandria, 2013

222 Pérez D, Gasulla I, Capmany J. Software-defined reconfigurable microwave photonics processor. Opt Express, 2015, 23: 14640–14654

223 Perez D, Gasulla I, Capmany J. Honeycomb lattice meshes for reconfigurable universal microwave photonics processors. In: Proceedings of SPIE/COS Photonics Asia, 2016

224 Capmany J, Gasulla I, Pérez D. Microwave photonics: the programmable processor. Nat Photon, 2016, 10: 6–8

225 Zhuang L, Roeloffzen C G H, Hoekman M, et al. Programmable photonic signal processor chip for radiofrequency applications. Optica, 2015, 2: 854–859

226 Pérez D, Gasulla I, Capmany J, et al. Reconfigurable lattice mesh designs for programmable photonic processors. Opt Express, 2016, 24: 12093

227 Pérez D, Gasulla I, Crudgington L, et al. Multipurpose silicon photonics signal processor core. Nat Commun, 2017, 8: 636

228 Perez D, Gasulla I, Capmany J. Toward programmable microwave photonics processors. J Lightwave Technol, 2018, 36: 519–532

229 Wang X, Zhou L, Li R, et al. Continuously tunable ultra-thin silicon waveguide optical delay line. Optica, 2017, 4: 507–515

230 Burla M, Khan M R H, Marpaung D A I, et al. Separate carrier tuning scheme for integrated optical delay lines in photonic beamformers. In: Proceedings of International Topical Meeting on Microwave Photonics, Singapore, 2011

231 Pérez D, Gasulla I, Capmany J, et al. Figures of merit for self-beating filtered microwave photonic systems. Opt Express, 2016, 24: 10087–10102

232 Jinguji K, Kawachi M. Synthesis of coherent two-port lattice-form optical delay-line circuit. J Lightwave Technol, 1995, 13: 73–82

233 Shao H, Yu H, Jiang X, et al. Large bandwidth and high accuracy photonic-assisted instantaneous microwave frequency estimation system based on an integrated silicon micro-resonator. In: Proceedings of 2014 IEEE 11th International Conference on de Group IV Photonics (GFP), Paris, 2014

234 Ho K, Liaw S, Lin C. Efficient photonic mixer with frequency doubling. IEEE Photon Technol Lett, 1997, 9: 511–513

235 Ghelfi P, Laghezza F, Scotti F, et al. A fully photonics-based coherent radar system. Nature, 2014, 507: 341–345

236 Pan S, Zhang Y. Microwave photonic radars. J Lightwave Technol, 2020, 38: 5450–5484

237 Trajkovic M, Blache F, Debregeas H, et al. 55 GHz EAM bandwidth and beyond in InP active passive photonic integration platform. In: Proceedings of Conference on Lasers and Electro-Optics, 2018

238 Burla M, Hoessbacher C, Heni W, et al. 500 GHz plasmonic Mach-Zehnder modulator enabling sub-THz microwave photonics. APL Photonics, 2019, 4: 056106

239 Tzu T C, Sun K, Costanzo R, et al. Foundry-enabled high-power photodetectors for microwave photonics. IEEE J Sel Top Quantum Electron, 2019, 25: 3800111

240 Lischke S, Peczek A, Morgan J S, et al. Ultra-fast germanium photodiode with 3-dB bandwidth of 265 GHz. Nat Photon, 2021, 15: 925–931